Understanding Acute Responses in *Ex-vivo* Brain Tissue Using Microfluidic Technology

A Dissertation Presented for the

Doctor of Philosophy

Degree

The University of Tennessee, Knoxville

Victoria Nickole Norman

August 2025

ACKNOWLEDGEMENTS

First and foremost, I want to acknowledge my mentor and supervisor, Dr. Rebecca A. Prosser. When I began in her lab, I knew very little about neurobiology, let alone circadian rhythms. Nevertheless, she was willing to take me on as a graduate student, and through her patience, guidance, and wisdom I have grown into the neuroscientist I am today. I also must acknowledge her willingness to see this journey through until the end with me and I am proud to be the last graduate student and end to the Prosser lab era.

Next, I would like to acknowledge my committee members: Dr. Jim Hall, Dr. Francisco Barrera, Dr. Jae Park, and Dr. Chris Baker. Their collective varied expertise and feedback have been influential to my research.

I would like to take this opportunity to extend my gratitude to my amazing friends and colleagues in the department for their support. I cannot express enough gratitude to Dr. Debalina Acharyya, who is not only a former lab mate and mentor but also a cheerleader and lifelong friend. Also, special thanks to Lauren Walden, Tere Rodriguez Garcia, Abigail Burke, and Claudia Ramos De Jesus for making surviving graduate school a little bit easier.

I would like to acknowledge the faculty of the Department of Biochemistry & Cellular and Molecular Biology for all the support and encouragement they have provided through the years. I would also like to thank all the faculty and student members of NeuroNET for their support and for providing me with resources to further my neuroscience training and research at The University of Tennessee.

I want to acknowledge the undergraduate students who have worked with me through the years: Christiane Alvarez, Jimin Lee, Emma Kate Martin, Jackson Major, Alissa Nam, Ellie Pritchard, Brenna Reed, and Harrison Wade.

I would like to thank my family, especially my parents, James and Kathy Norman, for their continued support not just through graduate school but throughout my life. The continued support, whether it be a phone call, weekend visit, or words of encouragement delivered via text, has motivated me through any self-doubt and obstacles.

Last but certainly not least, I want to thank myself. Through all the late nights, early mornings, and hard work, I want to thank myself for staying motivated to complete this goal.

ABSTRACT

Alzheimer's disease (AD) is a progressive and irreversible neurodegenerative disease that is pathologically defined by the accumulation of amyloid plaques and neurofibrillary tangles. A few of the common symptoms of AD include memory loss, confusion of time and places, changes in mood or behavior, among other things. These symptoms are due to a breakdown of synaptic connections between damaged neurons beginning in brain regions like the entorhinal cortex (EC).

The suprachiasmatic nucleus (SCN) is also thought to be affected by AD pathology as disrupted sleep is another common symptom of AD. In this work, we investigated the response of these two brain regions after being exposed to AD associated peptides, amyloid-beta (Aβ) and tau. We have demonstrated that within the first 12 hours of exogenous peptide exposure, both the EC and SCN exhibits cell death and Aβ, specifically, increases lactate dehydrogenase (LDH) release. To further expand on this research and answer more specific questions about changes in tissue due to peptide exposure we developed a novel microfluidic device. We demonstrated that Aβ and tau can induce an increase in intracellular calcium similar to potassium chloride depolarization. Additionally, we have shown that Aβ:tau stimulation leads to cell death, specifically microglial cells, within the EC. Upon targeting the ryanodine receptor with dantrolene to block the release of calcium from intracellular calcium stores, increases in fluorescence intensity due to intracellular calcium changes are still observed. However, we observed more healthy cells in the EC and SCN tissue stimulated with Aβ and tau in the presence of dantrolene as well as a reduction in LDH released. For the first time, dynamic response to exogenous Aβ and tau exposure via real-time changes in intracellular calcium concentrations has been shown. The

results presented here elucidate changes in the brain that occur with the onset of AD before cognitive symptoms may occur.

TABLE OF CONTENTS

Chapter 1: Background 1

Introduction 2

Alzheimer's Disease 2

The Suprachiasmatic Nucleus and Circadian rhythms 4

Alzheimer's, Aging, and Circadian rhythms 5

Ex-vivo Brain Tissue Slices as a Model for Disease 6

Conventional Brain Slice Chambers 10

Microfluidic Devices: What are they and why should we care? 11

Methods 12

Development of Microfluidic Devices for Acute Brain Tissue Slices 12

Chapter 2: Potential Protective Function of $A\beta_{42}$ Monomer on Tauopathies 17

Abstract 19

Introduction 20

Materials and methods – Brain Slice Toxicity 22

Brain Slice Preparation and Treatment 22

Propidium Iodide Imaging and Data Analysis 23

Lactate Dehydrogenase Assay and Data Analysis 24

Results and Discussion – Brain Slice Toxicity 25

PI staining shows minimal cell damage induced by Aβ42 alone, tauPHF43 alone or mixture of Aβ42 and tauPHF43 in the SCN 25

PI staining shows cell damage induced by mixture of Aβ42 and tauPHF43 in the EC 25

LDH assay indicates increased cell damage in response to Aβ42 treatment 25

Conclusion 31

Chapter 3: Bubble perfusion brain slice culture with single-droplet stimulus delivery in a 3D printed microfluidic device 34

Abstract 36

Introduction 37

Materials and Methods 39

Design and operation of the perfusion system 39

Temperature Characterization 40

Hydrogel glue preparation 40

Tissue slice preparation 41

Drug-stimulated Ca^{2+} response measurements 42

Comparison of EC and SCN tissue 43

Results and Discussion 44

Device design 44

Temperature characterization 47

Evaluation of tissue viability 51

Comparison of EC and SCN tissue health 53

Drug stimulus studies 56

Conclusion 59

Chapter 4: Acute response of *ex-vivo* brain tissue after initial Aβ and Tau exposure 61

Abstract 62

Introduction 63

Materials and methods 65

Thioflavin T Assay 65

Brain Slice Preparation 66

Propidium Iodide Treatment and Imaging 67
Immunohistochemical Staining and Imaging 68
LDH Sample Collection and Analysis 69
Statistical Analysis 70
Results and Discussion 71
ThT assay of Aβ, tau, and Aβ:tau aggregation 71
Stimulus-induced changes in intracellular Ca^{2+} 73
PI imaging analysis 75
PI imaging analysis of neurons and microglia 76
LDH analysis 82
Ca^{2+} imaging in the presence of dantrolene 82
PI imaging analysis in the presence of dantrolene 87
PI imaging analysis of neurons and microglia in the presence of dantrolene 90
LDH Analysis 93
Summary and Conclusions 97
Chapter 5: Summary and Conclusions 98
List of References 104
Appendices 127
A. Additional Materials for Chapter 4 128
B. Imaging Protocols 132
Image Analysis for Determining Cell Damage and Death 132
Image Analysis for Colocalization of PI in Specific Cell Types 134
Image Analysis for Calcium Imaging Time Lapsed Videos 137
Vita 140

LIST OF FIGURES

Figure 1.1 The amyloidogenic pathway 3

Figure 1.2 Biological models 7

Figure 1.3 Examples of microfluidic devices 16

Figure 2.1 The tau peptide 23

Figure 2.2 Comparison of cell death in the SCN and AH 26

Figure 2.3 Comparison of cell death in the EC 27

Figure 2.4 Quantified LDH release from the SCN 28

Figure 2.5 Quantified LDH release from the EC 30

Figure 2.6 Summary schematic 33

Figure 3.1 Perfusion Device Design 45

Figure 3.2 Temperature control characterization. 48

Figure 3.3 Temperature stability characterization 50

Figure 3.4 KCl-induced Ca^{2+} response in SCN tissue slices 52

Figure 3.5 Comparison of Ca^{2+} response in EC and SCN tissue 54

Figure 3.6 Endpoint health of EC and SCN tissue 55

Figure 3.7 Comparison of Ca^{2+} response induced by AEA and CBD 58

Figure 4.1 Peptide aggregation 72

Figure 4.2 Comparison of peptide-induced Ca^{2+} response in EC and SCN. 74

Figure 4.3 Comparison of cell death in EC and SCN 77

Figure 4.4 Comparison of heathy cells in EC and SCN 78

Figure 4.5 Comparison of neuron specific cell death in EC and SCN 80

Figure 4.6 Comparison of microglia specific cell death in EC and SCN 81

Figure 4.7 Quantified LDH release from the EC and SCN 83

Figure 4.8 Comparison of KCl induced Ca^{2+} response in EC and SCN in the presence of DMSO 85

Figure 4.9 Comparison of peptide induced Ca^{2+} response in EC and SCN in the presence of dantrolene..... 86

Figure 4.10 Comparison of cell death in EC and SCN in the presence of dantrolene..... 88

Figure 4.11 Comparison of heathy cells in EC and SCN..... 89

Figure 4.12 Comparison of neuron specific cell death in EC and SCN with dantrolene 91

Figure 4.13 Comparison of microglia specific cell death in EC and SCN with dantrolene 92

Figure 4.14 Comparison of healthy neurons in EC and SCN..... 94

Figure 4.15 Comparison of healthy microglia in EC and SCN 95

Figure 4.16 Quantified LDH release from the EC and SCN with dantrolene 96

Figure A.1 Comparison of Ca^{2+} response in EC slices 128

Figure A.2 Comparison of Ca^{2+} response in SCN slices 129

Figure A.3 Comparison of number of microglia and neurons in EC and SCN 130

Figure A.4 Comparison of number of microglia and neurons in EC and SCN with dantrolene 131

LIST OF ABBREVIATIONS

3R	3-repeat
4R	4-repeat
Aβ	Amyloid beta
AD	Alzheimer's Disease
AEA	Anandamide
AH	Anterior hypothalamus
APP	Amyloid Precursor Protein
aCSF	Artificial Cerebrospinal Fluid
BMAL1	Brain and muscle ARNT-like 1
Ca2+	Calcium ion
CB1	Cannabinoid receptor 1
CBD	Cannabidiol
ChitHCl	Chitosan hydrochloride
CICR	Calcium-induced calcium release
CLOCK	Circadian locomotor output cycles kaput
CRY	Cryptochrome
CycA	Cyclosporine A
DAPI	4',6-diamidino-2-phenylindole
DDA	Dextran dialdehyde
EBSS	Earl's Balanced Salt Solution
EC	Entorhinal Cortex

ER	Endoplasmic reticulum
HBSS	Hank's Balanced Salt Solution
hIAPP	Human islet polypeptide
IMS-MS	Ion mobility spectrometry mass spectrometry
KCl	Potassium chloride
LDH	Lactate Dehydrogenase
MAPT	Microtubule-associated protein tau
NFTs	Neurofibrillary tangles
OCT	Optimal cutting temperature
PBS	Phosphate-buffered saline
PDMS	Polydimethylsiloxane
PER	Period
PHF	Paired helical filaments
PI	Propidium Iodide
ROI	Region of interest
RyR	Ryanodine receptor
SCN	Suprachiasmatic Nucleus
T2D	Type 2 diabetes
ThT	Thioflavin T

Chapter 1: Background

Introduction

Alzheimer's Disease

Alzheimer's disease (AD) is a progressive and irreversible neurodegenerative disease that is the most common cause of dementia.[1] First discovered in the early 1900's by Dr. Alois Alzheimer, AD is characterized pathologically by the accumulation of amyloid plaques and neurofibrillary tangles (NFTs) he observed in the postmortem brain of a patient exhibiting memory loss, language problems, and unpredictable behavior.[2,3] Through further research, scientists in the field continued to understand more about changes in the brain due the AD. In addition to the accumulation of amyloid-beta (Aβ) and tau peptides into to insoluble plaques and NFTs, AD is further characterized by the loss function and connection between neurons.

Currently, the amyloid hypothesis or the amyloid cascade hypothesis is one of the accepted explanations for the pathogenesis of AD. In this hypothesis, Aβ is released into the extracellular space where under normal conditions it is rapidly degraded but under pathological conditions the peptides begin to accumulate into amyloid fibrils that eventually develop into insoluble Aβ plaques.[4] Aβ is a 40 or 42 amino acid peptide produced when the amyloid precursor protein (APP) is cleaved by β- and γ-secretase, sequentially (**Figure 1.1**). While Aβ is found in the extracellular space in non-pathological conditions, the normal function of the peptide is not fully understood. Some studies suggest it may play a role in things like kinase activation[5], protection against oxidative stress[6,7] and regulating cholesterol transport.[8,9] It has also been shown to be not essential, as loss of Aβ in mice does not lead to loss of physiological function.[10–12]

Similarly, the tau hypothesis is that tau isoforms found within the axons of neurons are the principle causative substance of AD.[4] Tubulin associated unit, more commonly known as tau,

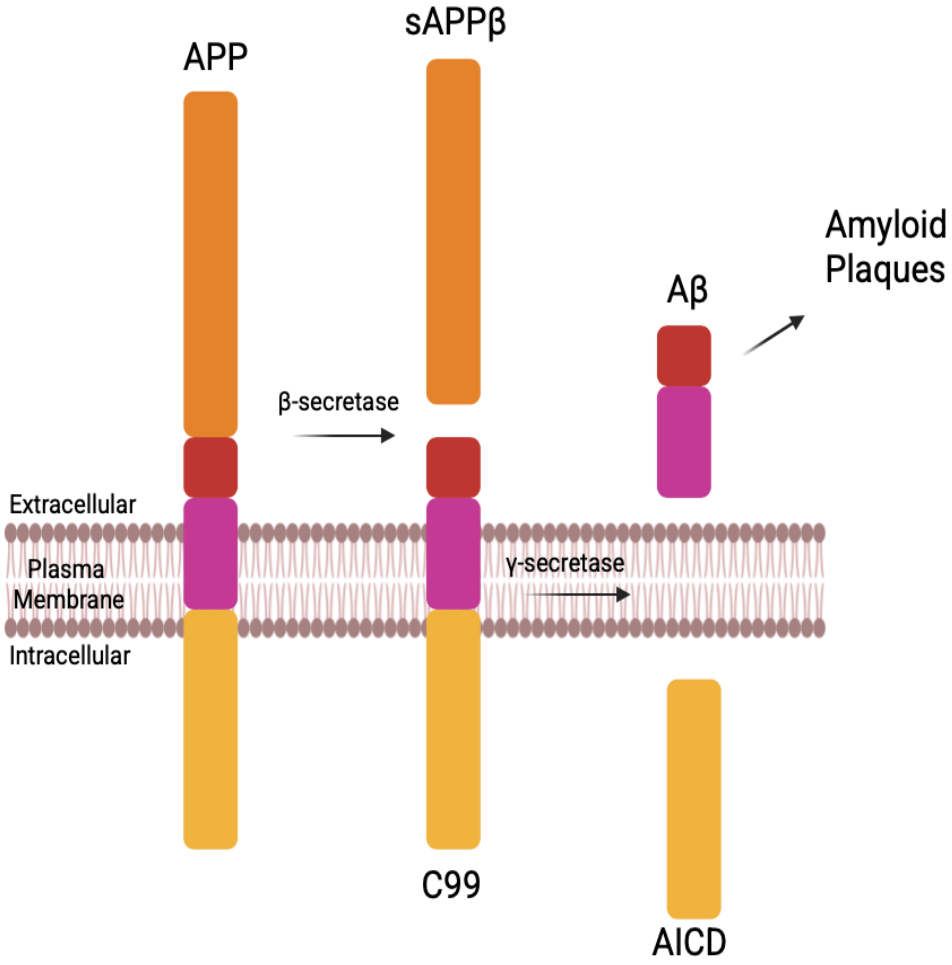


Figure 1.1 The amyloidogenic pathway illustration of how Aβ is produced through the proteolytic cleavage of the amyloid precursor protein (APP)

refers to a group of six protein isoforms produced by the alternative splicing of the microtubule-associated protein tau (MAPT) gene. Through this alternative splicing, the inclusion of exon 10 in the microtubule binding domain yields 4-repeat (4R) isoforms or 3-repeat (3R) isoforms that do not include exon 10. These protein isoforms are abundant in neurons and their main function is to help stabilize microtubules in the distal axons. In normal physiological conditions tau undergoes phosphorylation but it is specifically in pathological conditions where tau affinity for tubulin decreases and the protein can accumulate into insoluble NFTs that disturb microtubule networks, compromising the function of neurons.[13–15]

The entorhinal cortex (EC) is essential for memory formation and consolidation by processing and transmitting information to the hippocampus.[16–18] Issues with memory are often the first indicator of cognitive impairment due to AD. This is attributed to the initial accumulation of tau and Aβ peptides in the EC and hippocampus before spreading to other areas in the brain.[19–21] The mechanisms by which these peptides spread are not fully understood but both have been shown to travel from infected to neighboring healthy areas.[15] Given that the EC is one of the first areas in the brain to experience neurodegeneration due to AD, most research pertaining to AD focus on the EC and related areas.[22]

The Suprachiasmatic Nucleus and Circadian rhythms

The suprachiasmatic nucleus (SCN) is a small, bilateral structure in the hypothalamus region of the brain that is located just above the optic chiasm and straddles the third ventricle. It is made of neurons and glial cells and is a cell dense area with approximately 10,000 neurons in each unilateral SCN that can be categorized into two subdivisions: a ventral “core” region and a dorsal “shell” region. The core borders the optic chiasm, receiving retinal input and projecting

densely to the shell while the shell partially envelops the core, receiving its input and projecting sparsely back to it.

The SCN is known as the internal clock as it is responsible for generating circadian rhythms. In mammals, this is done through a delayed feedback loop that regulates the transcription, translation, and activity of clock genes and proteins. The process starts with the dimerization of circadian locomotor output cycles kaput (CLOCK) and brain and muscle ARNT-like 1 (BMAL1) which promote the transcription of genes in the *Period* (*Per1, Per2*, and *Per3*) and *Cryptochrome* (*Cry1* and *Cry2*) gene families increasing PER and CRY levels. PER/CRY dimers inhibit CLOCK/BMAL1-mediated transcription thereby inhibiting the transcription of their own genes, creating a transcriptional translational feedback loop.

Alzheimer's, Aging, and Circadian rhythms

While the two recognized hallmarks of AD are the Aβ plaques and NFTs, another commonly observed cognitive symptom is disrupted circadian rhythms. Patients have been observed to exhibit symptoms such as trouble falling asleep or poor sleep quality, sometimes a whole decade before other cognitive symptoms associated with AD occur.[23–26] Due to the SCN's important biological role in sleep, it has been the focus of studies on disrupted circadian rhythm in AD patients and neurodegeneration within the region itself. It has been suggested that neuronal dysfunction in the SCN could be a consequence or lend to the development of AD.[27–29]

Studies done in animal models report significant neurodegeneration and inflammatory responses in the SCN of AD mice, along with circadian disruptions and sleep abnormalities. Further studies have used non-invasive tools, such as MRI, to help identify microstructural changes in the SCN during AD development.[30,31] While there is evidence that the SCN undergoes

changes during AD development and researchers looking for answers as to what exactly those changes are, how the SCN is affected before or during AD is still largely unknown.

Ex-vivo Brain Tissue Slices as a Model for Disease

The brain is a complex organ that exhibits heterogeneity at all levels, including development, structure, vasculature and cells. It is protected by the skull, multiple layers of meninges, and the blood-brain barrier. These and other factors make it very difficult to study its physiological and pathological processes. And while animal models are pivotal in understanding physiological and pathological processes, they often do this with the assumption that data derived from animal models are directly translatable to human physiology. Unfortunately, this is not always the case, which can result in failures in clinical trials.[32] Although advances in experimental techniques have increased our abilities to investigate the brain *in situ*, much research on the brain still requires approaches utilizing cells and tissues removed from the intact animal.

In vitro (long-term) approaches to studying brain functions include cell cultures, organotypic brain slices, and more recently, organoids (**Figure 1.2**). Their accessibility and longevity allow multiple forms of investigation, including electrophysiology, cell imaging, chemical stimulation, genetic manipulations, and analysis of released substances. To begin with, cell cultures enable the investigation of specific cellular processes at the single- and multi-cellular level, providing key insights into intra- and intercellular communication.[32] They allow precise control over what cell types are present, and allow the activity of single cells to be followed over long periods of time. However, they lack the normal cellular architecture, which limits how directly their cellular/extracellular interactions are translatable to the intact brain.

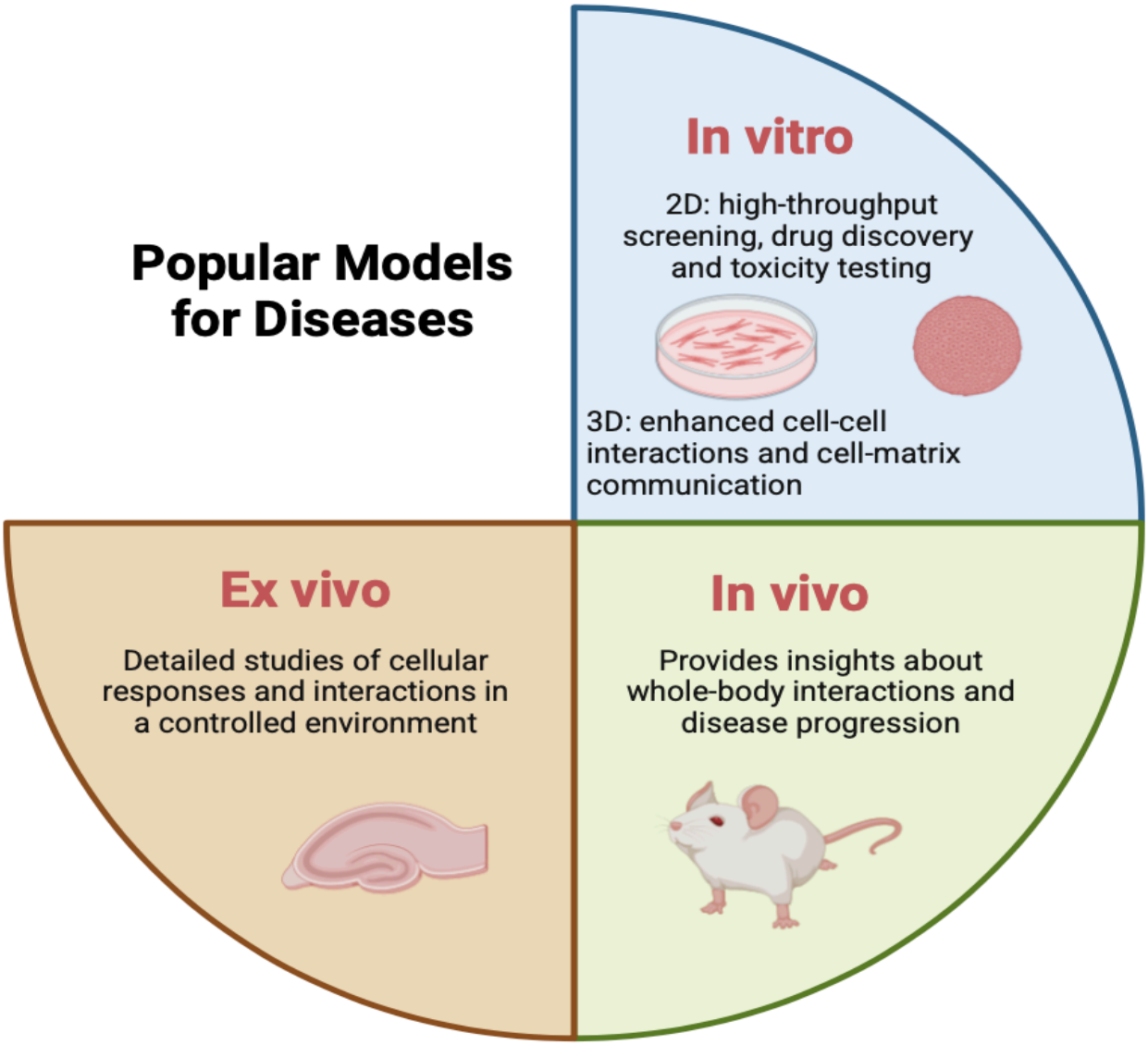


Figure 1.2 Biological models A comparison of *in vitro, in vivo,* and *ex vivo* models for studying disease

Organoids offer more complexity with multiple cell types that grow in a 3-dimensional arrangement.[33] They are derived from stem cells that self-organize into complex structures that can recapitulate fundamental functional properties of organs or tissues. They allow researchers to move away from the limitations of animal models while still providing more complexity than cell cultures, but organoids also have drawbacks. Though they present impressive three-dimensional architecture that can mimic the brain, they are deficient in the vasculature needed to provide nutrients and oxygen to be sustained long-term, and it is unclear how precisely they recapitulate normal brain structure.[33]

Lastly, organotypic brain slices offer a model taken straight from the animal that therefore (initially) contains the original architecture and vasculature.[34,35] The typical ways of culturing these slices are the interface method or the roller tube method.[35] In the former, the slice sits on a porous membrane where it receives culture medium from below and oxygen from above and in the latter, the slice is mounted on a cover slip that is slowly rotated within a test tube partially filled with culture medium, allowing the slice to spend half its time in medium and half its time in oxygen.[35] Both methods can sustain slices for several weeks. However, organotypic brain slices do not exhibit vascular perfusion, and they undergo substantial reorganization, cell loss, and cell growth when cultured long-term, and thus do not maintain their *in vivo* cellular connections.[34] Thus, each of these *in vitro* preparations has their advantages and disadvantages.

Ex vivo (acute) brain slices are a preparation dating back to the late 1950's with Henry McIlwain recording resting membrane potentials from cortical slices[36]. They are typically maintained for 24h or less using minimal salt solutions rather than culture media. They serve as a middle ground between *in vivo* and *in vitro* models, providing physiological complexity through maintained architecture, morphology, and cell heterogeneity. Similar to *in vitro* models, they can

provide easy access for electrophysiology, imaging, and analyte analyses while applying physiological, pharmacological, and toxic manipulations, depending on how they are maintained[36–38]. *Ex vivo* brain slices have proven to be an extremely useful preparation, providing significant insights into brain function under both physiological and pathological conditions.[38]

The use of *ex vivo* tissue slices as a model can be advantageous but they also have their limitations. For example, similar to *in vitro* brain slices, afferent input to the brain region as well as changes in neuronal activity driven by adjustments in vascular circulation have been eliminated. Also, depending on the brain region being investigated, slice preparation can result in substantial damage to projection neurons, which can compromise the overall health of the tissue.[34,39]

Another important consideration is that removing the tissue from the body deprives the slices of vascular perfusion, so that the tissue must rely solely on diffusion for oxygenation and nutrient exchange. Thus, the viability of *ex vivo* tissue is dependent on the efficiency of nutrient and waste exchange as well as oxygen supply. This results in inner layers of the tissue often not receiving enough oxygen and nutrients, which compromises viability.[39] It has been shown that maintaining tissue samples with continuous perfusion can combat this by improving circulation in and around the tissue.[40] However, devising systems that provide the proper nutrients and oxygen saturation to maintain viability for extended periods of time while avoiding mechanical stressors can be challenging. This constrains variables such as slice thickness, rate of perfusion, and access to sufficient oxygen. Together these factors ultimately determine how long the tissue remains healthy and the repeatability of observed phenomena. In the following sections we go into more detail about typical preparations for acute tissue slices that have been used in the past

and how the integration of microfluidic technology has improved those preparation techniques and lead to enhanced experimental designs.

Conventional Brain Slice Chambers

Since the first acute tissue slice preparations, neuroscientists have developed standardized chambers used to maintain *ex vivo* brain slices.[38,41] These chambers involve flowing hyper-oxygenated artificial cerebrospinal fluid (aCSF) or nutrient containing media over or around the brain slices, and they can be separated into two categories: interface or submerged slice chambers.[41,42] An interface chamber, sometimes referred to as a 'Haas' type chamber, involves the brain slice resting on a piece of filter paper or nylon mesh as oxygenated aCSF is perfused under it and the top is exposed to carbogen (95% O_2:5% CO_2)[41]. The filter paper or nylon mesh allows for nutrient and waste to be exchanged with the aCSF underneath, while the exposed top surface of the slice allows for oxygen exchange. While this provides efficient atmospheric gas exchange, the upper surface of the brain slices can be prone to drying out if the atmosphere in the chamber is not sufficiently humid. In submerged chambers, tissue is completely submerged in hyper-oxygenated aCSF, allowing for nutrient and oxygen diffusion from all sides.[42] However, oxygen exchange into the brain slice is less efficient in this type of chamber.[43]

Depending on their specific designs, these brain slice chambers are best suited for modulating brain slice physiology using chemical or electrical stimuli and assessing changes using electrophysiology. However, their large perfusion volumes and overall size make imaging and analysis of released substances more difficult. While the use of these chambers has provided substantial insights into brain function, a recent trend towards maintaining brain slices in microfluidic devices is bringing key advantages.

Microfluidic Devices: What are they and why should we care?

The term 'microfluidics' refers to a system that manipulates small volumes of fluids using small channels that are on the size order of tens to hundreds of microns.[44] While 'microfluidic device' is a broad term to describe fabricated technologies addressing specific scientific problems or questions, there are features that they all share, such as small perfusion volumes (L to fL), small channels for solution delivery, and the ability to be integrated into various experimental configurations such as electrophysiology and microscopy.[44] As the development of microfluidics has progressed, culturing cells and tissues using this approach has become commonplace. Specifically, in regard to biopsied tissues, these efforts have been coined 'organ-on-a-chip' and involve using microfluidics to aid in drug discovery and development, study disease physiology, and understand complex processes in basal and disease states.

More recently, the development of microfluidic devices for maintaining *ex vivo* brain tissue slices has begun to address some of the previously mentioned experimental limitations. They can support brain slice viability using principles derived from conventional brain slice chambers but just on a smaller scale. Importantly, due to the decreased size of microfluidic devices, they offer versatility and flexibility that allows them to be integrated into a wide range of experimental configurations.[45] Hurdles to their broad use with brain tissue have included providing sufficient oxygenation and aCSF exchange in the smaller format, as well as maintaining access to the tissue for experimental manipulations and assessments. The development of microfluidic devices to maintain *ex vivo* tissue while allowing different types of experimental data acquisition is reviewed below.

Methods

Development of Microfluidic Devices for Acute Brain Tissue Slices

Passeraub et al.[46] were among the first to maintain brain slices in microfluidic devices. They developed a device that has regular and controlled flow into the chamber, similar to that used in interface chambers, but with a reduced total volume (~100 uL) and a perfusate exchange rate four times faster than conventional perfusion chambers. The nutrient and oxygen exchange tissue slices experience also mimics conventional interface chambers, but the tissues rest on an array of microposts as opposed to the filter paper or nylon mesh normally used to maximize the surface contact between the perfusate and tissue.

To demonstrate its utility, transverse hippocampal slices with a thickness of 600 microns were prepared from Sprague-Dawley rats and transferred into their microfabricated chamber. Using microelectrodes, they recorded spontaneous epileptiform activity from the stratum pyramidale of the CA3 region following the removal of Mg^{2+} from the aCSF perfusing the chamber. Their work was the first to demonstrate a new microfluidic perfusion system based on a simple microfabrication process with hopes of future integration of other valuable features such as microfluidic channels for drug delivery and electrode or sensor arrays within the chamber.

Soon after, Blake et al.[47] developed a three-layered polydimethylsiloxane (PDMS) device that holds a brain slice in place with microposts from the above and below while also allowing for flow of solution to the tissue. The device was design for medulla brain slices between 530 and 700 microns thick, obtained from neonatal rats. The unique design of this device is a closed system that uses laminar flow to direct the perfusion to specific areas of the brain slice, allowing each region to be targeted with different solutions simultaneously. Blake et al. demonstrated this

capability by focusing a stream of Na^+-free solution on one half of the slice, abolishing spontaneous neural activity only in that half while the other half remained active.

Similarly, Tang et al.[48] demonstrated localized chemical stimulation of brain slices in their microfluidic device. However, instead of using an enclosed chamber, the brain slices rest on top of an array of microposts and suction pressure is used to achieve localized injection. Using 400-micron thick coronal slices from C57Bl/6 female mice, they showed local induction of cortical spreading depression by locally injecting 1M potassium chloride (KCl). Microscopy was integrated into the microfluidic setup for the first time, and brain slices were imaged while in the microfluidic device using epifluorescence. Depolarization-induced cellular swelling caused the optical properties of cells to change. Both of these latter groups[47,48] were able to demonstrate the advantage of using microfluidic devices for area-specific drug delivery.

Microfluidic devices are not only advantageous for precisely regulated fluid delivery to brain slices, but they can also regulate the flow of gas to the tissues. The previously mentioned devices have been designed with a closed chamber that houses the tissue slice with tightly regulated flow of medium. In contrast, Mauleon et al.[49] manipulated the delivery of oxygen gas to brain slices to study the neuronal response to an hypoxic environment. In this study, a commercially available perfusion chamber was used and a microfluidic add-on with gas channels was developed. Hippocampal slices were obtained from wild type BL7 mice and placed in the device so that the dentate gyrus and CA1 regions were receiving oxygen from different gas channels. Researchers imaged the two regions while lowering the oxygen concentration to the CA1 region and observed an increase in intracellular calcium, using Fura-2/AM, during hypoxic conditions.

More recently, Saleheen et al.[50] developed a microfluidic device that improved on previous systems in two ways: providing oxygenation in an enclosed chamber and sizing the device so it fits on the stage of a standard upright microscope for imaging. The device continuously delivers alternating gas bubbles and media droplets meant to mimic the roller tube method on a smaller scale. Their closed system consists of a chamber fabricated from glass and polydimethylsiloxane (PDMS). To test its functionality, coronal brain tissue slices, 500 microns in thickness, containing the SCN and surrounding anterior hypothalamus were prepared from male C57/Bl6 mice. Tissues were stimulated periodically throughout an 8-hour period with droplets containing 30 mM KCl while increases in intracellular calcium were imaged using Fluo-4 AM to confirm continued tissue health. At the end of experimentation, slices were stained with propidium iodide (PI) and then fixed for histological assessment of tissue health. The researchers achieved a well-controlled and consistent perfusion of this chamber while demonstrating sustained tissue health for a long period of time. While this device design addressed the goals of the researchers, improvements were needed. The continuous flow and relatively wide perfusion channel made analyte sampling difficult. Precise delivery of stimulus and response monitoring was also limited due to the way the device was designed. These shortcomings were addressed in future design iterations of this device.

Following from the success of the bubble-droplet microfluidic device by Saleheen et al., we have modified the initial device to address some of the restrictions imposed by previous microfluidic designs. Specifically, we wanted to develop a microfluidic device that would maintain healthy brain slices for extended periods of time (>8-12 h), allow real-time assessments of the brain slices via microscopy, and allow for investigation of time-stamped analytes released by the tissue into the perfusion media. We also wanted the device to be easily modifiable for

parallel concurrent brain slice experiments and for addition of other modalities such as electrophysiological recordings. With these considerations in mind, we have developed a 3D-printed version that has smaller channel dimensions to reduce the overall volume and incorporates temperature regulation through a circulating water bath compartment. The small size of the device enables it to fit on a standard microscope stage for real-time microscopy. Pinch valves allow for precise control of media and air flows into and out of the chamber, so that perfusion droplets can be paused in the chamber. Additionally, multiple inlet valves allow for multiple stimuli to be delivered to the tissue sequentially. These important modifications allow analytes released by the tissue in response to multiple stimuli to be concentrated in small droplet volumes and remain segregated from other droplets after leaving the chamber so that precisely timed changes in analytes can be investigated. Most recently Ca^{2+} changes induced by cannabinoids were explored by Gutierrez et al., and as done previously, PI was used to assess tissue health. Preliminary attempts at analyte detection from media droplets were done to detect lactate dehydrogenase, an enzymatic cell death indicator, as another way to assess tissue health. This combination of features has led to a system capable of maintaining healthy tissue for at least 12 hours while integrating real-time microscopy analysis and improved analyte collection.

Microfluidics have proven to be an important improvement on traditional tissue slice preparation techniques. Multiple devices for various uses have been summarized in the above discussion (**Figure 1.3**). The advancement of 'organ-on-a-chip' technology allows for the recapitulation of *in vivo* physiology on a small scale. This is appealing for understanding complex disease processes, studying disease physiology, and drug discovery and development. With this knowledge, experiments were designed to investigate responses of *ex-vivo* tissue slices to Aβ and tau exposure with the goal of identifying initial changes before the onset of

AD. First using traditional culturing techniques before moving on to integrate microfluidic technology, our work investigated how these AD-associated peptides specifically effected the EC and SCN regions within the brain.

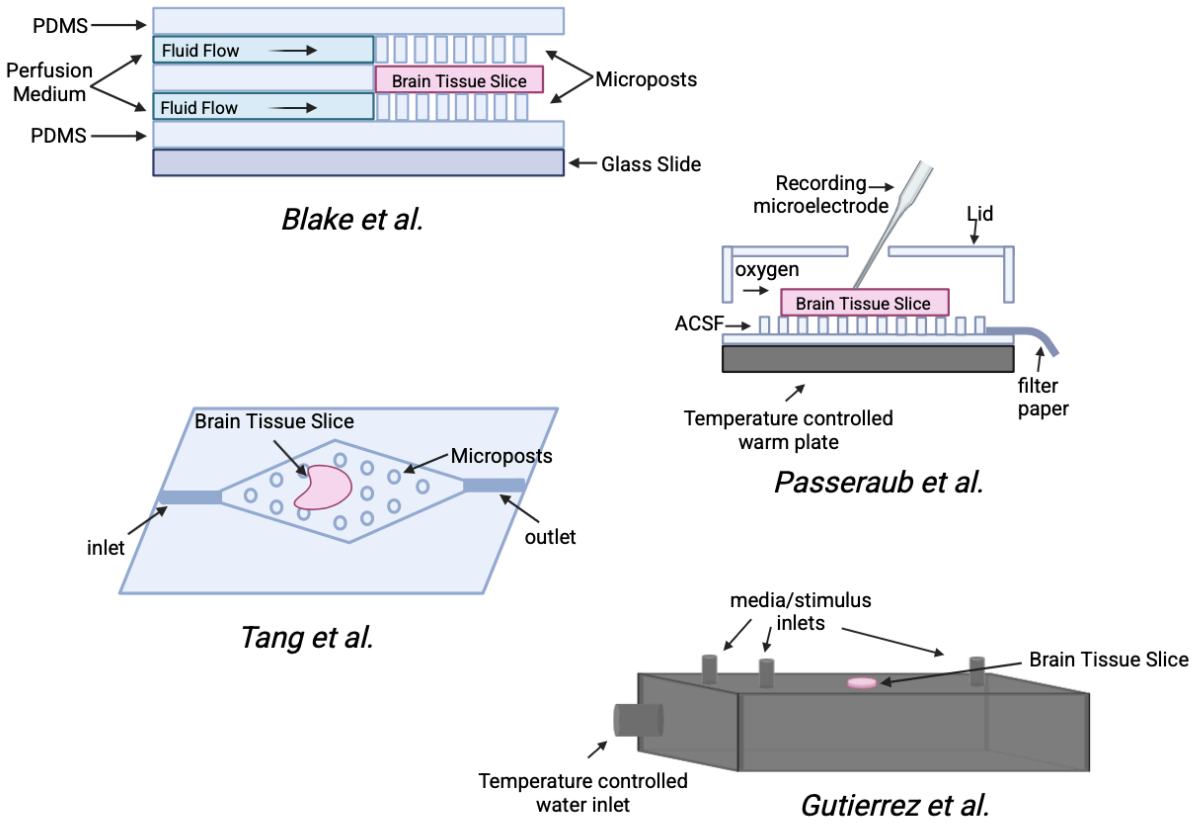


Figure 1.3 Examples of microfluidic devices Adapted schematics showing the configuration of the multiple microfluidic devices

Chapter 2: Potential Protective Function of $A\beta_{42}$ Monomer on Tauopathies

A version of this chapter was originally published by Amber L. H. Gray, Victoria Norman, Damilola S. Oluwatoba, Rebecca A. Prosser, and Thanh D. Do.

Amber L. H. Gray, Victoria Norman, Damilola S. Oluwatoba, Rebecca A. Prosser, and Thanh D. Do, “Potential Protective Function of $A\beta_{42}$ Monomer on Tauopathies” *Journal of the American Society for Mass Spectrometry.* 2023, 34(3), 472-483. (DOI: 10.1021/jasms.2c00343)

Abstract

While soluble forms of amyloid-β (Aβ) and Tau work together to drive healthy neurons into a disease state, how their interaction may control the prion-like propagation and neurotoxicity of Tau is not fully understood. The cross-linking via disulfide bond formation is crucial for Tau oligomers to obtain stable conformers and spread between cells. This work thus focuses on how $A\beta_{42}$ regulates this critical process. By studying the interactions between $A\beta_{42}$ and Tau_{PHF43}, a construct that mimics the Tau R3 isoform, has a similar length to $A\beta_{42}$ and contains one cysteine (Cys-322), we discovered that fresh $A\beta_{42}$ could protect Tau against the formation of disulfide cross-linked dimers. We showed by ion mobility spectrometry mass spectrometry (IMS-MS) that the monomeric and small Aβ oligomers (we termed them the "non-amyloidogenic Aβ") could efficiently disassemble Tau dimers and heparin-induced Tau fibrils to recover Tau monomers. Interestingly, the Tau disassembly is not driven by the competitive co-aggregation of Aβ and Tau but via Aβ serving as an antioxidant to prevent disulfide bond formation. Its effect was supported by the experiments of Aβ with cystine, the oxidized dimer of cysteine. Furthermore, using cyclosporine A (CycA), a lipophilic macrocyclic peptide and a β-sheet disruptor, we demonstrated that targeting the β-sheet structures (amyloidogenic Aβ) with CycA does not affect the Tau_{PHF43} disassembly driven by $A\beta_{42}$. We expect this protective function of $A\beta_{42}$ on Tau to be lost once Aβ aggregates into plaques. Separately, we assessed the initial toxicity of $A\beta_{42}$ and Tau_{PHF43} in acute brain slices and found that $A\beta_{42}$ is more toxic than Tau_{PHF43} or the two peptides combined. Our work highlights a potential protective role of $A\beta_{42}$ monomers in AD that was previously overlooked while focusing on the mechanism behind $A\beta_{42}$ aggregation leading to tau dysfunction.

Introduction

The self-assembly of proteins into amyloid fibrils is broadly associated with human neurodegenerative disease.[51–54] However, it is also well-accepted that some soluble oligomers, which precede fibril formation, are the toxic species of such diseases.[55–58] Examples of amyloids include the proteins $A\beta_{42}$ and Tau, which may underlie the initiation and pathophysiology of Alzheimer's disease (AD).[59–61]

It has long been debated how $A\beta_{42}$ and Tau coincide *in vivo* to cause cellular death and damage exhibited in AD. Hardy and Higgins initially proposed the amyloid cascade hypothesis in the 1990s,[62] linking $A\beta_{42}$ aggregation and amyloid plaques to a rise in intracellular Ca^{2+} level as the primary cause of cell death. The hypothesis was later modified to include the hyperphosphorylation of microtubule-associated Tau proteins (Tau), which induces the formation of neurofibrillary tangles (NFT) in neurons of AD[21,63] or other Tauopathies.[64,65] Transgenic mice studies supported the crosstalk between Aβ and Tau. Current models suggest Aβ initiates a pathophysiological cascade leading to Tau misfolding and accumulation into NFTs.[66–68]

However, one of the main issues underlying this "bullet" ($A\beta_{42}$) and "trigger" (Tau) hypothesis[69] is the disconnect between the spatial and temporal distribution of $A\beta_{42}$ and Tau. In some instances, the presence of NFTs can precede amyloid plaques by approximately a decade.[70–72] Due to the recent controversies with the amyloid oligomer hypothesis, we propose an alternative view that the aggregation of Aβ impairs specific interactions essential to protect the normal Tau functions. One such interaction could be between monomeric Aβ and Tau. Because Aβ quickly aggregates *in vitro* or cell models, the actions of Aβ monomers could easily be overlooked.

Additionally, NFTs reside inside the neurons, while amyloid plaques accumulate as extracellular deposits. Despite this difference, it has been speculated that soluble $A\beta_{42}$ may exist intracellularly,[73,74] specifically in the perikaryon of pyramidal cells.[75] Furthermore, normal Tau can be found in the extracellular space.[76–78] Therefore, soluble Aβ and Tau have ample opportunity to interact inside and outside of cells, and the smaller species, like monomers of Aβ and Tau, may interact more frequently than the larger and more stable species, like oligomers and fibrils.

To investigate this molecular cross-talk between soluble $A\beta_{42}$ and Tau, a technique that can separate and capture individual oligomeric species is required. Ion mobility spectrometry – mass spectrometry (IMS-MS) is an experimental technique that can isolate individual amyloid oligomers by obtaining reduced ion mobilities of isobaric oligomeric species of the same mass-to-charge ratio (*m/z*).

Surprisingly, few studies have investigated the interactions between soluble $A\beta_{42}$ and Tau oligomers that may arise in the early disease state. Only one study has examined the interactions between short Tau and Aβ model fragments with IMS-MS.[79] One facet of the current study aims to investigate how soluble $A\beta_{42}$ and Tau species may interact prior to the formation of tangles and fibrils. By understanding these initial interactions, we can gain insights into the mechanisms that induce full-disease pathology and the potential subtle functions of $A\beta_{42}$ that could be overshadowed by its aggregation. Furthermore, we investigated how cyclosporine A (CycA), a cyclic peptide known to interact with β-sheets,[80] interferes with the interplay between $A\beta_{42}$ and Tau. Finally, we tested the toxicity of $A\beta_{42}$ and Tau in acute brain slices to begin to assess their separate and combined pathology in an intact tissue preparation.

Full-length Tau contains two N-terminal domains and a microtubule-binding region. The microtubule-binding region consists of four repeats. Human Tau has six different isoforms, which differ by the number of two N-terminal domains and the presence of the second repeat (R2) within the microtubule-binding region (**Figure 2.1**). The propensity of Tau to form paired helical filaments (PHF) depends on two six-residue sequences (PHF6; ^{306}VQIVYK^{311} and PHF6*; ^{275}VQIINK^{281}) of which PHF6 is present within all Tau isoforms.[81,82] These amyloid nucleating regions initiate PHF formation by promoting Tau's random-coil to a β-structure.[81,82] This current study specifically utilizes a Tau construct, termed Tau_{PHF43}, which exhibits similar aggregation behavior to the full-length Tau. Specifically, dimerization and anionic factors such as heparin promote the formation of thin fibrils.[81]

Materials and methods – Brain Slice Toxicity

Brain Slice Preparation and Treatment

Adult (2-4 months old) male C57BL/6 mice were housed under 12:12 light-dark conditions with food available *ad libitum* for at least 2 weeks prior to use in the experiments. Coronal brain slices with a ~450 – 500μM thickness, containing the suprachiasmatic nucleus (SCN) and the surrounding anterior hypothalamus (AH) or the entorhinal cortex (EC) were prepared immediately after lights-on. Tissue slices were maintained at 37ºC and supplied with 95% O_2/5% CO_2 in an interface brain slice chamber constantly perfused with Earl's Balanced Salt Solution (EBSS, MP Biomedicals, LLC, Solon, OH), supplemented with dextrose anhydrous and sodium bicarbonate (pH 7.4), at a rate of approximately 20 mL/h, as described.[83]

Approximately one hour after preparation, tissue slices were transferred to small-volume, static wells maintained within the perfusion chambers. 200 mL of EBSS (control) or EBSS supplemented with $A\beta_{42}$, Tau_{PHF43}, or $A\beta_{42}$ +Tau_{PHF43} peptides were added into the static wells to

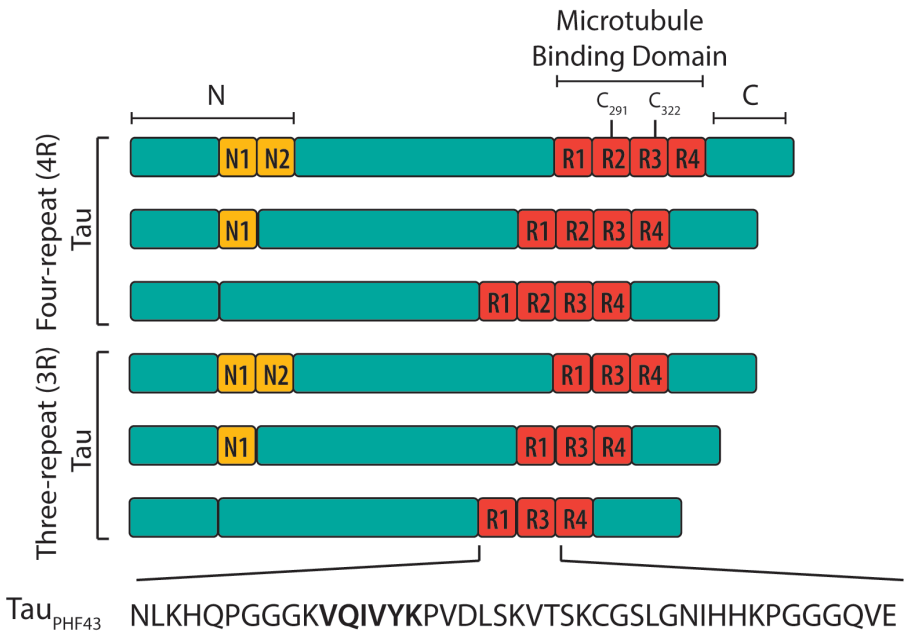


Figure 2.1 The tau peptide Schematic of the six different human Tau isoforms. Note that full length Tau contains two cysteines. The sequence of Tau_{PHF43} is given, which encompasses part of the repeat 1 domain (R1), all of R3, and part of R4

slightly submerge the tissue slices. The final concentration of the peptides in the wells was 40µM for all experiments. The media surrounding the tissue slices was collected and replaced every 2h and stored at -80ºC for lactate dehydrogenase analysis. After 12h the slices were transferred back into the main perfusion well of the brain slice chamber.

Propidium Iodide Imaging and Data Analysis

Tissue slices transferred back to the perfusion chamber were perfused for 2h with 4.6 µg/mL propidium iodide (PI) prepared in EBSS in order to assess the tissue health. PI is only membrane permeable in dead and damaged cells, where it intercalates with the DNA and is fluorescent upon excitation at ~535 nm.[84–87] After PI perfusion, the tissue slices were placed in 4% paraformaldehyde for 10 min and then incubated in 30% sucrose overnight at 4º C. The following day, the slices were embedded in optimal cutting temperature compound (Fisher HealthCare, Houston, TX) and stored at -80°C until sectioning. 10 µm thin-cut tissue slices were prepared using a cryostat, collected on gelatin-subbed slides, and stored at -80° C. For staining,

slides containing the tissue sections were first allowed to air dry and then washed three times in phosphate buffered saline for 10 min. After the wash, the sections were cover slipped using mounting media that includes the nuclear stain 4',6-diamidino-2-phenylindole (DAPI; Vectashield, Vector Laboratories, Burlingame, CA), and the coverslip edges were sealed using nail polish. Fluorescence images were acquired using a Leica DM6000B microscope and analyzed using ImageJ software (NIH). One image, chosen to be near the center of the SCN and having clear SCN and AH adjacent to each other or to be near the center of the EC, was analyzed for each tissue slice. A total of 6 images were analyzed for each experimental condition. The images were split into blue and red channels, where the blue channel shows DAPI-stained cells, and the red channel shows PI-stained cells. Within each region of interest (SCN, AH, and EC) the total number of cells in the identified area were counted using the blue channel. The PI intensity across the cells in the same region was assessed using the red channel. The ImageJ thresholding option was used to differentiate between high PI intensity cells corresponding to dead cells, moderate PI intensity indicating damaged cells, and cells with minimal PI staining, considered healthy cells.[86,87] The percentage of total (DAPI-stained) cells that were healthy, damaged, or dead cells was then calculated. Histology analyses were performed by three individuals blind to the experimental conditions and their percentages were averaged together. Differences in the percentage of healthy, damaged, and dead cells in each brain region across experimental conditions were determined using 2-way ANOVAs, with $p<0.05$ set as significant.

Lactate Dehydrogenase Assay and Data Analysis

The media surrounding the tissue slices (N=6 for each experimental condition) that was collected and stored at -80ºC was used for a lactate dehydrogenase (LDH) cytotoxicity assay. LDH is a cytosolic enzyme that is present in most cells and is released upon damage to the

plasma membrane.[88,89] Through a coupled enzymatic reaction where LDH catalyzes the production of formazan, extracellular LDH can be quantified (CyQUANT LDH Cytotoxicity Assay kit; Invitrogen, Eugene, OR). Averaged absorbances at each time point for each brain region across experimental conditions were determined using one-way ANOVAs, with $p<0.05$ set as significant.

Results and Discussion – Brain Slice Toxicity

PI staining shows minimal cell damage induced by Aβ42 alone, tauPHF43 alone or mixture of Aβ42 and tauPHF43 in the SCN

Histology images revealed sparse PI labeling of cells in the AH and virtually no PI labelled cells in the SCN across all experimental conditions (**Figure 2.2 A-D**). Two-way ANOVAs testing within each cell grade determined that there were no statistically significant differences in the percentage of healthy, damaged, or dead cells across experimental conditions or between the two brain areas (**Figure 2.2 E,F**).

PI staining shows cell damage induced by mixture of Aβ42 and tauPHF43 in the EC

Histology images revealed little to no PI labelled cells in the EC for control, Aβ, and tau experimental conditions but some PI labelled cells in the Aβ:tau condition (**Figure 2.3 A-D**). Two-way ANOVAs testing within each cell grade determined that there were no statistically significant differences in the percentage of healthy, damaged, or dead cells in any experimental conditions except the number of healthy cells in the Aβ:tau condition (**Figure 2.3 E**).

LDH assay indicates increased cell damage in response to Aβ42 treatment

With respect to the LHD data, (**Figure 2.4**) one-way ANOVA comparing absorbance levels of the samples, combining the data across all 12 h, determined there were statistically significant

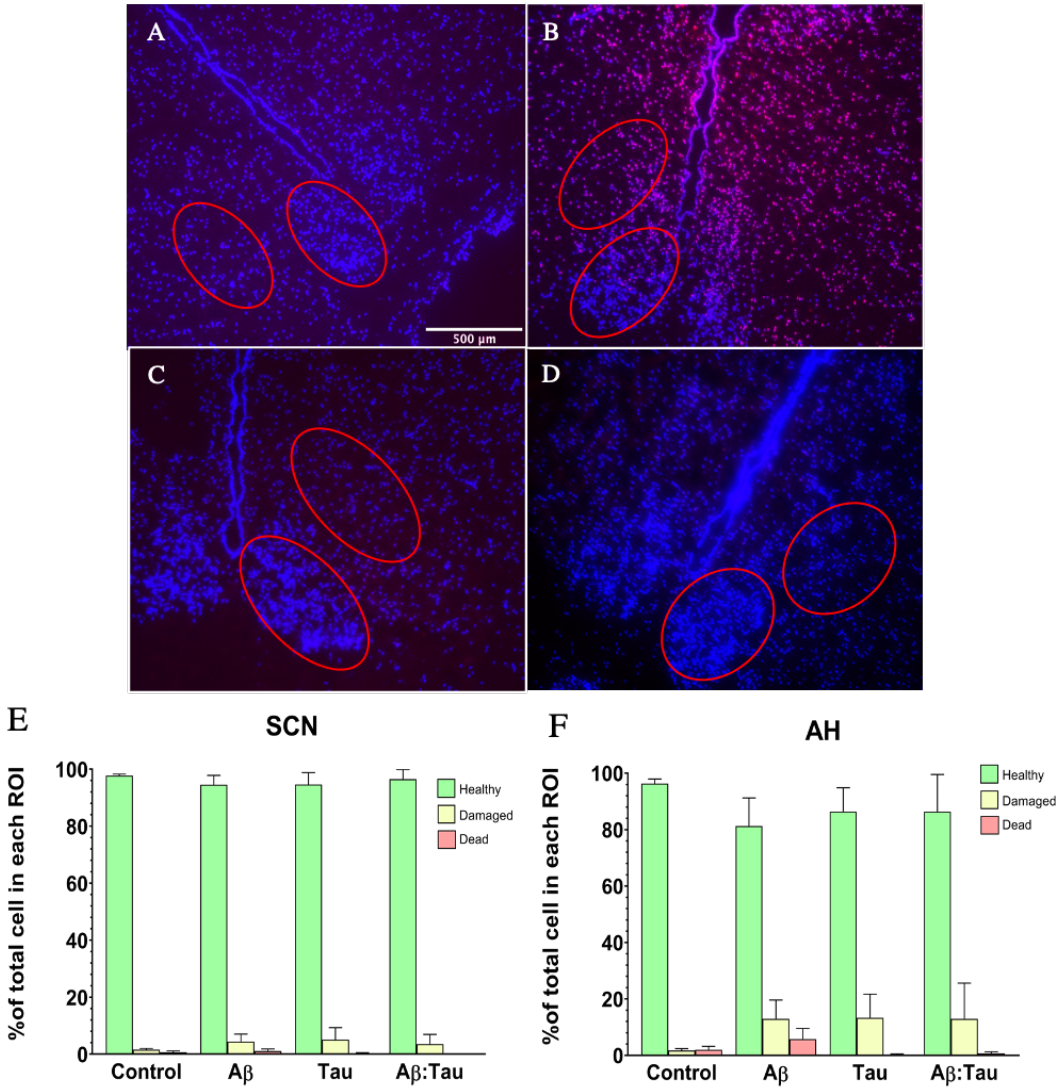


Figure 2.2 Comparison of cell death in the SCN and AH Example histological images showing DAPI (blue) and PI (red) stained cells in SCN/AH tissues slices for A) control, B) $A\beta_{42}$, C)Tau_{PHF43}, and D) $A\beta_{42}$ + Tau_{PHF43} conditions. Histogram graphs show quantification of dead, damaged, and healthy cells in the E) SCN and F) AH

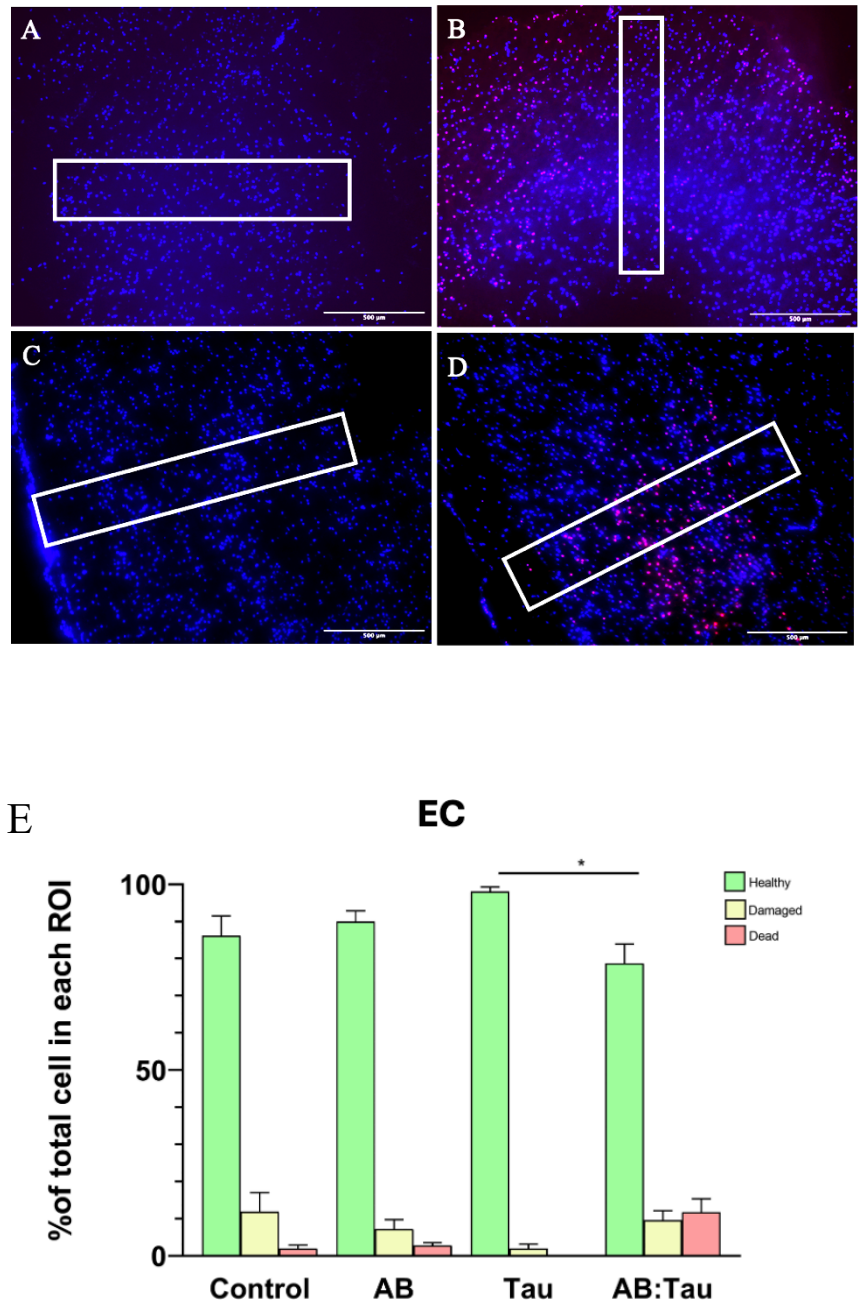


Figure 2.3 Comparison of cell death in the EC Example histological images showing DAPI (blue) and PI (red) stained cells in EC tissues slices for A) control, B) $A\beta_{42}$, C) Tau_{PHF43}, and D) $A\beta_{42}$ + Tau_{PHF43} conditions. E) Histogram graph shows quantification of dead, damaged, and healthy cells in the EC. (* = $p<0.05$)

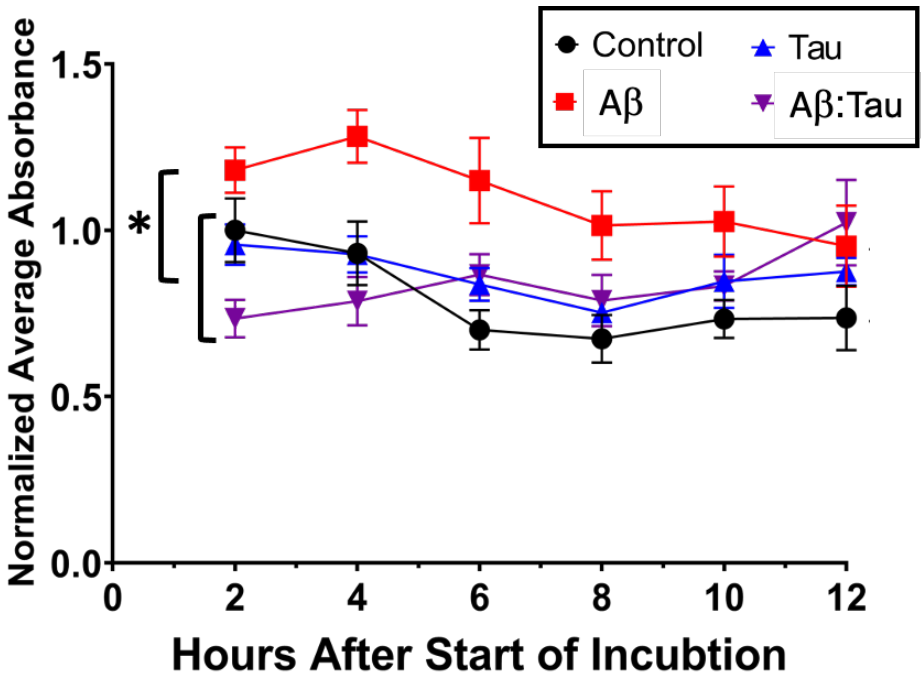


Figure 2.4 Quantified LDH release from the SCN Normalized average absorbance of formazan product over 12h produced in LDH assays for each experimental condition. (* = p <0.0001 $A\beta_{42}$ *vs*. each of the other three conditions)

differences. Pairwise comparisons indicated that significantly more LDH was released by SCN/AH tissue slices treated with $A\beta_{42}$ compared to control, Tau_{PHF43}, and the mixture of $A\beta_{42}$ and Tau_{PHF43}. In the EC (**Figure 2.5**), pairwise comparisons indicated the significantly more LDH was released by slices treated with Tau_{PHF43} or by control slices compared to other experimental conditions.

In comparing the two toxicity assays, although analysis of PI staining found no significant differences in cell health in either the SCN or AH when comparing across the peptide treatments, there appeared to be a minor, non-significant amount of cell damage in the AH that was not seen in the SCN, including an uptick in cell death in the AH with $A\beta_{42}$ exposure. Data obtained from the LDH cytotoxicity assay, however, found significant increases in cell damage after exposure to $A\beta_{42}$. Likewise, in the EC, PI staining indicated more cell damage with the mixture of $A\beta_{42}$ and Tau_{PHF43} but the LDH cytotoxicity assay found significant increases in cell damage with control tissues and after Tau_{PHF43} treatment. The difference in results of the two assays suggests that LDH release is a more sensitive marker of cell damage/death compared to PI staining. The LDH assay also has the advantage of providing information on changes in cell damage over time, while PI staining only provides information on the extent of cell damage at the time of PI incubation/tissue fixation. PI staining, however, provides critical information on regional differences within the tissue sections that cannot be obtained using the LDH assay. Thus, combining the two techniques gives insight into cellular recovery dynamics that might take place in tissue slices as well as regional specificity. Overall, the combined data suggest that $A\beta_{42}$ aggregation induces higher toxicity compared to either Tau_{PHF43} alone or when combined with Tau_{PHF43} and that the AH may be more susceptible to $A\beta_{42}$ toxicity than the SCN. The Jiang and Bitan groups showed that Aβ oligomers, but not monomers or fibrils, “primes” cells, making

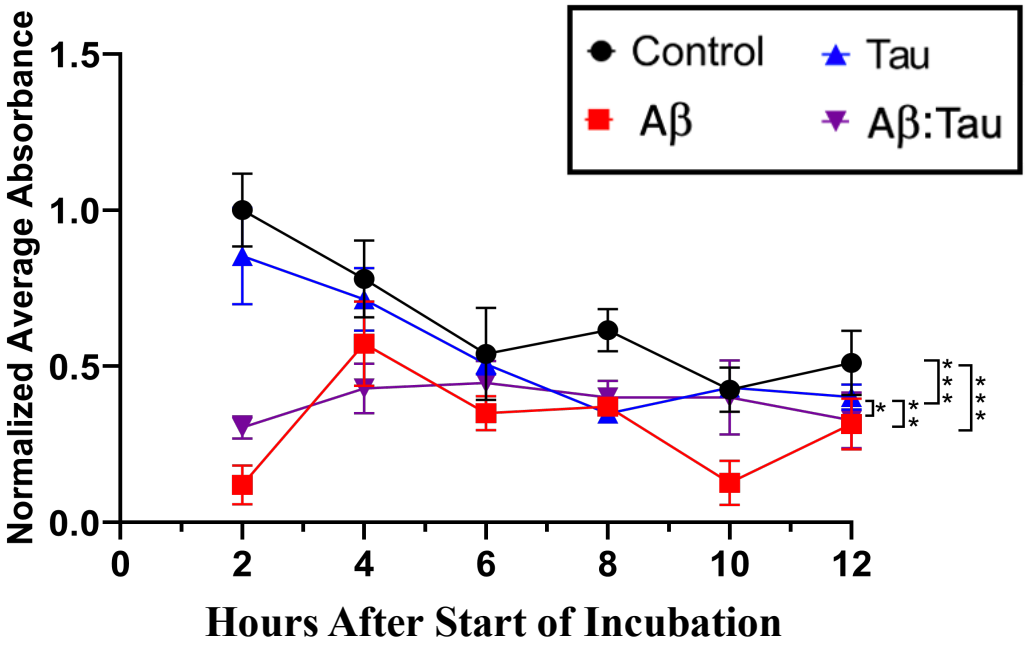


Figure 2.5 Quantified LDH release from the EC Normalized average absorbance of formazan product over 12h produced in LDH assays for each experimental condition. (* = p <0.05, ** = p <0.01, ***=p <0.001)

them more susceptible to tau seeding.[90] Luo and co-workers showed that tau protein blocks the aggregation of $A\beta_{40}$ *in vitro*, and that $A\beta_{40}$ remains in a random coil, monomeric form.[91] These findings suggest that the direct interaction of Aβ and tau is a lot more complicated than one protein promoting the aggregation of the other. Of note, because the viability assays studied cell states after hours of incubation, the toxicity was more likely due to $A\beta_{42}$ oligomers (or fibrils) than the monomers, since $A\beta_{42}$ by itself is known to quickly aggregate at room temperature, and these experiments were conducted at 37ºC. Nonetheless, the tissue data indicate that the mixture of $A\beta_{42}$ and Tau_{PHF43} is less toxic than $A\beta_{42}$, supporting the conclusion that interactions between the two peptides may induce protective effects and support our IMS-MS data.

Finally, it is noteworthy that the acute toxicity of $A\beta_{42}$ seen here is much less than when similar tissue slices were exposed for 4 h to KVKVLWDVIEV (G6W), an 11-residue mutant segment of αB crystallin.[83] The G6W peptide was shown to self-assemble into a novel dodecameric structure and is currently the most structurally sophisticated model of amyloid oligomers published. This suggests that neither $A\beta_{42}$ nor Tau_{PHF43} are exceedingly toxic to hypothalamic brain tissue upon initial exposure. It will be interesting in future studies to assess whether this changes with the age, sex, or genotype of the donor animal. Future experiments could also investigate whether CycA would decrease this initial toxicity of $A\beta_{42}$ in tissue slices.

Conclusion

In summary, we characterized a Tau construct (Tau_{PHF43}) previously reported by Mandelkow and co-workers[81] and investigated its interactions with $A\beta_{42}$ via IMS-MS and tested their toxic effects in acute brain slices. First, we showed that Tau_{PHF43} has a propensity to form cross-linked disulfide dimers. Previous studies have speculated on the importance of these cross-linked dimers in Tau pathology and toxicity. We were able to study the formation of higher ordered

oligomers formed from Tau_{PHF43} and examine them for the presence of disulfide bonds. The lack of disulfide bonds in these higher-ordered Tau_{PHF43} oligomers may help explain why the 3R Tau is less aggregation-prone than the 4R Tau. Upon elucidation of interactions between Tau_{PHF43} and $A\beta_{42}$, we saw that $A\beta_{42}$ has a high tendency to bind to Tau_{PHF43}. Surprisingly, we also found that $A\beta_{42}$ disrupted disulfide bonds of the Tau_{PHF43} dimers. Our data suggest that this may indicate a protective function of non-amyloidogenic Aβ species (monomer or small oligomers) on maintaining normal Tau function and making Cys-322 available for actin binding (**Figure 2.6**). Experiments with CycA, a lipophilic macrocycle known to disrupt β-sheet structures, support our hypothesis on the overlooked protective role of $A\beta_{42}$ monomer. Our toxicity experiments indicate that neither $A\beta_{42}$ nor Tau_{PHF43} peptides alone induce substantial cell damage or death during the first 12 h of tissue exposure, but that $A\beta_{42}$ by itself leads to significantly more damage than Tau_{PHF43} in the SCN and the two peptides combined induce more cell damage in the EC. This partially supports our hypothesis that $A\beta_{42}$ may abrogate Tau_{PHF43} toxicity, while at the same time showing minor toxicity induced by $A\beta_{42}$ and the peptide combination in a regionally specific manner. Compared to our work with other amyloid oligomers, it appears that neither $A\beta_{42}$ nor Tau_{PHF43} have substantial acute toxicity. Whether their toxicity increases with longer incubation times was not investigated here. Finally, the proposed positive effect of $A\beta_{42}$ is similar to the case of human islet polypeptide (hIAPP) in type 2 diabetes (T2D), another amyloid-related disease. In T2D, hIAPP is secreted from islet β-cells, and its aggregation[92] has been linked to β-cell destruction.[93–95] However, much therapeutic effort to target hIAPP aggregation failed to cure T2D. On the other hand, Pramlintide, an FDA-approved drug for T2D, is a non-amyloidogenic hIAPP analogue.[96,97] Thus, we may speculate that non-amyloidogenic Aβ analogues[98] may provide a new therapeutic approach toward AD treatments.

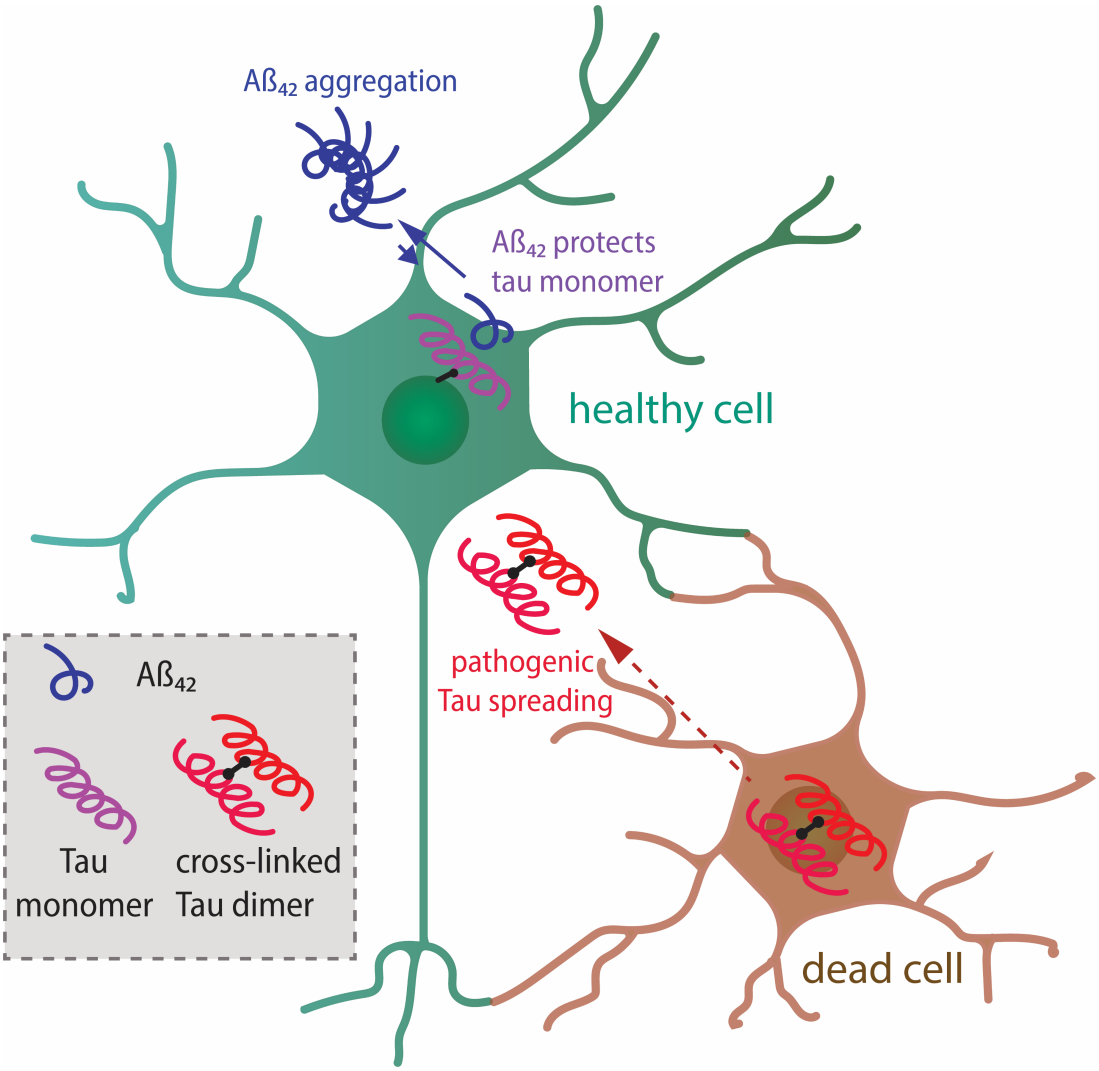


Figure 2.6 Summary schematic Our proposed hypothesis on $A\beta_{42}$ protecting Tau from disulfide-driven dimerization.

Chapter 3: Bubble perfusion brain slice culture with single-droplet stimulus delivery in a 3D printed microfluidic device

A version of this chapter was originally submitted by Genoveve G. Gutierrez, Richard J. Ortiz, Victoria Norman, Rebecca A. Prosser, and Christopher A. Baker.

Genoveve G. Gutierrez, Richard J. Ortiz, Victoria Norman, Rebecca A. Prosser, and Christopher A. Baker, "Bubble perfusion brain slice culture with single-droplet stimulus delivery in a 3D printed microfluidic device" *Submitted*, 2025

Abstract

Ex vivo tissue culture can model tissue physiology under well-controlled conditions and is especially promising for understanding the complex mechanisms of the brain. 3D printing has immense potential to accelerate microfluidic technology development, especially for *ex vivo* tissue culture devices where miniaturization is ultimately limited by the physical dimensions of tissue explants. Here we describe the development of a 3D printed microfluidic perfusion device for *ex vivo* brain slices that utilizes media droplets segmented by oxygen bubbles, a perfusion technique we call "bubble perfusion". Device design considerations are described, including materials property challenges associated with 3D printed plastic, such as wetting behavior and thermal conductivity challenges. Integrating a heated water circulation chamber and media prewarming chambers yielded media droplets delivered to brain slice explants at a temperature of 36.8°C ± 0.13°C, with tissue experiencing a temperature drift of 0.5 ± 0.09°C over the course of a 60 s media droplet exposure. Murine brain tissue explants containing the suprachiasmatic nucleus (SCN) or entorhinal cortex (EC) were observe d to be viable within the perfusion system by fluorescence imaging of intracellular Ca^{2+} flux induced by single-droplet stimulus of 60 mM KCl. Robust Ca^{2+} flux was observed for perfusion experiments lasting up to 12 hours, with sequential droplet observations indicating the temporal dynamics of Ca^{2+} responses. End-point propidium iodide staining was used to characterize the health of EC and SCN tissue, with *ca.* 60% of cells in both regions showing no sign of membrane damage after 12 hours of perfusion. The utility of the perfusion system towards pharmacological studies was demonstrated by comparing the Ca^{2+} flux induced by stimulus with 50 µM cannabidiol (CBD) *vs*. 50 µM anandamide (AEA). Interestingly, similar magnitude and temporal dynamics of Ca^{2+} flux were observed for both CBD and AEA stimuli despite differential proposed mechanisms of action with

respect to the cannabinoid receptor 1 (CB1). These studies demonstrate the utility of the 3D printed bubble perfusion system towards the study of receptor-binding ligands that induce relatively modest magnitudes of Ca^{2+} flux.

Introduction

Neurodegenerative diseases are characterized in part by dysfunction or loss of synapses and neurons, and formation of protein aggregates, which severely impact behavior and physiology.[99] Alzheimer's disease (AD) is the most common age-dependent neurodegenerative disease and is the most common cause of dementia in elderly people. An estimated 6.7 million Americans aged 65 and older are living with AD. By 2050, the number of people aged 65 or older living with AD is projected to grow to 12.7 million.[100] Initial AD neuronal dysfunction and cell death occur in areas associated with memory and cognitive processing such as the entorhinal cortex (EC).[22] AD patients commonly experience disruption in circadian rhythms, which influences various homeostatic functions, including disturbances with thermoregulation and sleep-awake cycles.[101–104] Additionally, circadian disruption becomes more severe as AD severity increases.[104,105]

In animal models, accumulation of Ab interferes with the expression of circadian clock-related genes.[23,106,107] Specifically, Ab accumulation has shown to alter expression patterns of the circadian clock genes *Bmal1* and *Per2*.[108] Therefore, age-related neuroendocrine degeneration and disruption of circadian rhythms have been proposed to have a consequential, bidirectional interaction[109,110] that require further examination.

Recent studies have shown that the G-protein coupled receptor cannabinoid receptor 1 (CB1) plays critical roles in various physiological and behavioral systems including memory formation,[111,112] nociception,[113] and energy homeostasis.[114] Centrally, CB1 is expressed in

various areas of the brain, including the suprachiasmatic nucleus (SCN), which acts as the body's central circadian timekeeper,[115] and the EC, which is involved in time perception.[116,117] CB1 activation has been shown to have an excitatory effect on SCN neurons by reducing GABA release,[116] affecting circadian light attenuation. Cannabidiol (CBD) is a phytogenic ligand of CB1 and an emerging pharmacotherapy for AD.[117] CBD has been found to be neuroprotective, to prevent hippocampal and cortical degeneration,[118] and to protect against Aβ neurotoxicity.[119,120]

Modeling microphysiological environments with the precision flow control of microfluidics has provided new understanding of biochemical signaling processes and accelerated drug discovery.[121–123] Emerging microfluidic technologies are enabling various *ex vivo* organ-on-chip models,[124] including brain, kidney, and heart tissue.[125] Integrating microfluidic perfusion systems with *ex vivo* tissue slices enables precise delivery of nutrients and various chemical stimuli. Additionally, perfusate sampling facilitates the analysis of tissue-secreted factors such as hormones and neurotransmitters.[126,127] These techniques together are especially promising steps toward understanding complex signaling in neural tissue.

A key challenge for maintaining brain tissue samples *ex vivo* is meeting the high oxygen demand of neuronal tissue without intact vasculature. The rotary-tube culture method was an early approach to addressing this challenge,[128] but while it provides adequate oxygen influx, the mechanics of rotary tube culture do not allow for real-time analysis by microscopy or electrophysiology. As such, rotary tube culture has largely been supplanted by membrane-interface culture methods, in which tissue slices are kept stationary on a porous membrane at a liquid-gas interface.[128] Porous membranes present a difficulty for microfluidic flow control, and the challenge of miniaturizing *ex vivo* brain slice culture to create brain-on-chip models remains an active area of research.

Our labs previously developed a brain-on-chip microfluidic device that mimicked the alternating oxygen and media delivery of rotary tube culture by delivering segmented flow of media droplets and oxygen bubbles in a method we called bubble perfusion.[129] The original bubble perfusion technology was limited by a need for specialized microfabrication, and by a continuous flow operation that increased total perfusion volumes despite the small volume of individual droplets. Here, we describe the development of a bubble perfusion system fabricated using accessible, consumer grade 3D printing technology, and designed for droplet-on-demand fluid delivery that reduces overall perfusion volumes. Single-droplet stimulus delivery was demonstrated in various experiments delivering KCl, anandamide, or CBD. Tissue responses to stimuli were observed via fluorescence imaging of Ca^{2+} flux in either SCN or EC tissue, and tissue health was assessed via end-point propidium iodide (PI) staining. Robust Ca^{2+} flux was observed in SCN and EC tissue for the full duration of perfusion experiments lasting up to 12 hours.

Materials and Methods

Design and operation of the perfusion system

Device architectures were designed in AutoCAD 2023 (Autodesk, San Francisco, CA). Devices were 3D printed using BioMed Clear resin on a Form 3B SLA printer (Formlabs, Somerville, MA). The tissue chamber was sealed using a 25 X 20 mm cover slip cut from GelBond® film (Lonza, Basel, Switzerland) adhered to the device using a double-sided adhesive gasket cut from 300LSE tape (3M, St. Paul, MN).

On-demand delivery of aqueous droplets and oxygen bubbles was achieved using a custom-built valving system (see supporting information, Figure S1). Briefly, 3D printed two-point pinch valves were supplied with pressurized oxygen and placed upstream of the perfusion

device. For bubble delivery, the pinch valve was connected directly to the perfusion device. For droplet delivery, a sealed 50 mL centrifuge tube was placed in-line between the pinch valve and the perfusion device. Metered volume delivery was accomplished by entrapping a defined volume of pressurized oxygen between the dual pinch points of the valve, then releasing this entrapped pressurized volume to flow towards the perfusion device. The metered volume was defined by the over pressure of the entrapped volume relative to atmospheric pressure and the volume entrapped between the two pinch points of each valve.

Temperature Characterization

Temperature characterization evaluated three factors: prewarming chamber volume, droplet hold time, and circulating water temperature. Prewarming chamber volume was evaluated at 19.5 μL, and 156 μL termed 1X, and 8X, respectively, for their relative volume to the tissue chamber. Droplet hold time was evaluated at 30 min, 1 min, and 15 min. Circulating water temperature was evaluated at 37 °C , 41 °C , and 45 °C. Experiments lasted approximately 2.5 hours allowing for both 1 and 30 minute droplet delivery times (n = 57 and n = 4, respectively). A miniature thermistor (TH10K, THORLABS, Newton, NJ) was sealed into the tissue chamber to record the response of temperature vs. time.

Hydrogel glue preparation

Hydrogel glue was synthesized following a protocol developed by Balakrishnan and colleagues,[130] and was used to immobilize tissue slices on the Gelbond cover slips. The two-part glue was comprised of Chitosan hydrochloride (ChitHCl) and Dextran dialdehyde (DDA).

ChitHCl preparation: 5 g of high molecular weight chitosan was mixed into 60 mL of 12M HCl and 40 mL of ethanol and allowed to stir at room temperature for 3 hours. The ChitHCl salt was filtered and washed with a 3:1 mixture of acetone-water and dialyzed against ultrapure

water until no precipitate appeared when 1 wt% silver nitrate was added to the dialysate dropwise. The ChitHCl solution was dried to a pellet by vacuum centrifuge and stored at -20 °C until needed.

DDA preparation: 5 g of dextran and 4.5 g of sodium metaperiodate was mixed with 100 mL of ultrapure water for 6 hours while protected from light. 5 mL of the solution was dialyzed against milli-Q water until no precipitate appeared when 1 wt% silver nitrate was added to the dialysate dropwise. The DDA solution was dried to a pellet by vacuum centrifuge and stored at -20 °C until needed.

Tissue slice preparation

Coronal brain slices of approximately 400 – 500 μm thickness containing the SCN and surrounding anterior hypothalamus or the EC were collected from adult male C57BL/6 mice (Prosser Lab) or 10 – 12 week-old female Swiss Webster mice (Baker Lab). All animals were housed in 12 h light : 12 h dark conditions with food and water provided ad libitum. Tissue slices were initially placed in an interface brain slice chamber with Hank's Balanced Salt Solution (HBSS, pH:7.4, Baker Lab) or Earle's Balanced Salt Solution (EBSS, pH:7.4, Prosser Lab) and aerated with 100% O_2 (Baker Lab) or 95%O_2/5%CO_2 (Prosser Lab) for 30 minutes.

Prior to transferring to the perfusion device, tissue slices were incubated in balanced salt solution supplemented with 20 μM (Baker Lab) or 50 μM (Prosser Lab) Calbryte 520 AM (AAT Bioquest, Pleasanton, CA) and 1% pluronic acid, then protected from light for 45 - 60 minutes. The dye-loaded tissue was washed by incubation in fresh balanced salt solution prior to loading into the perfusion device.

Working solutions of 10 wt% DDA in phosphate buffered saline and 5 wt% of ChitHCl in ultrapure water were prepared. 4 μL of each working solution were combined into a single

droplet on the Gelbond cover slip, and the tissue slice was immediately placed onto the glue droplet. The cover slip was sealed to the perfusion device to load the tissue into the tissue chamber.

Drug-stimulated Ca^{2+} response measurements

Experiments evaluating SCN response to drug stimuli were conducted in the Baker Bioanalysis Lab. Alternating oxygen bubbles and aqueous droplets containing HBSS were delivered to the tissue chamber, with each bubble or droplet held stationary on the tissue for 60 seconds before being evacuated by the subsequent droplet or bubble. This pattern of media and oxygen delivery was maintained for the full duration of each perfusion experiment (8 - 12 hrs). Once per hour a single stimulus droplet was delivered which was comprised of HBSS supplemented with 60 mM KCl, 50 μM anandamide (AEA), or 50 μM CBD.

Fluorescence image sequences were collected using an upright fluorescence microscope (BX41, Olympus, Tokyo, Japan) outfitted with a 488 nm laser excitation source (Sapphire-100, Coherent) and sCMOS camera (Kiralux, Thorlabs, Newton, NJ). Image sequences were collected for 6 HBSS droplets prior to the stimulus droplet ("pre-stimulus"), the stimulus droplet, and 4 HBSS droplets following the stimulus droplet ("post-stimulus"). Images were collected with a field of view of several hundred μm^2, giving physiological-level, but not cellular-level, spatial resolution. Quantitative processing of fluorescence images is illustrated in the supporting information. Briefly, fluorescence vs. time profiles were extracted from image sequences using ImageJ[131] to define a region of interest corresponding to the tissue region of study, keeping only image data collected during the interval when an aqueous droplet filled the tissue chamber. Non-linear background drift resulting from photobleaching, and dye leakage was fit to a single-phase exponential decay, and the fluorescence *vs.* time profile of the full droplet sequence was divided

by the exponential decay fit to give the signal-to-background ratio profile for each droplet. The mean profile for all pre-stimulus droplets was calculated to give the intra-droplet baseline profile. Finally, the intra-droplet baseline profile was subtracted from each droplet's signal-to-background ratio profile to get the baseline-subtracted signal-to-background ratio profile of each droplet.

Comparison of EC and SCN tissue

Comparisons of EC and SCN tissue were conducted by the Prosser Lab. Alternating gas bubbles and aqueous droplets were delivered consecutively to the tissue chamber using various droplet pause times but maintaining the 60 second pause time for oxygen bubbles. Preliminary experiments indicated that droplet pause times up to 8 minutes maintained robust Ca^{2+} responses for at least 12 hours; thus, tissue comparison experiments used 8-minute droplet pause times for droplets delivered between stimulus sequences.

Tissue slices were stimulated with 60 mM KCl at 1, 6, and 12 hours of perfusion time. Each stimulus sequence included observations for 4 pre-stimulus, 1 stimulus, and 4 post-stimulus droplets. During the stimulus sequence, droplet pause times were decreased to 1 minute, and a series of time-lapsed images, one every 5 seconds, was taken of the tissue. Fluorescence image sequences were collected using an upright fluorescence microscope (BH-2, Olympus, Tokyo, Japan) outfitted with a 488 nm laser excitation source (GH04850B2G, Sharp Corp., Osaka, Japan) and sCMOS camera (FMA050, AmScope, Irvine, CA).

After 12 hours of perfusion, slices were transferred to an interface brain slice chamber and perfused for 2 hours with EBSS containing 4.6 μg mL^{-1} PI. Following PI loading, slices were fixed in 4% PFA for 10 minutes then transferred to 30% sucrose overnight at 4°C. Slices were embedded in optimal cutting temperature (OCT) compound and stored at -80°C. 25 μm sections

were cut using a cryostat and mounted to gelatin subbed slides and stored at -80°C. Slides were thawed at room temperature and washed three times for five minutes each with phosphate-buffered saline (PBS). Coverslip media containing 4',6-diamidino-2-phenylindole (DAPI) was added to the surface of slides before they were cover slipped and sealed with nail polish.

Fluorescence images were acquired via 10x objective using a Leica DM6000B microscope and analyzed using ImageJ software. One image was analyzed for each tissue slice, and a region of interest (ROI) was drawn to contain either the entire SCN or a portion of the EC within that section. The images were split into blue and red channels to isolate DAPI-stained cells and PI-stained cells, respectively. Within each ROI, the total number of cells were counted using the DAPI image, and the PI was assessed in the same ROI. The ImageJ thresholding feature was used to differentiate between high PI intensity cells corresponding to dead cells, moderate PI intensity indicating damaged cells, and cells with minimal PI staining, considered healthy cells.[86,87,132]

Results and Discussion

Device design

The final design of the 3D printed bubble perfusion device is shown in **Figure 3.1**. Transitioning from microfabrication in PDMS/glass to SLA 3D printing presented challenges related to materials properties. First, we anticipated a substantial reduction in thermal conductivity for SLA printed plastics as compared to the previously employed glass substrates. Whereas glass devices can rely on simple resistive stage heaters, the 3D printed perfusion system integrated a 10.6 mL water circulation chamber for on-device thermal management. This approach utilized the thermal mass of circulating water to achieve a stable temperature

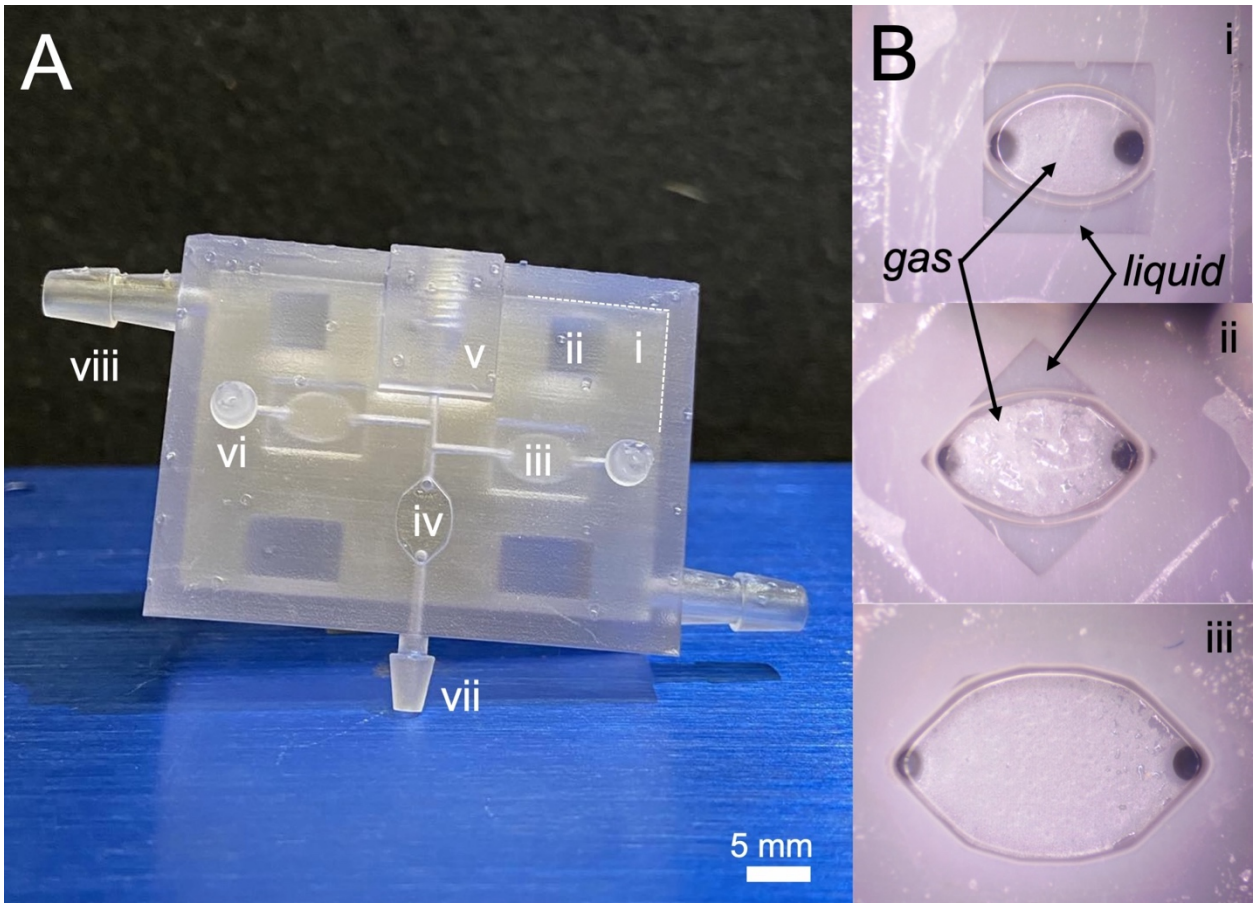


Figure 3.1 Perfusion Device Design A. A photograph illustrating the final perfusion device design including water circulation chamber(i), internal structural supports (ii), media prewarming chambers (iii), tissue culture chamber (iv), finger tight threaded port for gas inlet (v), and barbed connectors for two media/stimulus inflows (vi), perfusate outflow (vii), and heated water circulation (viii). **B.** Micrograph illustrating uncleared droplet solution remaining in the chamber for square (i) and 45 rotated (ii) tissue chambers. Minimal uncleared droplet solution was observed for the lemon geometry (iii), which mimicked the spontaneous wetting behavior observed in ii

equilibrium within the culture volume. Temperature characterization using this strategy is discussed below.

Another key challenge was the difference in surface energy between the 3D printed plastic substrate and the previously employed PDMS/glass materials, which ultimately influences wetting behavior within the tissue culture chamber. Complete clearing of the tissue chamber of each media droplet by the subsequent gas bubble is important to ensure removal of metabolic waste products, and to maintain temporal sampling fidelity in downstream droplet analyses. In our previous work, we achieved effective tissue chamber clearance by identifying several empirical "best practices" for tissue chamber design, but we were unable to identify a specific model to relate design parameters (such as geometry and material) to droplet clearance behavior. In the 3D printed device, the previously identified best practices did not translate to the plastic substrate material. **Figure 3.1** shows the evolution of tissue chamber design, highlighting the retained volume of a previous droplet after a bubble had filled the chamber. The initial chamber design was identical in geometry to that employed in our previous work, however here we observed retention of a substantial fraction of the droplet volume. Rotating the chamber geometry by 45° showed little improvement. The chamber geometry was then modified to mimic the inherent wetting behavior observed in the sub-optimal geometries, resulting in what we called the lemon geometry, which showed effective droplet clearance of droplets. One drawback to this approach was the need to scale the lemon geometry up slightly to facilitate the dimensions of a typical tissue slice. This resulted in increased chamber volume, from 12 μL for the square geometries to 19.5 μL for the lemon geometry, although this volume does not consider the volume occluded by tissue slice samples housed within the chamber. Future work may address large chamber volumes with refinements to the tissue preparation procedure, but we

anticipate that tissue dimensions will remain the limiting factor for volume reduction in this and similar perfusion systems for brain slice culture.

Temperature characterization

Figure 3.2 shows the temperature profiles of droplets delivered to the tissue chamber and held static within the chamber for 60 seconds, with circulating water heated to 37 °C. Our initial perfusion design delivered room temperature perfusion media, which warmed only as it transited through the delivery channels prior to entering the tissue chamber. In that design, media droplets largely came to temperature within the tissue chamber, showing a profile of steadily increasing temperature spanning 2.3 ± 0.21 °C. To reduce temperature variation within the tissue chamber, media holding volumes, referred to as prewarming chambers, were added to the device prior to the tissue chamber. Prewarming chambers were evaluated at equal volume and eight times the volume of the tissue culture chamber. The range of temperature variation was reduced with prewarming chambers to 0.4 ± 0.05 °C for the 1X prewarming chamber, and 0.7 ± 0.04 °C for the 8X prewarming chamber.

Importantly, circulating 37 °C did not provide the desired chamber temperature of 37 °C, and subsequent calibration (data not shown) revealed that a circulating water temperature of 45 °C was required to reach 37 °C within the tissue chamber. Operating with circulating water >37 °C presented the potential of over-heating the media in prewarming chambers, which was of particular concern when delivering stimulus droplets after lengthy residence times in the prewarming chamber. Therefore, we evaluated the 60 second temperature profiles of droplets with 1 minute and 30-minute residence times in the prewarming chambers. With circulating water heated to 37 °C, droplets with one-minute residence time in the prewarming chamber were measured as 31.3 ± 0.06 and 31.6 ± 0.08 °C within the tissue chamber, for 1x and 8x prewarming

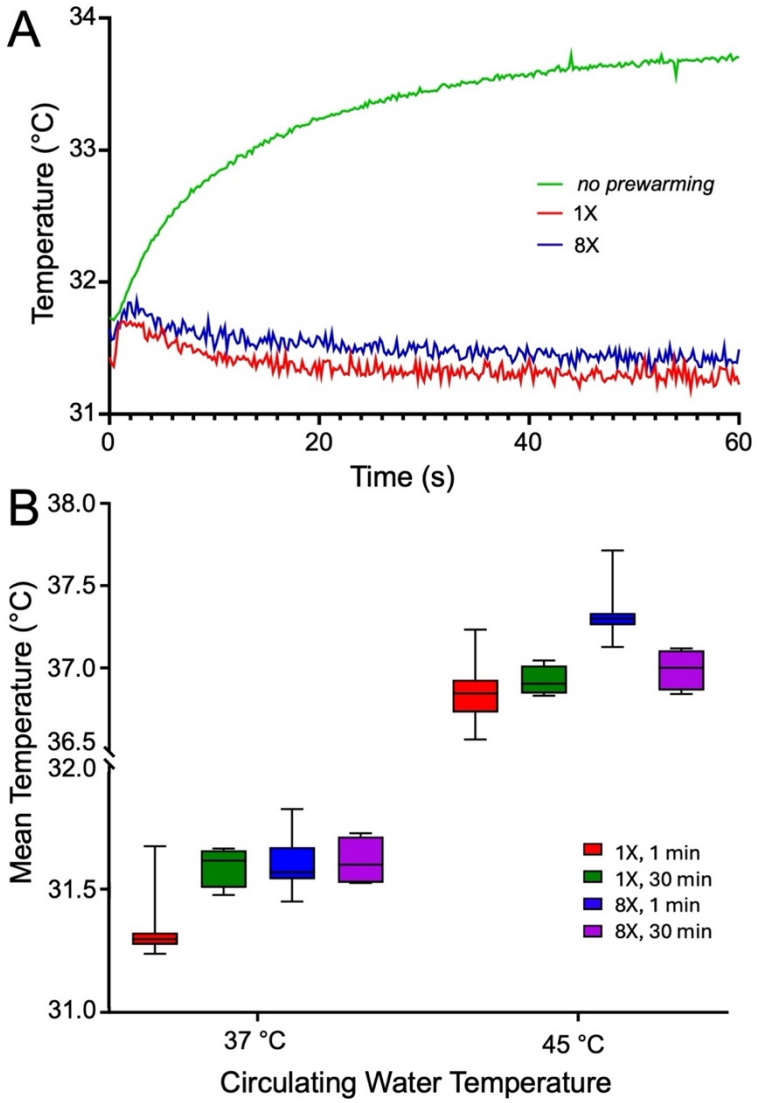


Figure 3.2 Temperature control characterization A. Representative temperature vs. time profiles measured within droplets delivered to the tissue culture chamber in device designs with no media prewarming chamber (green), and prewarming chambers with volumes of 1X (red) and 8X (blue) that of the tissue culture chamber. Profiles were measures with a circulating water temperature of 37 °C. **B.** Mean temperature of the 60 s droplet temperature profile for 1X and 8X designs vs. the temperature of water circulating through the integrated water circulation chamber. Profiles were measured for droplets delivered after 1 minute holding time in the prewarming chamber (n = 57 for each condition), and after 30 minutes holding time (n = 4 for each condition). Boxes indicate the central 50th percentile of observed values, whiskers indicate the full range.

chambers respectively (n = 57). Droplets with 30-minute prewarming residence times yielded 31.6 ± 0.08°C, 0.10 °C for both prewarming chamber volumes (n = 4).

With circulating water heated to 45 °C, one-minute prewarming residence times yielded 36.8 ± 0.13 °C and 37.3 ± 0.08 °C, for 1x and 8x designs respectively (n = 57). 30-minute residence times yielded 36.9 ± 0.09 °C and 37.0 ± 0.13 °C for 1x and 8x designs respectively (n = 4).

Intra-droplet temperature stability was characterized with 45 °C circulating water by observing the trend of temperature versus time for droplets held in the tissue chamber for 60 s. Temperature stability was summarized by the range of temperature drift over the course of 60 s (**Figure 3.3**). With 1 min prewarming residence time, temperature ranges were 0.5 ± 0.09 °C and 1.5 ± 0.14 °C for 1x and 8x designs, respectively (n=57). Temperature range for 30 min prewarming residence time were 0.7 ± 0.01 °C and 1.4 ± 0.13 °C for 1x and 8x designs, respectively (n=4).

With 45 °C circulating water, the 1X prewarming chamber design showed no statistical difference in either mean temperature or range of temperature drift between prewarming residence times of 1 or 30 minutes. This suggests that with the 1X prewarming chamber and water circulation at 45 °C, droplets delivered to the tissue chamber were at appropriate physiological temperature and were near thermal equilibrium. Thus, the risk of overheating or thermal shock to the tissue slices were low under these conditions. Importantly, this result illustrates that media droplets delivered with relatively short prewarming residence time (i.e. 1 - 2 min) and stimulus droplets with much longer prewarming residence times (i.e. 30 - 60 min) can be prewarmed in chambers of identical volume, simplifying device design and operation.

The 8X prewarming chamber design showed reduced temperature stability compared to the 1X design. This may result from increased interfacial area between the prewarming chamber

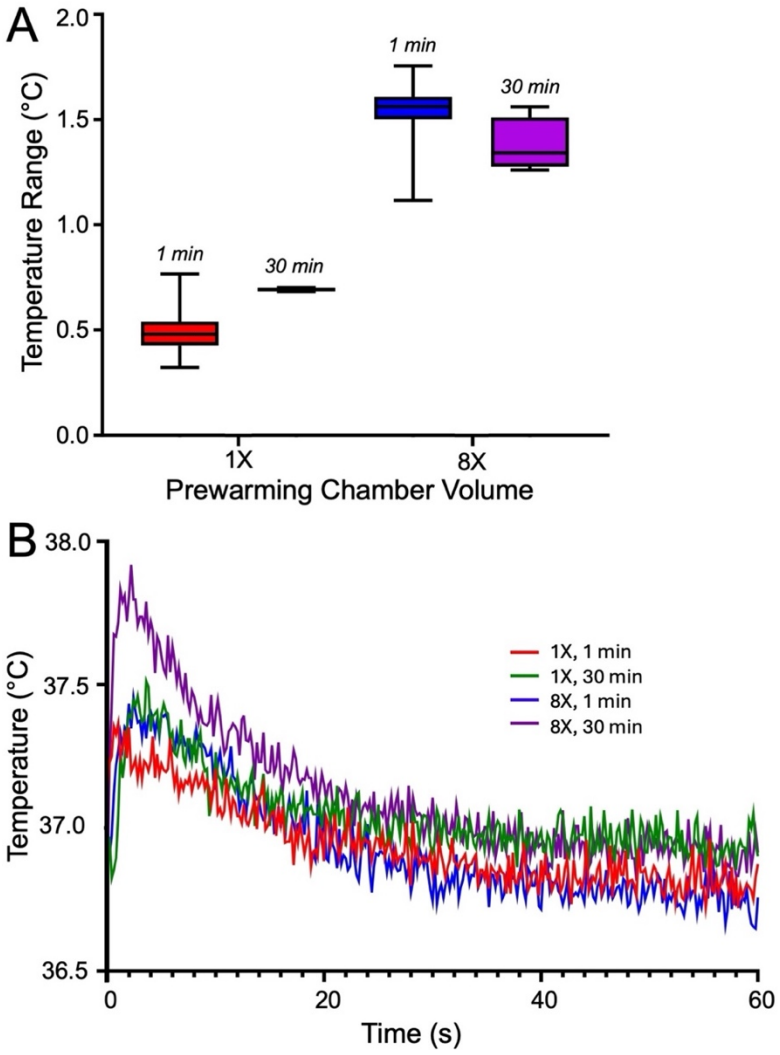


Figure 3.3 Temperature stability characterization A. The magnitude of the temperature drift over 60s ("Temperature Range") for droplets delivered to the tissue culture chamber from 1X and 8X prewarming chambers with circulating water set at 45 °C. Holding times in the prewarming chamber are indicated. n = 57 for conditions with 1 min holding time, n = 4 for conditions with 30 min holding time. Boxes indicate the central 50th percentile of observed values, whiskers indicate the full range. **B.** Representative temperature vs. time profiles for droplets delivered to the tissue culture chamber with a circulating water temperature of 45 °C

and water circulation chamber, which would alter the thermal equilibrium, although further work would be needed for such a conclusion. Still, no benefit was evident to indicate the use of an 8X prewarming chamber design, and the 1X chambers were incorporated into the final device design. The final design of this perfusion device can be accessed via the NIH 3D print exchange under model number 3DPX-021779.

Evaluation of tissue viability

To evaluate the efficacy of the perfusion system for maintaining viable brain tissue slices, intracellular calcium changes were measured in response to a depolarizing chemical stimulus. Tissue slices containing the SCN were loaded with Calbryte 520 AM prior to 10 – 12-hour perfusion experiments. Tissue was perfused with alternating HBSS droplets and oxygen bubbles. Depolarization was induced by delivering a single droplet containing HBSS supplemented with 60 mM KCl. Fluorescence intensity *vs.* time was monitored within the SCN tissue for six droplets prior to KCl stimulation (**Figure 3.4,pre-stimulus**), the single stimulus droplet (**Figure 3.4, stimulus**), and four droplets after stimulation (**Figure 3.4, post-stimulus**). Fluorescence profiles observed after 30 minutes (**Figure 3.4A**) and 12 hours (**Figure 3.4B**) of perfusion indicated that tissue remained responsive to the depolarizing stimulus for at least 12 hours in the device. We have shown previously that robust KCl-induced intracellular Ca^{2+} increases are well-correlated with end-point PI staining to indicate a low level of cell death in the calcium responsive tissue.[129]

Figure 3.4C shows the change in baseline subtracted fluorescence for the droplet sequence starting with the final Pre-stimulus droplet for 6 stimulus experiments across 3 tissue

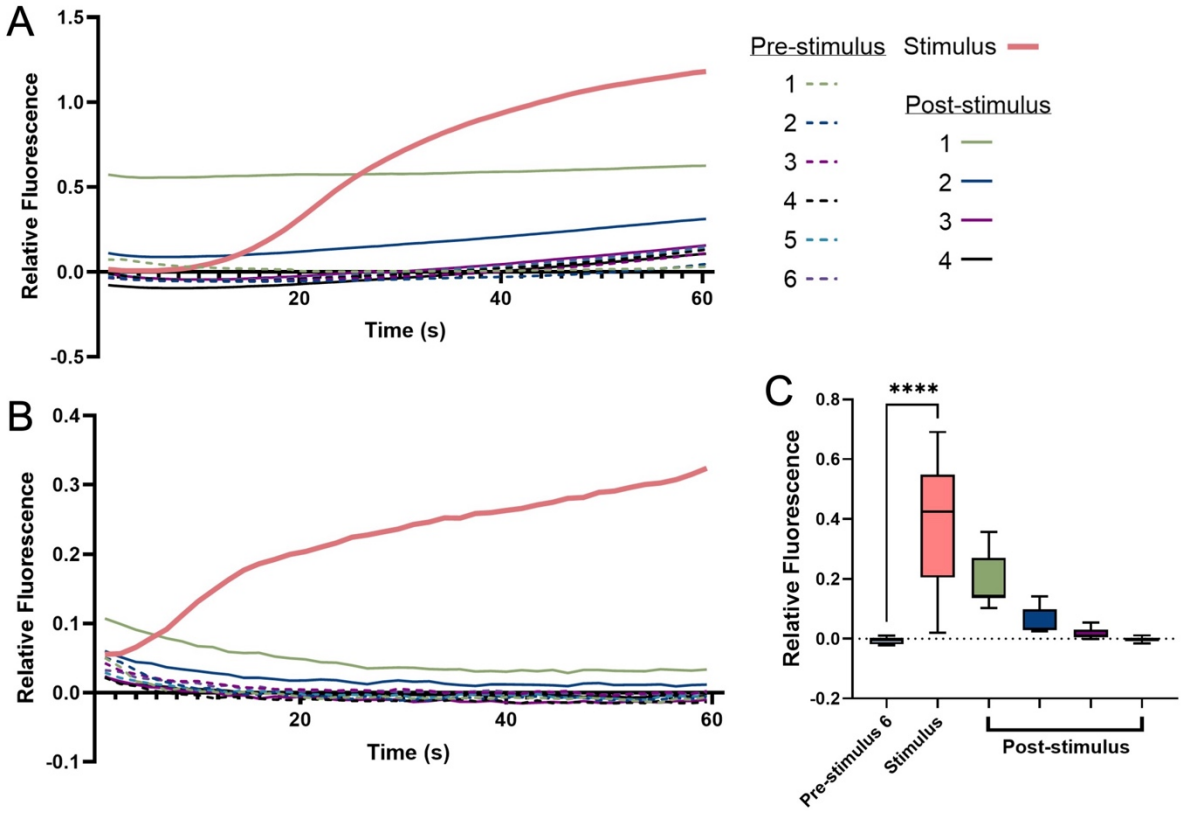


Figure 3.4 KCl-induced Ca^{2+} response in SCN tissue slices A. Baseline subtracted fluorescence of Calbryte 520-loaded SCN tissue vs. time for 6 pre-stimulus droplets (HBSS), 1 stimulus droplet (HBSS + 60 mM KCl), and 4 post-stimulus droplets (HBSS) delivered after 30 minutes of tissue perfusion. **B.** The same experiment described for panel A, but for stimulus delivered after 12 hours of perfusion. **C.** Summary of KCl-induced Ca^{2+} response from 23 stimulus deliveries performed across 3 tissue samples, with each perfusion experiment lasting 10 - 12 hrs. Only the final pre-stimulus droplet is shown in the summary for figure clarity. Boxes indicate the central 50th percentile of observed values and whiskers indicate the full range. **** $p < 0.0001$

preparations. Since droplets are delivered at regular intervals of once every 120 s, the sequential droplet comparison illustrates the temporal dynamics of intracellular Ca^{2+} levels in the SCN tissue slices, with a return to baseline [Ca^{2+}] within 3 - 4 post-stimulus droplets.

Comparison of EC and SCN tissue health

Tissue slices containing the SCN or EC were loaded with Calbryte 520 AM prior to 12-hour perfusion experiments. Depolarization was induced by delivering a single droplet of EBSS supplemented with 60mM KCl at 1, 6 and 12 hours. Fluorescence intensity *vs.* time was monitored for four pre-stimulus droplets, the single stimulus droplet, and four post-stimulus droplets for 3 tissue preparations of each EC and SCN tissue (**Figure 3.5, A and B, respectively**). Interestingly, although in all cases the KCl induced significant intracellular Ca^{2+} flux, differences in the magnitude and duration of the changes are apparent between the SCN and EC, and between the SCN tissue studied in the Prosser lab vs the Baker lab. The reasons for these differences are unclear, although between-lab differences may be influenced by differences in optical efficiency of the relative imaging systems, differences in perfusion media used, or biological differences between the tissue donor animals. Further investigation may be warranted. To corroborate evidence of tissue health observed by fluorescence Ca^{2+} imaging, end-point PI staining was performed following 12-hour perfusion experiments. Slices were removed from the tissue chamber and perfused with PI to identify dead and damaged cells. After fixation, tissues were imaged, and PI-stained cells were counted in defined ROIs corresponding to the tissue regions of interest. **Figure 3.6** shows the quantitation of healthy, damaged, and dead cells for the EC and SCN regions.

Observations of depolarization-induced Ca^{2+} flux in the SCN and EC provide three important insights. First, the ability of SCN and EC brain slice tissues to maintain robust

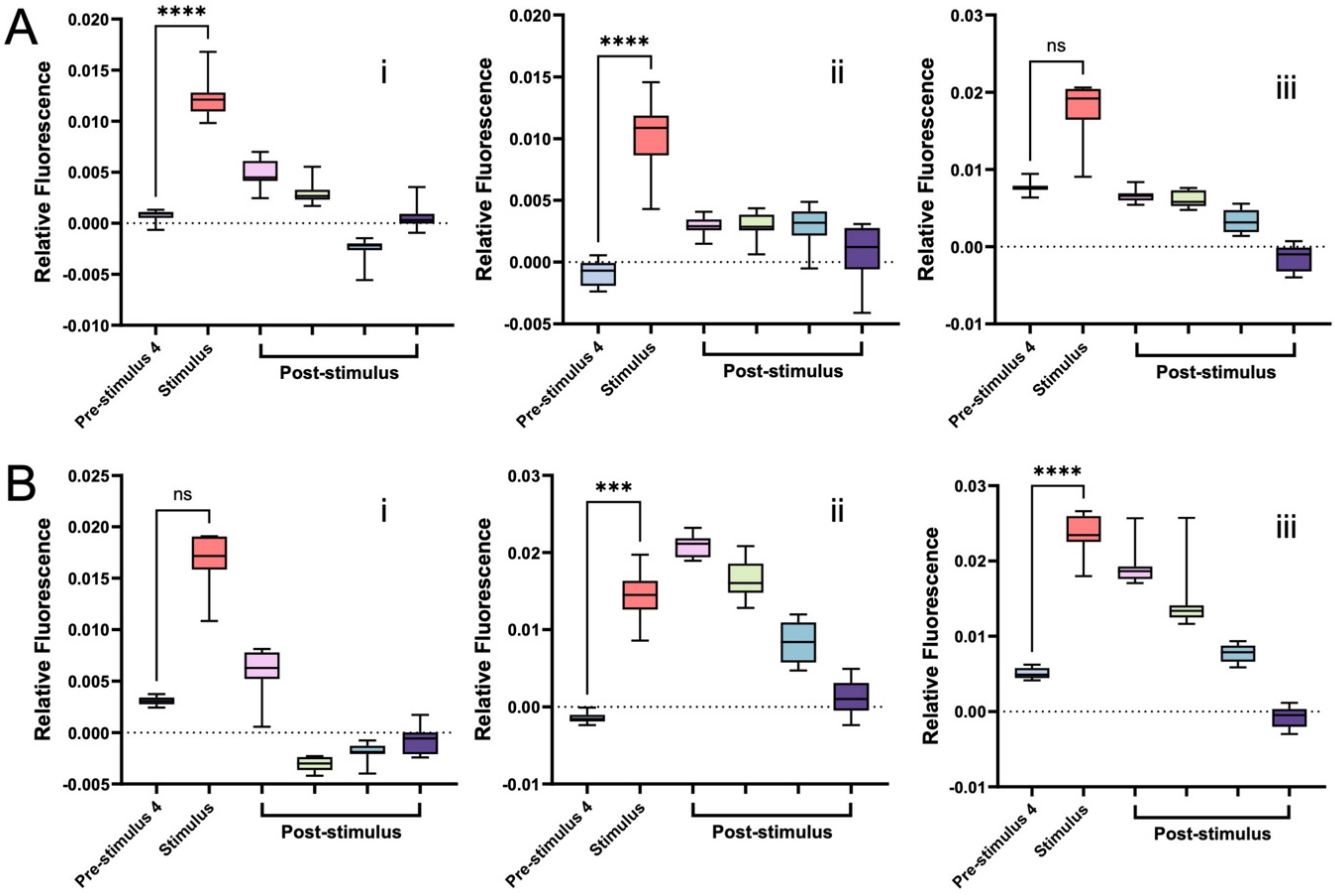


Figure 3.5 Comparison of Ca^{2+} response in EC and SCN tissue A. Summary of Ca^{2+} response in EC tissue induced by delivery of 60 mM KCl after 1 hour (i), 6 hours (ii), and 12 hours (iii) of perfusion. Each dataset pools observations from three tissue slices. **B.** The analysis is identical to A, but summarizing Ca^{2+} response in SCN tissue. ***$p < 0.001$, ****$p < 0.0001$, ns = $p > 0.05$

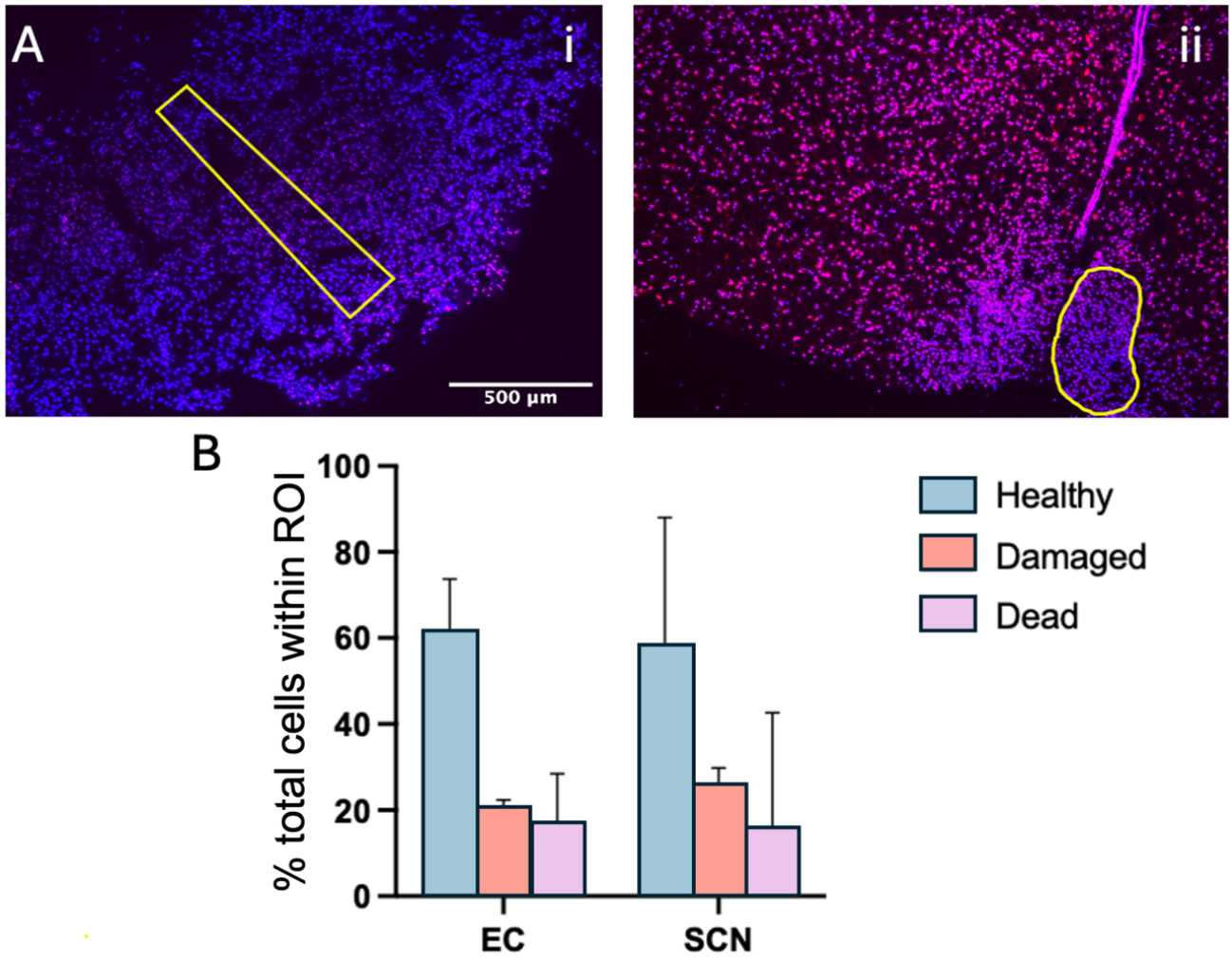


Figure 3.6 Endpoint health of EC and SCN tissue A. Representative fluorescence images showing typical ROIs (shown in yellow) used for EC (i) and SCN (ii) analyses. Tissue samples were PI stained and PFA-fixed after 12-hour perfusion experiments, then imaged by fluorescence microscopy with additional DAPI staining. **B.** PI intensity analysis in conjunction with PI/DAPI ratio revealed the percentage of healthy, damaged, and dead cells in the tissue region of interest. Data represents pooled observations from 3 tissue samples for each region

depolarization-induced Ca^{2+} flux demonstrates that the 3D printed bubble perfusion device is suitable for maintaining viable brain slices from different brain regions for at least 12 hours. The histological data using PI staining confirms the robust health of the tissues at the end of the 12-hour perfusion experiments, with EC tissue and SCN tissue showing comparable distributions of healthy, damaged, and dead cells. Combining both assessments, we observed no indicators that 12 hours represents a physiological limit, but rather a pragmatic limit of perfusion experiments that were not designed around unsupervised automation. Therefore, we anticipate that future work with this system will readily extend into assaying important physiological phenomena in *ex vivo* tissues, such as those investigating neural plasticity responses of the EC or circadian functions of the SCN on 12 - 24-hour timescales. Second, the ability for on-demand delivery of individual stimulus droplets enabled a time-resolved picture of depolarization-induced changes in intracellular [Ca^{2+}]. We anticipate this capability will be useful for evaluating other dynamic responses in brain tissues, such as time course profiles of short duration drug stimuli. Third, the extended droplet pause times utilized when comparing EC to SCN slices may offer a straightforward approach to enriching the concentration of cellular secretions in future applications focused on downstream analysis of droplet contents.

Drug stimulus studies

KCl-induced depolarization studies demonstrated the efficacy of the perfusion system for maintaining viable brain slices and established a method to analyze temporally resolved measures of stimulus-induced Ca^{2+} flux in SCN tissue. To demonstrate the utility of the perfusion and imaging system towards more selective mechanisms of chemical stimulus, such as via receptor-mediated cell activation, we applied the same methodology described for KCl stimulus

to compare the Ca^{2+} response induced by CB1 receptor ligand CBD to that of the endogenous CB1 ligand anandamide (AEA).

Figure 3.7 shows the Ca^{2+} response of SCN tissue stimulated with 50 μM AEA or CBD. Each tissue slice preparation was stimulated with both AEA and CBD, at alternating 60-minute intervals, to prevent aliasing slice-to-slice variability with real differences in stimulus response. For both CB1 ligands, measurable Ca^{2+} flux was observed in SCN tissue. A comparison of the sequential droplet profile of AEA and CBD-induced activation (**Figure 3.7C**) shows similar dynamics both in terms of the magnitude of stimulus-induced Ca^{2+} increase and the time-course of recovery.

The similarities in Ca^{2+} response between AEA and CBD is curious, since AEA is a CB1 receptor agonist while CBD has been shown to be a CB1 receptor antagonist.[133] This may suggest that the dominant mechanism of action of CBD within SCN tissue is not via CB1 antagonism. We hypothesize that the observed CBD-induced Ca^{2+} flux may be via TRPV1 receptor activation,[134–136] but further work beyond the scope of this technology development report is needed to resolve differential mechanisms of CBD and AEA activation in the SCN. Still, these results illustrate that despite more subtle and selective mechanisms of activation yielding relative fluorescence intensity changes more than an order of magnitude lower than those observed for broad depolarization by KCl, statistically significant increases in Ca^{2+} flux were observed for both AEA and CBD stimulation. This demonstrates the perfusion system as an appropriate platform technology for developing further drug stimulus and response studies such as those needed to resolve mechanistic differences between AEA and CBD stimulus in the SCN.

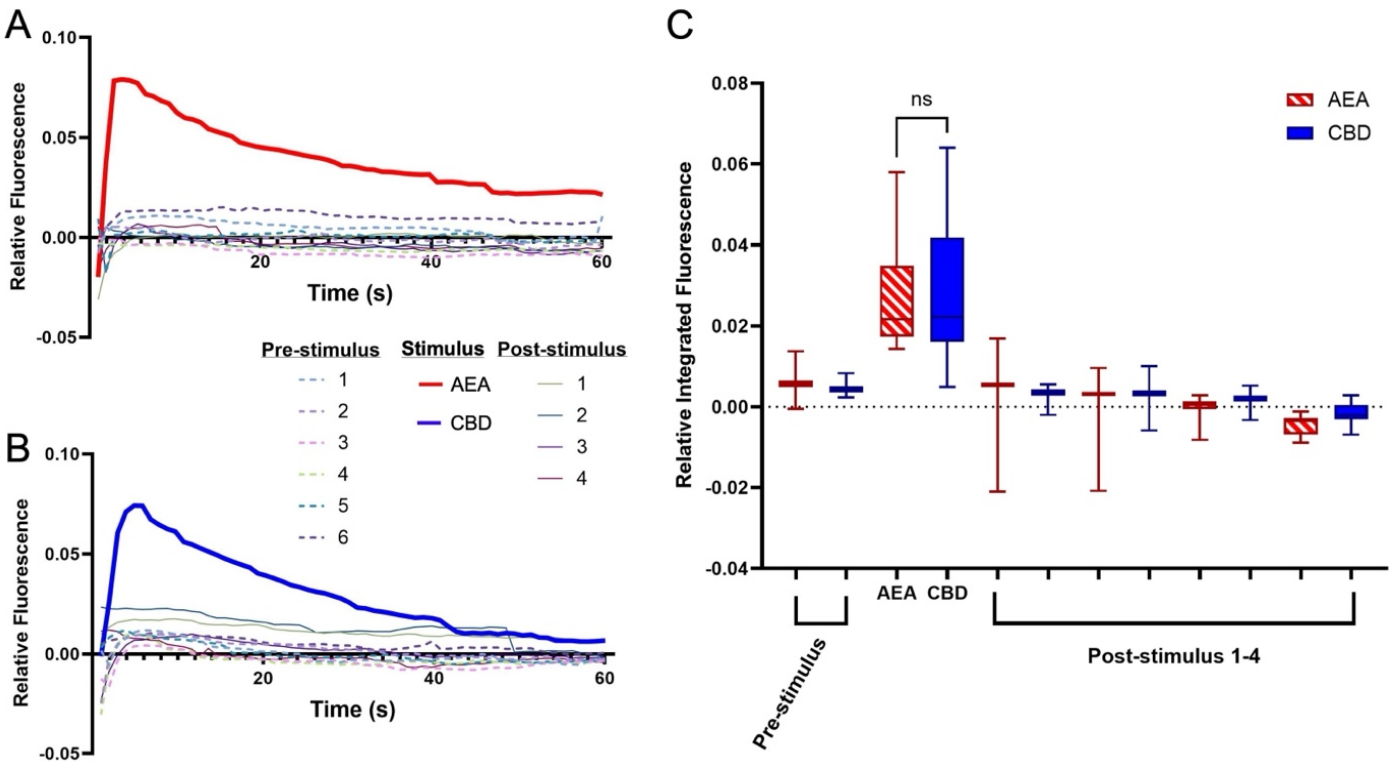


Figure 3.7 Comparison of Ca^{2+} response induced by AEA and CBD Representative fluorescence vs. time traces illustrate Ca^{2+} response in SCN tissue induced by delivery of **A.** 50 μM AEA; or **B.** 50 μM CBD. **C.** Summary of AEA and CBD-stimulated Ca^{2+} responses overserved across 3 tissue perfusion experiments, with each tissue sample receiving both AEA and CBD stimuli. n = 9 for AEA stimulus; n = 8 for CBD stimulus

Conclusion

This work demonstrates the development of a perfusion system for *ex vivo* brain slice culture fabricated by widely accessible consumer-grade 3D printing, which enables well-controlled delivery of chemical stimuli and straightforward integration with fluorescence microscopy. Two challenges were addressed relating to fabrication by 3D printing. First, the wetting properties of 3D printed plastic were addressed by modifying device geometry to achieve effective clearance of droplets from the tissue chamber. Second, the reduced thermal conductivity of plastic as compared to conventional glass microfabrication substrates was addressed by integrating circulating heated water. Thermal characterization achieved appropriate temperature and temperature stability for mammalian tissue culture.

The perfusion system was demonstrated to maintain Ca^{2+} responsive brain tissue for at least 12 hours of perfusion via KCl-stimulated depolarization and fluorescence imaging of Ca^{2+} responses. Two distinct brain regions, the SCN and EC, were studied in these experiments. Observing the trend of sequential droplets revealed time-resolved dynamics of these changes, demonstrating the suitability of the system for characterizing dynamic processes on minute time scales. Tissue health after 12 hours was verified using PI histological analysis. Finally, system utility was demonstrated by observing drug-induced activation in SCN tissue. Specifically, we observed similar activation profiles for SCN stimulated by AEA and CBD, warranting further study towards specific mechanisms of CBD-induced activation in the SCN.

This work was motivated to advance our previous proof-of-principle bubble perfusion technology, with an emphasis on enabling wider access to the technology for researchers who may not have access or expertise in precision microfabrication. The 3D printed fabrication strategy enables broad access and adoption of this technology and facilitates further

customization and scalability to meet specific research goals. This system represents a platform technology with value for applications in neuroscience, toxicology, pharmacology, and other areas that may benefit from organ-on-chip modeling or *ex vivo* tissue culture.

Chapter 4: Acute response of *ex-vivo* brain tissue after initial Aβ and Tau exposure

Abstract

Microfluidic devices are useful tools for investigating cellular physiology but adapting them to investigate brain tissue slices is a challenge given the high metabolic demands of neuronal tissue. Nevertheless, addressing this challenge will significantly enhance our ability to investigate neuronal function outside of the animal under conditions where local brain structure and cell networking remain intact. A microfluidic device that allows multiple time-stamped assessments of neuronal responses in acute brain slices would be especially useful to investigate complex issues such as the neurochemical changes associated with neurodegenerative diseases. We have developed a novel microfluidic device to maintain healthy *ex vivo* brain tissue slices for up to 12 hours while assessing responsiveness through real-time Ca^{2+} imaging, quantifying time-stamped chemical releasates, and monitoring overall healthy with end-of-experiment histological assessments, as demonstrated in the previous chapter. In these experiments we were interested in utilizing our microfluidic system to study Alzheimer's disease, a progressive and irreversible brain disorder that is currently the leading cause of dementia. The accumulation of amyloid-beta (Aβ) and tau peptides is thought to create a toxic environment that leads to the hallmark memory loss associated with Alzheimer's disease, but the initial effects of these peptides on brain functioning are not known. In Chapter 2, data collected showed brain tissue slices exposed to Aβ and tau exhibited signs of acute toxicity after 12 hours, with Aβ or Aβ + tau being slightly more toxic than tau, depending on brain region. Those experiments were conducted using Hatten-style dishes to maintain the slices. Although useful, that setup did not allow for real-time assessment of physiological changes in response to the peptides. To address these shortcomings, here we maintained brain slices containing the entorhinal cortex or the suprachiasmatic nucleus in our microfluidic device and exposed them to different combinations of Aβ and tau. Acute changes in

intracellular calcium in response to peptide exposure were assessed using the calcium indicator, Calbryte 520 AM. Time-stamped perfusion fluid samples containing analytes released from the slices were collected for off-line analyses. Changes in tissue health were assessed through histological analysis of propidium iodide uptake and release of lactate dehydrogenase. The results of these experiments demonstrate the usefulness of our novel microfluidic device and provide critical new insights regarding whether Aβ and/or tau accumulation may be an early event in Alzheimer's disease progression.

Introduction

Alzheimer's disease (AD) is the most common cause of dementia, affecting millions of Americans over the age of 60 years.[137] This number is expected to grow exponentially in the absence of intervention tools. Although researchers have been studying AD for decades, not much is known about the initial onset of the disease. The accumulation of hallmark proteins amyloid-beta (Aβ) and tau are linked to the disease because of their occurrence in the postmortem brains of AD patients; while there have been many hypotheses regarding their association with AD, there is no clear link that marks these peptides as the actual cause of the disease. In fact, by the time one begins to show clinical symptoms of AD such as memory loss and disorientation, Aβ and tau peptides have already been accumulating for years prior.[138] Contrarily, there are patients who exhibit postmortem peptide accumulation but never exhibited cognitive deficits or signs of dementia.[139] Thus, there is a critical need to understand what is happening in the brain during the initial accumulation of these peptides, before the onset of disease.

Current approaches for AD management focus on helping patients relieve or delay the symptoms of cognitive dysfunction by way of plaque removal, but this is a temporary solution as

AD is an irreversible neurodegenerative disease. Plaque removal does not restore cognitive function loss due to neuronal damage, but only slows/delays progression.[140] Efforts to not only recognize early effects of peptide accumulation but also treat and prevent early damage could go a long way in AD treatment.

Calcium dysregulation is thought to be a major player in neurodegenerative diseases like AD.[141,142] The calcium ion (Ca^{2+}) is an important second messenger in the function and structure of nerve cell circuits in the brain such as synaptic and cognitive function, exocytosis, and neuronal growth.[143,144] The Ca^{2+} influx observed in cell culture as a response to acute peptide exposure supports the idea that dysregulated $Ca^{2+}$is due to peptide accumulation, which eventually leads to neuronal death and cognitive symptoms like memory loss. The endoplasmic reticulum (ER) actively removes Ca^{2+} from the cytoplasm and can release stored Ca^{2+} into cytosolic space through ER membrane calcium channel ryanodine receptors (RyR). Additionally, the RyR can be activated by Ca^{2+} itself, leading to amplified Ca^{2+} influx via calcium-induced calcium releasee (CICR).[145,146] Excessive Ca^{2+} release from the ER via activation of RyR is associated with amyloid and tau pathology and contributes to memory and learning loss in AD. Also, intracellular Aβ oligomers have been found to stimulate Ca^{2+} release from the ER.[147]

Dantrolene is a muscle relaxant used to treat malignant hypothermia.[148] This compound is a known antagonist for RyRs and it blocks the release of Ca^{2+} ions from calcium stores within the ER. Behavioral studies exploring dantrolene's potential as a therapeutic for AD have shown attenuated memory deficits in aged mice.[149,150] Studies suggest that disruption of intracellular Ca^{2+} homeostasis, especially the abnormal and excessive Ca^{2+} release from the ER via the RyR, may play an important role in driving the dynamic of neuropathology of AD and the associated

memory loss, cognitive dysfunction.[142,151,152] Nevertheless, a direct association between dantrolene's acute effects on Ca^{2+} release and brain tissue health has not been shown.

In this study we aimed to investigate the effects of initial acute peptide exposure before the onset of disease, focusing specifically on changes in intracellular calcium. Consistent with our previous research (Chapter 2), we used the peptides $A\beta_{42}$ and Tau_{PHF43} for these experiments. We also aimed to assess changes in tissue health during the course of the experiments in addition to assessing tissue health at the end of the experiments. Lastly, we aimed to investigate the mechanisms of intracellular calcium changes due to peptide exposure and whether they are linked to changes in tissue health in an effort to understand possible targets in reducing or preventing calcium dysregulation.

Materials and methods

Thioflavin T Assay

To investigate whether the peptide monomers used in the described experiment aggregate over our experimental timeframe, a Thioflavin T (ThT) assay was done.[153,154] A 1mM stock solution of ThT was prepared in deionized water. Stock solutions of human $A\beta_{42}$ (Aβ) and Tau_{PHF43} (tau) were made. To a 96-well, EBSS and EBSS supplemented with Aβ, tau, or Aβ:tau was added to five wells each with ThT for each condition so that the final concentration of the peptides was 40μM and the final concentration of the ThT was 25μM with a final volume of 100 μL in each well. Fluorescence measurements were taken using a plate reader at recommended excitation and emission wavelengths at the 1-, 4-, 8-, and 12-hour timepoints. Between measurements the plate was protected from light while shaking at room temperature. All fluorescence values were normalized to ThT in EBSS

Brain Slice Preparation

Coronal brain slices of approximately 500 μm thickness containing the suprachiasmatic nucleus (SCN) and surrounding anterior hypothalamus, or the entorhinal cortex (EC) were collected from adult male C57BL/6 mice. All animals were housed in 12 h light:12 h dark conditions with food and water provided ad libitum. Tissue slices were initially placed in an interface brain slice chamber with Earle's Balanced Salt Solution (EBSS, pH:7.4) and aerated with 95%O_2/5%CO_2 for 30 minutes.

Prior to transferring to the microfluidic device, tissue slices were incubated in EBSS supplemented with 50 μM Calbryte 520 AM (AAT Bioquest, Pleasanton, CA) and 1% pluronic acid while protected from light for 60 minutes. Tissues were then mounted to a Gelbond coverslip using a hydrogel glue comprised of 10 wt% dextran dialdehyde (DDA) in phosphate-buffered saline (PBS) and 5 wt% of chitosan hydrochloride (ChitHCl) in ultrapure water. The cover slip was sealed to the microfluidic device to load the tissue into the tissue chamber. The tissue chamber easily housed EC slices, while SCN slices were trimmed closer to the SCN excluding some of the surrounding AH so they could better fit in the chamber. In the chamber, tissues were perfused with media droplets of EBSS (~20μL) and gas bubbles of carbogen gas (95%O_2/5%CO_2). Between stimulus presentations media droplets were paused in the chamber for 8 minutes followed by gas bubbles that were paused in the chamber for 1 minute. During stimulations, droplet pause times were decreased to 1 minute and gas bubbles pauses were kept at 1 minute.

Ca^{2+} Imaging of Peptide Response

In order to investigate the initial response to Aβ and tau exposure, tissue slices were stimulated with 60 mM KCl at 1, 6, and 12 hours of perfusion time, or with 40 μM Aβ, tau, or

Aβ:tau at 1, 4, 8, and 12 hours of perfusion time. Calbryte 520 AM, an intracellular calcium indicator, was used to visualize changes in calcium in response to KCl or peptide exposure. Each stimulus sequence included fluorescent imaging for 4 pre-stimulus (EBSS alone), 1 stimulus (EBSS supplemented with KCl or peptides), and 4 post-stimulus (EBSS alone) droplets following the procedures we developed previously (Chapter 3). During the stimulus sequence, a series of time-lapsed images were taken of the tissue throughout the droplet pauses, one every 5 seconds. Tissue slices were centered in the image capturing window using visual landmarks, specifically the optic chiasm and third ventricle for the SCN, to ensure the brain region of interest was being imaged. Fluorescence image sequences were collected using an upright fluorescence microscope (BH-2, Olympus, Tokyo, Japan) outfitted with a 488 nm laser excitation source (GH04850B2G, Sharp Corp., Osaka, Japan) and sCMOS camera (FMA050, AmScope, Irvine, CA). To investigate the effect of dantrolene on peptide-induced intracellular calcium changes, the above-described experiments (testing KCl, Aβ, and tau but not Aβ:tau) were repeated using EBSS supplemented with 20 μM dantrolene for all non-stimulus droplets. Each condition in each brain region was replicated three times using different brain tissue samples, except KCl stimulation with dantrolene in the EC and SCN region, which was replicated twice.

Propidium Iodide Treatment and Imaging

In order to investigate the extent of cell death and damage at the end of each experiment, propidium iodide (PI) was used as a marker of cell health. PI is only able to enter dead and damaged cells, where it binds nuclear DNA and is fluorescent upon excitation at ~535 nm.[84–87] After 12 hours of microfluidic perfusion/stimulation, slices were transferred back to an interface brain slice chamber and perfused for 2 hours with EBSS containing 4.6 μg/mL PI. Following PI exposure, slices were fixed in 4% PFA for 10 minutes then transferred to 30%

sucrose overnight at 4°C. Slices were embedded in optimal cutting temperature (OCT) compound and stored at -80°C. 25 μm tissue sections were cut using a cryostat and mounted to gelatin subbed slides and stored at -80°C. Slides were defrosted at room temperature and washed three times for five minutes each with PBS. Coverslip media containing 4',6-diamidino-2-phenylindole (DAPI) was added to the surface of slides before they were cover slipped and sealed with nail polish.

Fluorescence images were acquired via a 20x objective using a Keyence BZ-X microscope and analyzed using ImageJ software (NIH). One image was analyzed for each tissue slice, and a region of interest (ROI) was drawn to contain either the entire SCN or a portion of the EC within that section. The images were split into blue and red channels to isolate DAPI-stained cells and PI-stained cells, respectively. Within each ROI, the total number of cells were counted using the DAPI image, and the PI was assessed in the same ROI. The ImageJ thresholding feature was used to differentiate between high PI intensity cells corresponding to dead cells, moderate PI intensity indicating damaged cells, and cells with minimal PI staining, considered healthy cells (Appendix B). The percentages of total cells that were healthy, damaged, or dead cells were then calculated.[155–157]

Immunohistochemical Staining and Imaging

Slides containing SCN or EC tissue sections from PI treated brain slices underwent IHC staining with IBA1 or NeuN antibodies to identify microglia and neurons, respectively. The total number of each cell type in the ROIs and the percentage of each specific cell type that was healthy, damaged, or dead when treated with Aβ and/or tau compared to control conditions. For IBA1 and NeuN staining, the sections were washed PBS for 5 minutes a total of four times and blocked with a blocking buffer containing 3% Bovine Serum Albumin and 0.3% Triton X-100

for an hour. The blocking buffer was then replaced with blocking buffer containing IBA1 or NeuN antibody diluted to 1:1000 and incubated overnight at 4°C. The following day, the sections were again washed four times with PBS for 5 minutes and incubated with secondary antibody, Donkey anti-Rabbit 488, diluted to 1:1000 for one hour at room temperature. Following the secondary incubation, the sections were again washed four times with PBS for 10 minutes.

All slides were then cover slipped with VECTASHIELD (Vector Laboratories, CA, USA), sealed using nail polish and stored in 4°C until imaging was conducted. Fluorescence images were acquired via 20x objective using a Keyence BZ-X microscope and analyzed using ImageJ software. One image was analyzed for each tissue slice, and a ROI was drawn to contain either the entire SCN or a portion of the EC within that section. The images were split into blue (DAPI), red (PI), and green (IBA1 or NeuN) channels to isolate DAPI-stained cells, PI-stained cells, and specific cell types respectively. Within each ROI, the total number of cells were counted using the DAPI image, and the PI overlapping with the cell type was assessed in the same ROI. The ImageJ thresholding feature was used to differentiate between high, moderate and low PI intensity cells as above (Appendix B). The percentages of total cells that were healthy, damaged, or dead of each cell type were then calculated by counting the number of cell type specific cells in the green channel that overlapped with PI-stained cells of each intensity in the red channel.

LDH Sample Collection and Analysis

Lactate dehydrogenase (LDH) is an enzyme found in most mammalian cells that is released into the extracellular space when the cell membrane becomes compromised due to cell damage and death, making it a possible marker of cell health.[158] Initially, perfusion droplets were collected directly from the microfluidic outlet tubing into an Eppendorf tube while the time-

lapsed images of the tissue were being taken and droplets remained in the tissue chamber for only 1 minute. These initial experiments showed that 1-minute droplets were not in the chamber long enough for sufficient LDH to diffuse into the media for quantification (data not shown). To address this, droplets were collected immediately preceding the imaging sequence, when media droplets were paused in the tissue chamber for 8 minutes. In order to have enough volume for the LDH assay (~50 μL), 3 to 4 droplets were collected into an Eppendorf tube, which was immediately stored at -20°C. Droplets were collected from three tissue samples in each condition to give three total replicates for each condition. Samples were thawed and loaded onto a 96-well plate. Cytotoxicity was assessed using a CyQUANT LDH Cytotoxicity assay kit (catalog no. C20303, Invitrogen) according to the manufacturer's protocol. Fluorescence measurements were taken using a plate reader at recommended excitation and emission wavelengths.

Statistical Analysis

All the data were plotted using GraphPad Prism. To compare differences in fluorescence intensity of the ThT assay, two-way ANOVAs comparing the averaged fluorescence intensity over the 12-hour period were performed using GraphPad Prism. Each peptide condition was compared to the blank EBSS media and each other. All differences at $p<0.05$ were considered statistically significant.

To compare differences in fluorescence intensity for Ca^{2+} imaging, Friedman tests comparing the means of the last pre-stimulus droplet and all the post-stimulus droplets to the mean of the stimulus droplet were performed using GraphPad Prism for each condition at each time point. Differences were considered statistically significant at $p<0.05$.

To determine the percentage of healthy, damaged, or dead cells in different brain areas under all conditions, the means and SEMs were plotted and analyzed using GraphPad Prism. To

compare differences in the percentage of cells that were healthy, damaged or dead in each region, separate two-way ANOVAs with brain region and experimental conditions factors were performed for each cell health status category. Similar analyses were performed to determine the percentage of healthy, damaged, and dead cells of each specific cell type. All differences at $p<0.05$ were considered statistically significant.

To determine differences in overall tissue health with and without the use of EBSS supplemented with dantrolene, first the mean and SEM of healthy, damaged, and dead cells from KCl, Aβ, and tau stimulated tissue in the presence of dantrolene in each condition for each brain region was analyzed as above. Separately, a one-way ANOVA comparing each mean from the control and dantrolene conditions was conducted. All differences of $p<0.05$ were considered statistically significant.

For all LDH data, a one-way ANOVA was used to compare the mean of each condition over the 12-hour period to each other. Differences were considered statistically significant at $p<0.05$.

Results and Discussion

ThT assay of Aβ, tau, and Aβ:tau aggregation

ThT is a fluorescent dye that can be used to visualize and quantify protein aggregation and is commonly using for amyloid fibrils or tau aggregates.[153,154] Upon binding beta-sheets, there is an enhanced fluorescence, making it a useful tool to study peptide aggregation. In **Figure 4.1**, the fluorescence of each peptide over a 12-hour period is shown. Two-way ANOVAs indicated that there were statistically significant differences in the overall fluorescence intensity of Aβ ($p<0.0001$) and Aβ:tau ($p<0.0001$) when compared to tau and blank EBSS media. There was no statistically significant difference in the overall fluorescence intensity of tau ($p>0.9999$)

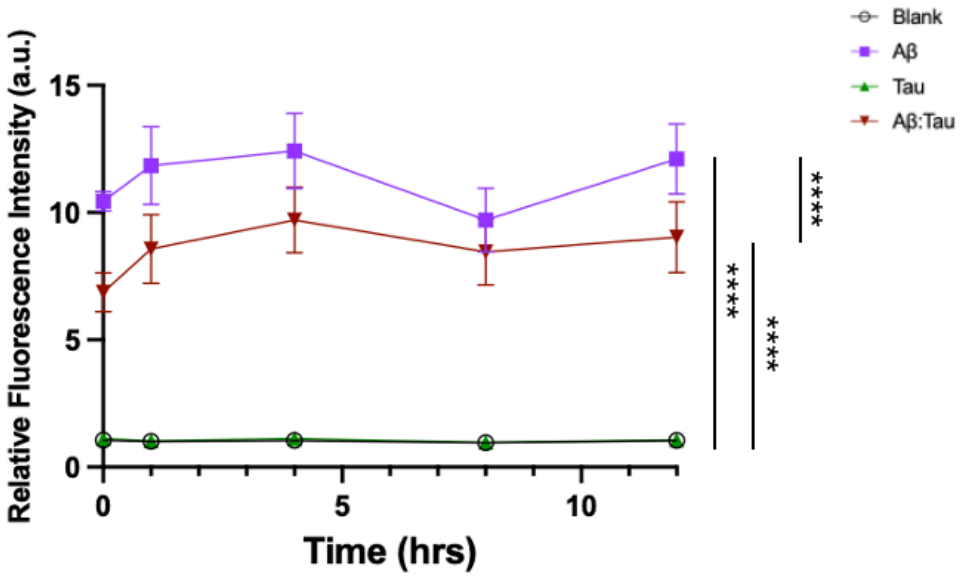


Figure 4.1 Peptide aggregation Fluorescence intensity of ThT with 40 μM Aβ, tau, and Aβ:tau over 12 hours ****p<0.0001, ns = p > 0.05. N=5

compared to blank EBSS media, suggesting the absence of beta-sheet aggregation. The specific form of tau used, $Tau_{PHF43,}$ is an fragment of one of the human tau isoforms that contains one of two six-residue sequences that lend to the propensity to form paired helical filaments.[81,82] The absence of fluorescent signal for tau suggest no further aggregation into beta-sheets and the reduced fluorescent signal of Aβ:tau suggest the tau paired helical filaments partially disrupts Aβ aggregation. Altogether this data indicates that Aβ and Aβ:tau aggregated in EBSS media within the first hour but not tau and Aβ underwent more aggregation than Aβ:tau.

Stimulus-induced changes in intracellular Ca^{2+}

From the obtained time-lapsed images, fluorescence *vs.* time profiles were extracted using ImageJ to define a region of interest corresponding to the EC or the SCN. Mean intensity values pertaining to only image data collected during the interval when a media droplet filled the tissue chamber were used while images obtained while gas bubbles were in the chamber were disregarded. Non-linear background drift resulting from photobleaching, and dye leakage was fit to a single-phase exponential decay, and the fluorescence *vs.* time profile of the full droplet sequence was divided by the exponential decay fit to give the signal-to-background ratio profile for each droplet. The mean of all pre-stimulus droplets was calculated to give the intra-droplet baseline profile that then was subtracted from the signal-to-background ratio profile of the last pre-stimulus, stimulus, and all post-stimulus droplets to get the baseline-subtracted signal-to-background ratio profile of each droplet (Appendix B). The calculated relative fluorescence intensities for before, during, and after brain tissue slices were stimulated at 1-, 6-, and 12 hours of incubation for KCl or 1-, 4-, 8- and 12 hours of incubation for Aβ, tau, and Aβ:tau are shown in Appendix A. More condensed graphs of these data are shown in **Figure 4.2**, where box plots

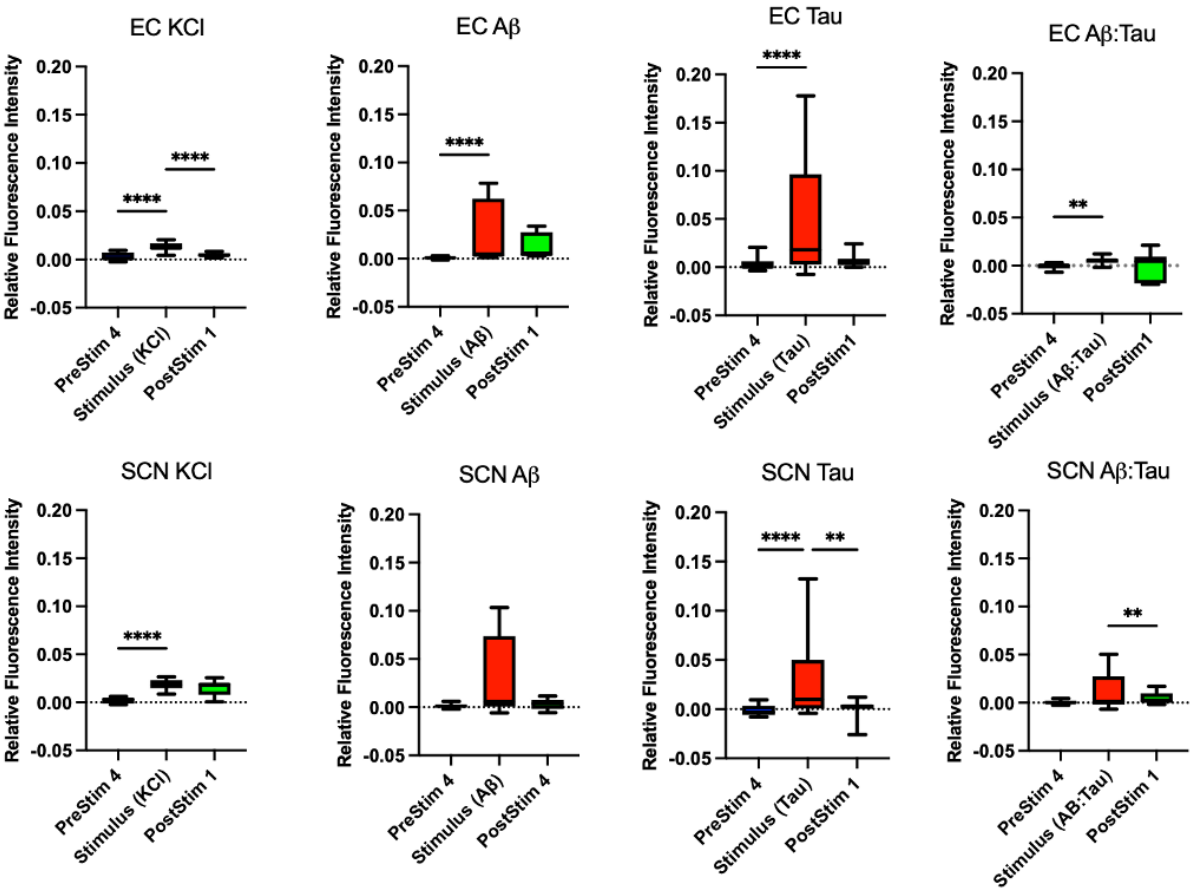


Figure 4.2 Comparison of peptide-induced Ca^{2+} response in EC and SCN Summary of Ca^{2+} response in EC (top row) and SCN (bottom row) tissue induced by delivery of 60 mM KCl, 40μM Aβ, 40μM tau, and 40μM Aβ:tau during 12 hours of perfusion. Each dataset pools observations from across the 12 hours for three replicates. **$p < 0.01$, ****$p < 0.0001$, ns = $p > 0.05$. N=3 for each condition.

represent the combined range of averaged values across all the stimulus times for each experimental condition.

Friedman tests indicate that there were statistically significant fluorescence increases between the last pre-stimulus droplet (PreStim 4) and the stimulus droplet in the KCl ($p<0.0001$), Aβ ($p<0.0001$), tau ($p<0.0001$), and Aβ:tau ($p=0.0018$) conditions as well as the stimulus droplet and first post stimulus droplet (PostStim 1) in the KCl ($p<0.0001$) condition in the EC. There was not a statistically significant difference between the stimulus and PostStim 1 in the Aβ ($p>0.9999$), tau ($p>0.9999$), and Aβ:tau ($p>0.9999$) conditions. In the SCN, there were statistically significant fluorescence increases between PreStim 4 and the stimulus droplet in the KCl ($p<0.0001$) and tau ($p<0.0001$) conditions as well as the stimulus droplet and PostStim 1 in the tau ($p=0.0021$) and Aβ:tau ($p=0.0057$) conditions. There was not a statistically significant difference between PreStim4 and the stimulus in the Aβ:tau (0.4819) condition, the stimulus and PostStim 1 in the KCl ($p=0.3030$) condition, and the PreStim 4 ($p=0.0991$) or PostStim 1 ($p>0.9999$) and stimulus droplet in the Aβ condition (**Figure 4.2**). All together this shows that in the EC, Aβ and tau, independently and combined, induced increases in intracellular Ca^{2+} similar to KCl, while in the SCN this effect was not as strong as seen in the EC. These changes were observed throughout the 12-hour perfusion of the tissue and demonstrate a relatively fast response (within a minute) to peptide exposure that is generally similar to that induced by KCl.

PI imaging analysis

One-way ANOVAs indicated that there was not a statistically significant difference in the number of healthy ($p=0.9307$), damaged ($p=0.9989$), or dead ($p=0.9997$) cells in EC slices stimulated with Aβ when compared to slices stimulated with KCl. There was also not a statistically significant difference in the number of healthy ($p>0.9999$), damaged ($p=0.9999$), or

dead (p=0.9992) cells in slices stimulated with tau when compared to slices stimulated with KCl. There was also not a statistically significant difference in the number of healthy (p=0.7758), damaged (p=0.9948), or dead (p=0.9976) cells in slices stimulated with Aβ:tau when compared to slices stimulated with KCl (**Figure 4.3**). In the SCN, one-way ANOVAs indicated that there was not a statistically significant difference in the number of healthy (p=0.3696), damaged (p=0.9963), or dead (p=0.8548) cells in slices stimulated with Aβ when compared to slices stimulated with KCl. There was also not a statistically significant difference in the number of healthy (p=0.9967), damaged (p=0.9886), or dead (p>0.9999) cells in slices stimulated with tau when compared to slices stimulated with KCl. There was also not a statistically significant difference in the number of healthy (p=0.5574), damaged (p=0.7862), or dead (p>0.9999) cells in slices stimulated with tau when compared to slices stimulated with KCl (**Figure 4.3**). Although there were no statistically significant differences across the experimental conditions, when the number of healthy cells in each condition for each brain region are compared (**Figure 4.4**), one-way ANOVAs indicated there were statistically more healthy cells in the SCN Aβ:tau condition at the end of the 12 hours than the EC (p=0.0151). There were no statistically significant differences in the number of healthy cells in the SCN versus the EC in the KCl (p=0.8603), Aβ(0.9958) and tau (p=0.4946) conditions.

PI imaging analysis of neurons and microglia

The number of neurons co-stained with NeuN and PI were quantified. One-way ANOVAs indicated that there were no statistically significant differences in the number of healthy (p=0.9967), damaged (p=0.9883), or dead (p>0.9999) neurons in EC slices stimulated with Aβ when compared to slices stimulated with KCl. There were no statistically significant differences in the number of healthy (p=0.9977), damaged (p=0.9654), or dead (p>0.9999)

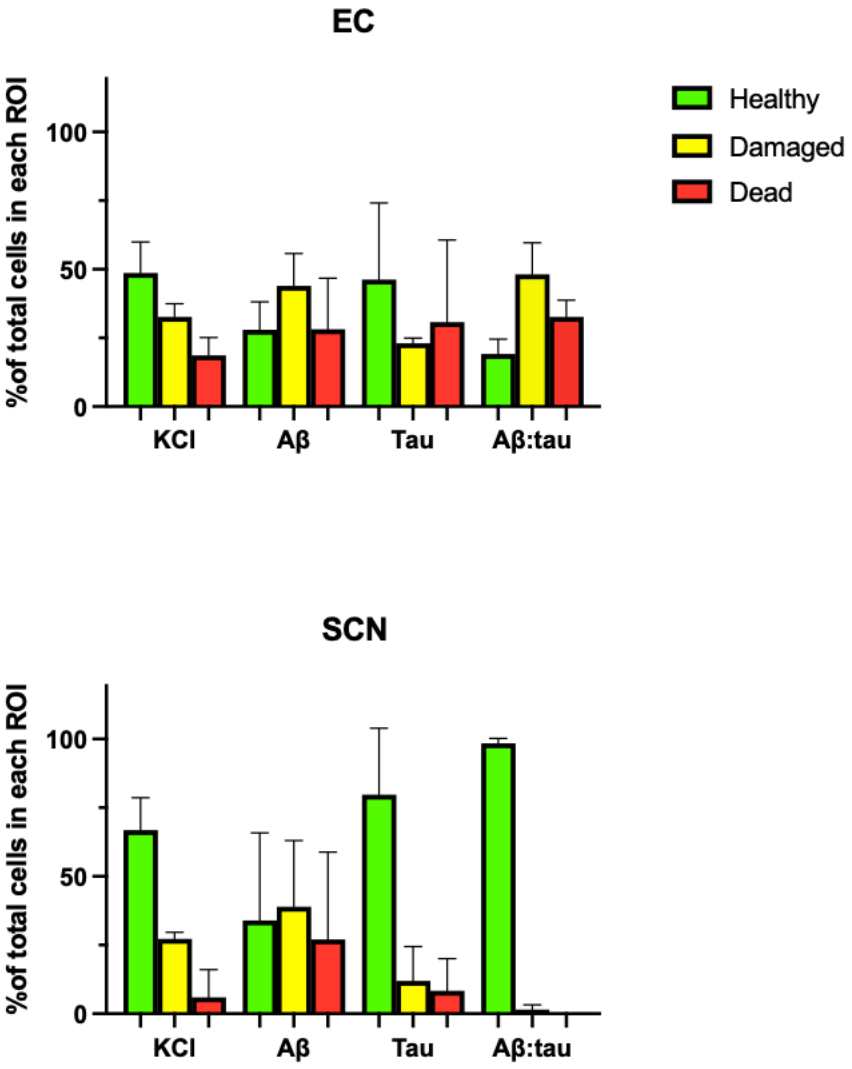


Figure 4.3 Comparison of cell death in EC and SCN Percentage of healthy, damaged, and dead cells in the EC and SCN after 12 hours, periodically stimulated with 40μM Aβ, tau, Aβ:tau or 60 mM KCl. N=3

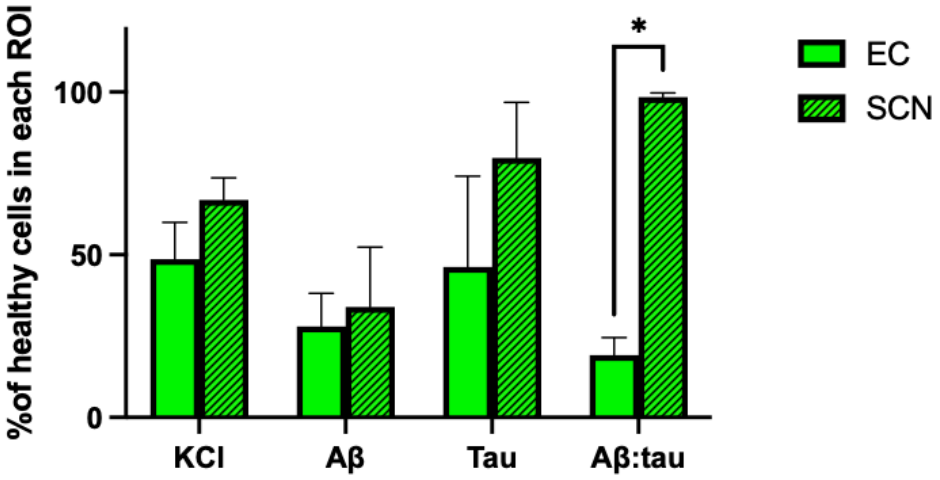


Figure 4.4 Comparison of heathy cells in EC and SCN. Percentage of healthy cells in the EC and SCN after 12 hours, periodically stimulated with 60 mM KCl, 40μM Aβ, tau, or Aβ:tau in EBSS. *p<0.05, **p<0.01, ns = p>0.05. N=3

neurons in EC slices stimulated with tau when compared to slices stimulated with KCl. There were no statistically significant differences in the number of healthy ($p=0.7529$), damaged ($p=0.5590$), or dead ($p>0.9999$) neurons in EC slices stimulated with Aβ:tau when compared to slices stimulated with KCl (**Figure 4.5**).

In the SCN, one-way ANOVAs indicated that there were no statistically significant differences in the number of healthy ($p=0.9916$), damaged ($p=0.9996$), or dead ($p>0.9999$) neurons in slices stimulated with Aβ when compared to slices stimulated with KCl. There were no statistically significant differences in the number of healthy ($p=0.5690$), damaged ($p=0.9611$), or dead ($p=0.9968$) neurons in slices stimulated with tau when compared to slices stimulated with KCl. There were no statistically significant differences in the number of healthy ($p>0.9999$), damaged ($p>0.9999$), or dead ($p>0.9999$) neurons in slices stimulated with Aβ:tau when compared to slices stimulated with KCl (**Figure 4.5**). The percentage of total cells in each region that were NeuN positive for each stimulus condition was also determined (Appendix A).
The number of microglial cells co-stained with IBA1 and PI were quantified. One-way ANOVAs indicated that there were no statistically significant differences in the number of healthy ($p>0.9999$), damaged ($p=0.9998$), or dead ($p>0.9999$) microglial cells in EC slices stimulated with Aβ when compared to slices stimulated with KCl. There were also no statistically significant differences in the number of healthy ($p=0.9496$), damaged ($p=0.9352$), or dead ($p>0.9999$) microglial cells in EC slices stimulated with tau when compared to slices stimulated with KCl. There were statistically significant differences in the number of healthy ($p=0.0101$) and dead ($p=0.0009$) but not damaged ($p=0.9463$) microglial cells in EC slices stimulated with Aβ:tau when compared to slices stimulated with KCl (**Figure 4.6**).

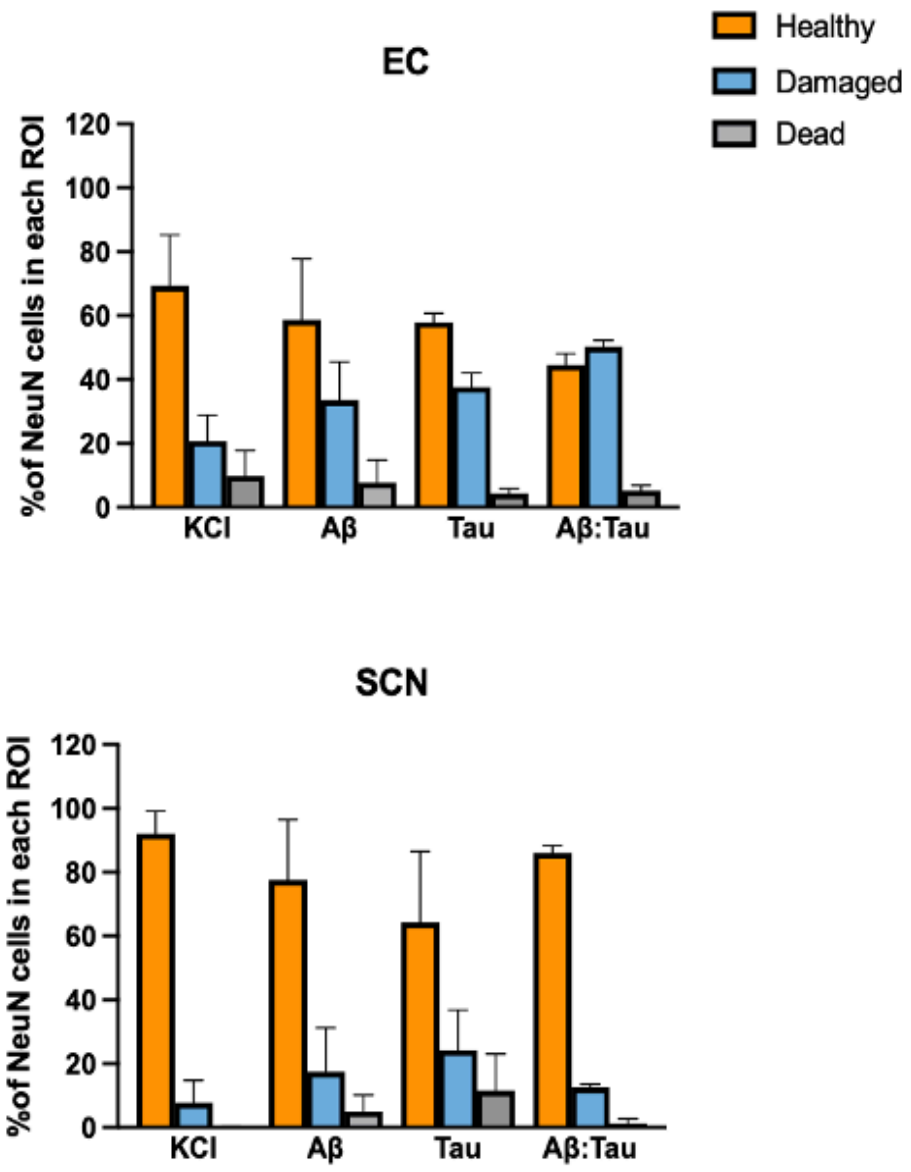


Figure 4.5 Comparison of neuron specific cell death in EC and SCN Percentage of healthy, damaged, and dead neurons in the EC and SCN after 12 hours, periodically stimulated with 40μM Aβ, tau, Aβ:tau or 60 mM KCl. N=3

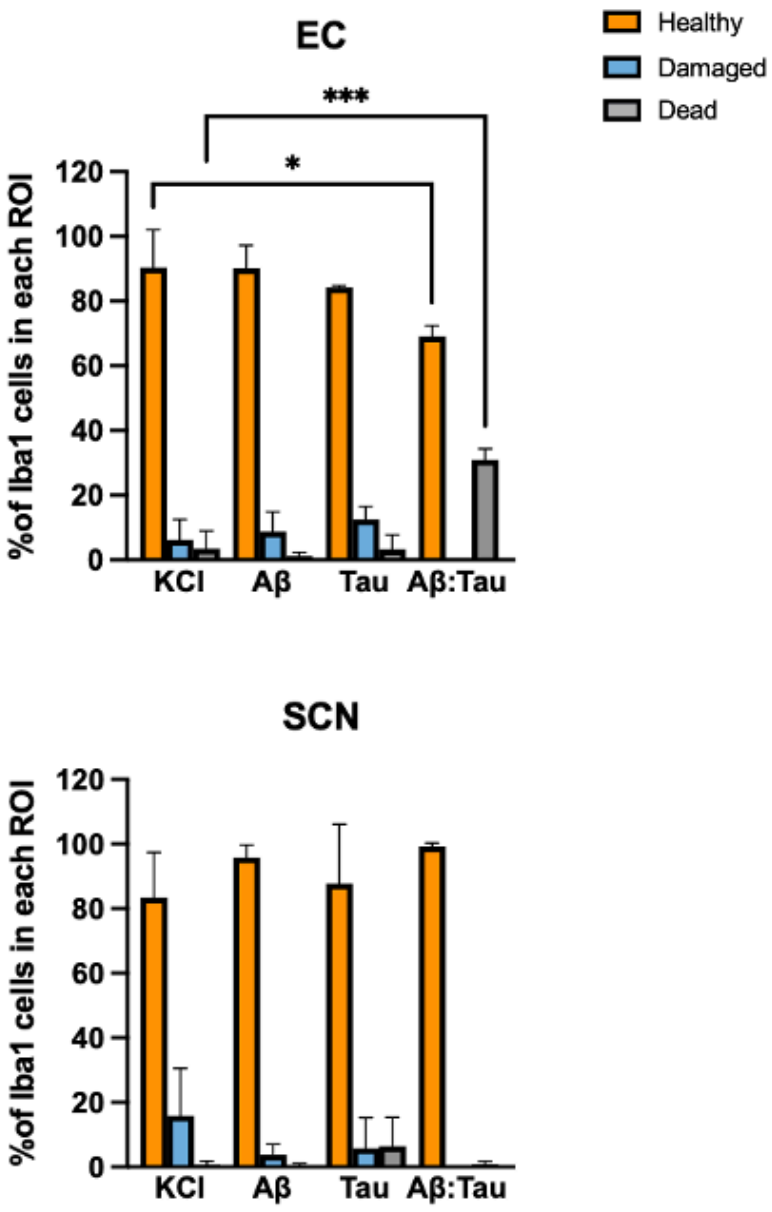


Figure 4.6 Comparison of microglia specific cell death in EC and SCN Percentage of healthy, damaged, and dead microglia in the EC and SCN after 12 hours, periodically stimulated with 40μM Aβ, tau, Aβ:tau or 60 mM KCl. N=3

In the SCN, one-way ANOVAs indicated that there was not a statistically significant difference in the number of healthy ($p=0.6989$), damaged ($p=0.7262$), or dead ($p>0.9999$) microglial cells in slices stimulated with Aβ when compared to slices stimulated with KCl. There was not a statistically significant difference in the number of healthy ($p=0.9996$), damaged ($p=0.8767$), or dead ($p=0.9965$) microglial cells in slices stimulated with tau when compared to slices stimulated with KCl. There was not a statistically significant difference in the number of healthy ($p=0.5386$), damaged ($p=0.5353$), or dead ($p>0.9999$) microglial cells in slices stimulated with Aβ:tau when compared to slices stimulated with KCl (**Figure 4.6**). The percentage of total microglial cells in each region that were IBA1 positive for each stimulus condition was also determined (Appendix A).

LDH analysis

One-way ANOVAs comparing fluorescence levels of the samples across the 12-hour incubation period determined there were statistically significant differences. Pairwise comparisons indicated that significantly more LDH was released by EC tissue slices treated with tau ($p<0.0001$) and Aβ:tau ($p=0.0001$) compared to slices treated with KCl as well as tau ($p<0.0001$) and Aβ:tau (0.0002) compared to slices treated with Aβ. In the SCN, slices treated with Aβ ($p<0.0001$), tau ($p<0.0001$), and Aβ:tau (<0.0001) also released significantly more LDH compared to slices treated with KCl (**Figure 4.7**).

Ca^{2+} imaging in the presence of dantrolene

To investigate whether the increase in fluorescence intensity signaling indicating an increase in intracellular Ca^{2+} involved release from intracellular stores, in the next set of experiments EBSS was supplemented with 20μM dantrolene made from a stock solution of 1mM dantrolene prepared in DMSO. In these experiments, only the KCl, Aβ, and tau stimulations

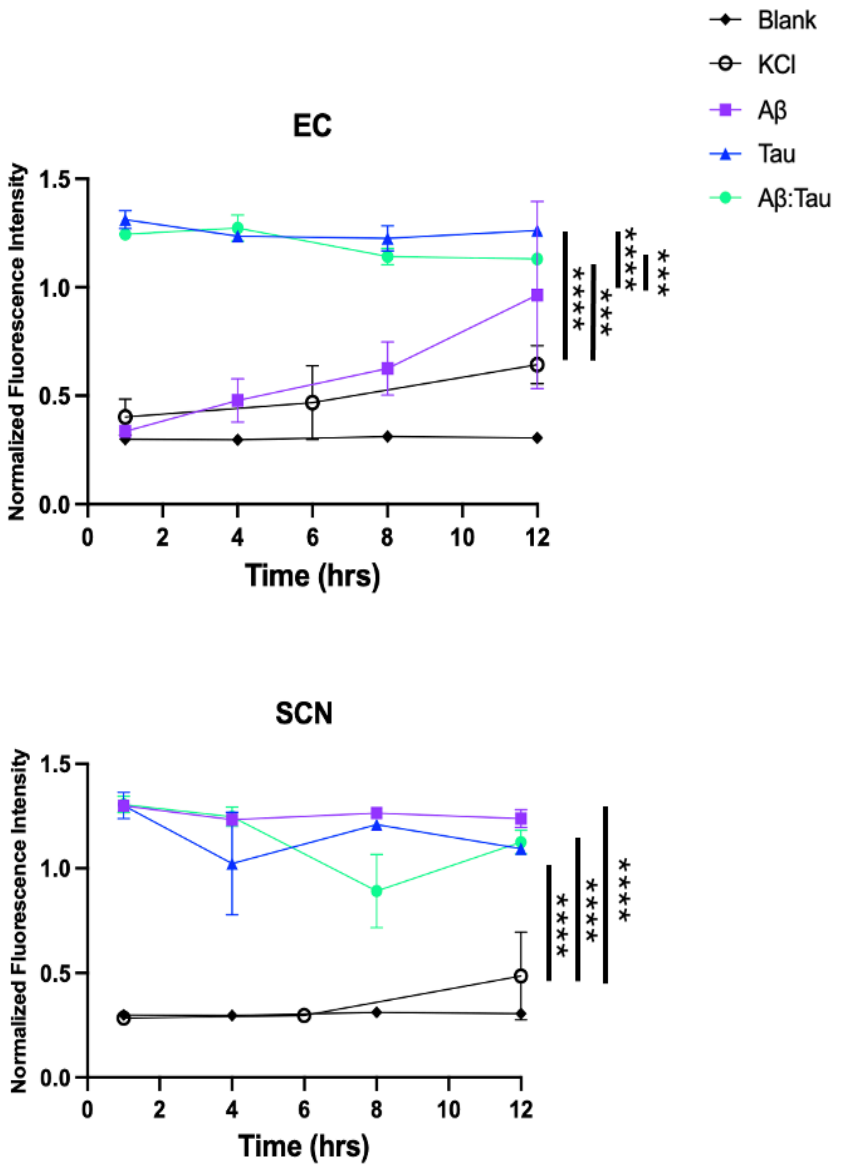


Figure 4.7 Quantified LDH release from the EC and SCN Normalized fluorescence intensity of released LDH over 12 hours from EC and SCN slice periodically stimulated with 60mM KCl, 40μM Aβ, and 40μM tau. **p<0.01 ****p < 0.0001, ns = p > 0.05. N=3

were used but not Aβ:tau. In previous experiments both with and without using microfluidics (Chapter 2), Aβ:tau did not show statistically significant cell death compared to the individual peptides. To meet time constrains, focus was shifted to the effects of Aβ and tau independently.

To test whether DMSO by itself affects the brain tissue slices, control experiments using EBSS supplemented with only DMSO were completed (**Figure 4.8**). Friedman tests indicated a statistically significant difference between the relative fluorescence intensity of PreStim 4 ($p<0.0001$) and PostStim 1 ($p<0.0001$) when compared to the KCl stimulus droplet in EC slices. In the SCN, there was not statistical difference between the PreStim 4 ($p=0.3146$) or PostStim 1 ($p=0.2396$) and the KCl stimulus droplet.

Next, tissue slices containing the EC or the SCN were stimulated with KCl, Aβ or tau using EBSS supplemented with dantrolene. Friedman tests indicated statistically significant differences in the fluorescence intensity of the PreStim 4 ($p<0.0001$) and PostStim 1($p=0.0007$) droplets compared to the KCl stimulus droplet in EC slices. There were also a statistically significant differences between the PreStim 4 ($p<0.0001$) and Aβ stimulus droplets as well as the PostStim 1 ($p<0.0001$) and tau stimulus droplets but not the PostStim 1 ($p=0.1762$) and Aβ stimulus droplets or the PreStim 4 ($p=0.0629$) and tau stimulus droplet (Figure 4.9). In the SCN, Friedman tests indicated statistically significant differences in the fluorescence intensity of the PreStim 4 ($p<0.0001$) and PostStim 1($p<0.0001$) droplets compared to both the Aβ and tau stimulus droplets. There was a statistically significant difference between the PreStim 4 ($p<0.0001$) but not the PostStim 1($p>0.9999$) droplet compared to the KCl stimulus droplet (**Figure 4.9**).

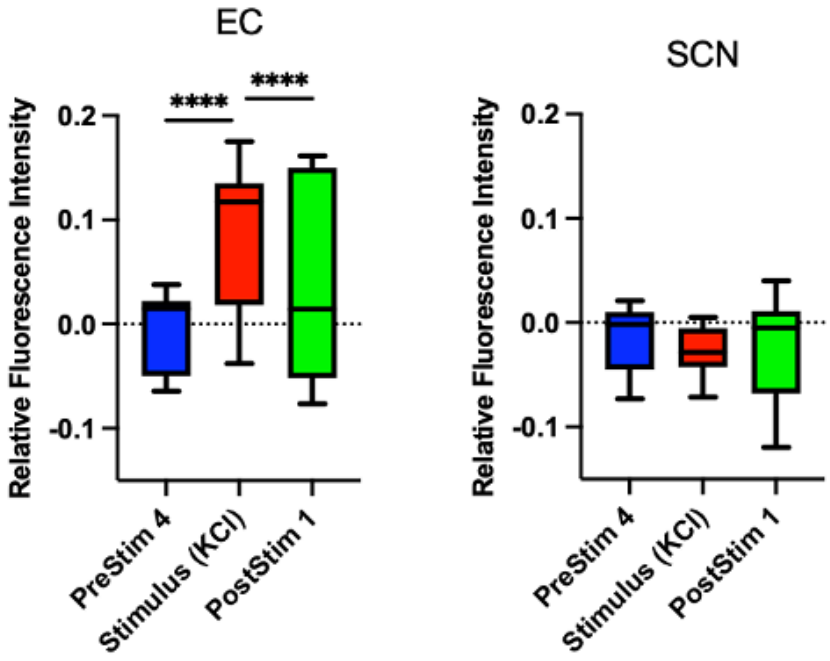


Figure 4.8 Comparison of KCl induced Ca^{2+} response in EC and SCN in the presence of DMSO
Summary of Ca^{2+} response in EC and SCN tissue induced by delivery of 60 mM KCl with DMSO supplemented EBSS Each dataset pools observations from three tissue slices. ****$p < 0.0001$, ns = $p > 0.05$. N=2

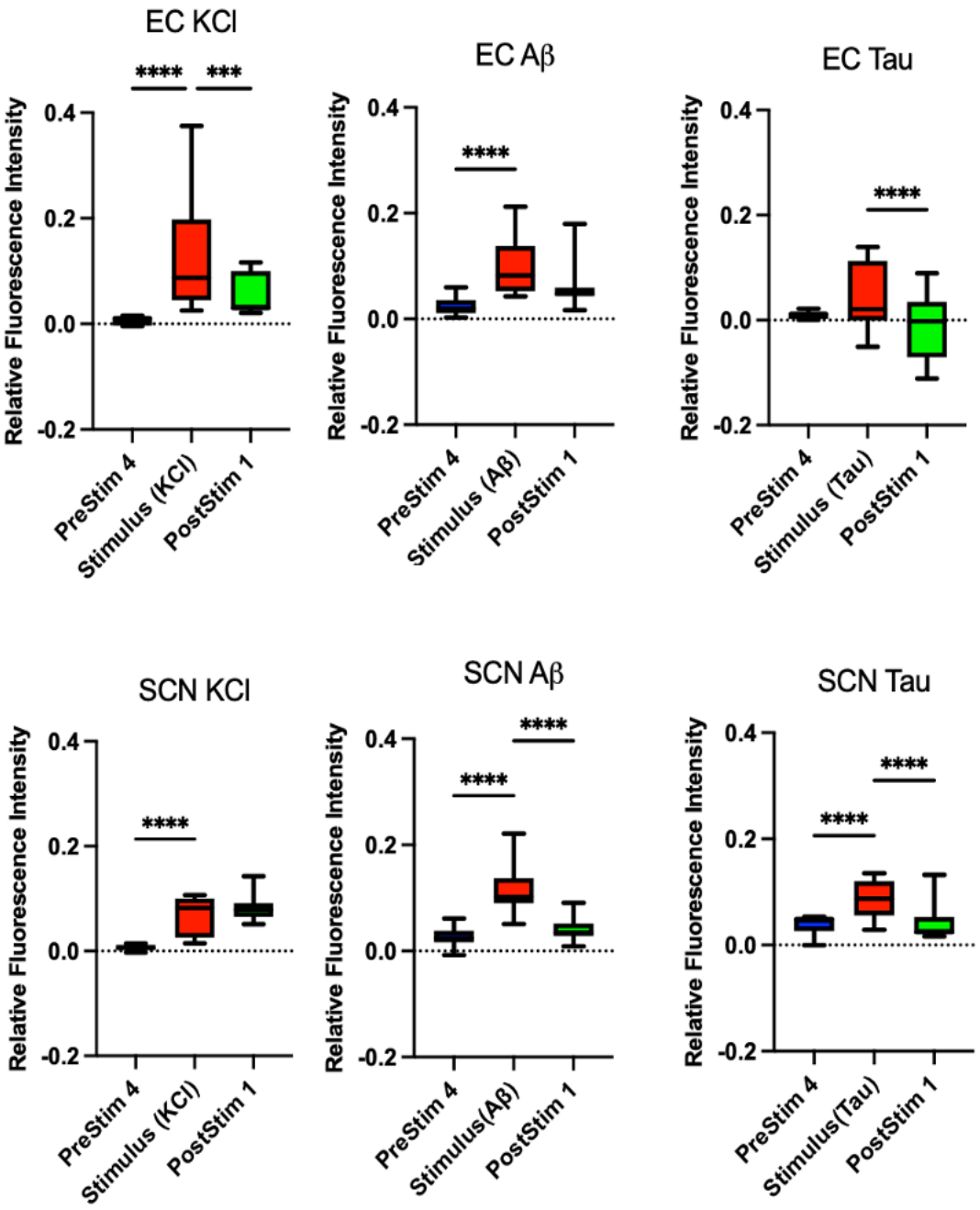


Figure 4.9 Comparison of peptide induced Ca^{2+} response in EC and SCN in the presence of dantrolene. Summary of Ca^{2+} response with 20μM dantrolene in EC (top row) and SCN (bottom row) tissue induced by delivery of 60 mM KCl, 40μM Aβ, and 40μM tau during 12 hours of perfusion. Each dataset pools observations from three tissue slices. ***p < 0.001, ****p < 0.0001, ns = p > 0.05. N=2-3

PI imaging analysis in the presence of dantrolene

One-way ANOVAs indicated that there was not a statistically significant difference in the number of healthy ($p=0.2431$), damaged ($p=0.5099$), or dead ($p>0.9999$) cells in EC slices stimulated with Aβ when compared to slices stimulated with KCl. There also was not a statistically significant difference in the number of healthy ($p=0.0859$), damaged ($p=0.2749$), or dead ($p=0.9993$) cells in EC slices stimulated with tau when compared to slices stimulated with KCl. In the SCN, one-way ANOVAs indicated that there was not a statistically significant difference in the number of healthy ($p=0.2184$), damaged ($p=0.2184$), or dead ($p>0.9999$) cells in slices stimulated with Aβ when compared to slices stimulated with KCl. There was also not a statistically significant difference in the number of healthy($p=0.1108$), damaged ($p=0.1108$), or dead ($p>0.9999$) cells in slices stimulated with tau when compared to slices stimulated with KCl (**Figure 4.10**).

Although there were no statistically significant differences across the three experimental conditions within the dantrolene experiments, when compared to tissues in the same conditions perfused with EBSS not supplemented with dantrolene (**Figure 4.11**), one-way ANOVAs indicated there were statistically more healthy cells in the Aβ condition at the end of the 12 hours in both the EC ($p=0.0153$) and SCN (0.0032) tissues exposed to dantrolene. There were no statistically significant differences in the number of healthy cells in the EC when comparing control to dantrolene for the KCl ($p=0.8604$) and tau ($p=0.0937$) conditions or in the SCN for the KCl ($p=0.4052$) and tau ($p=0.5723$) conditions. Thus, overall, these data indicate improve cell health after peptide exposure in the presence of dantrolene.

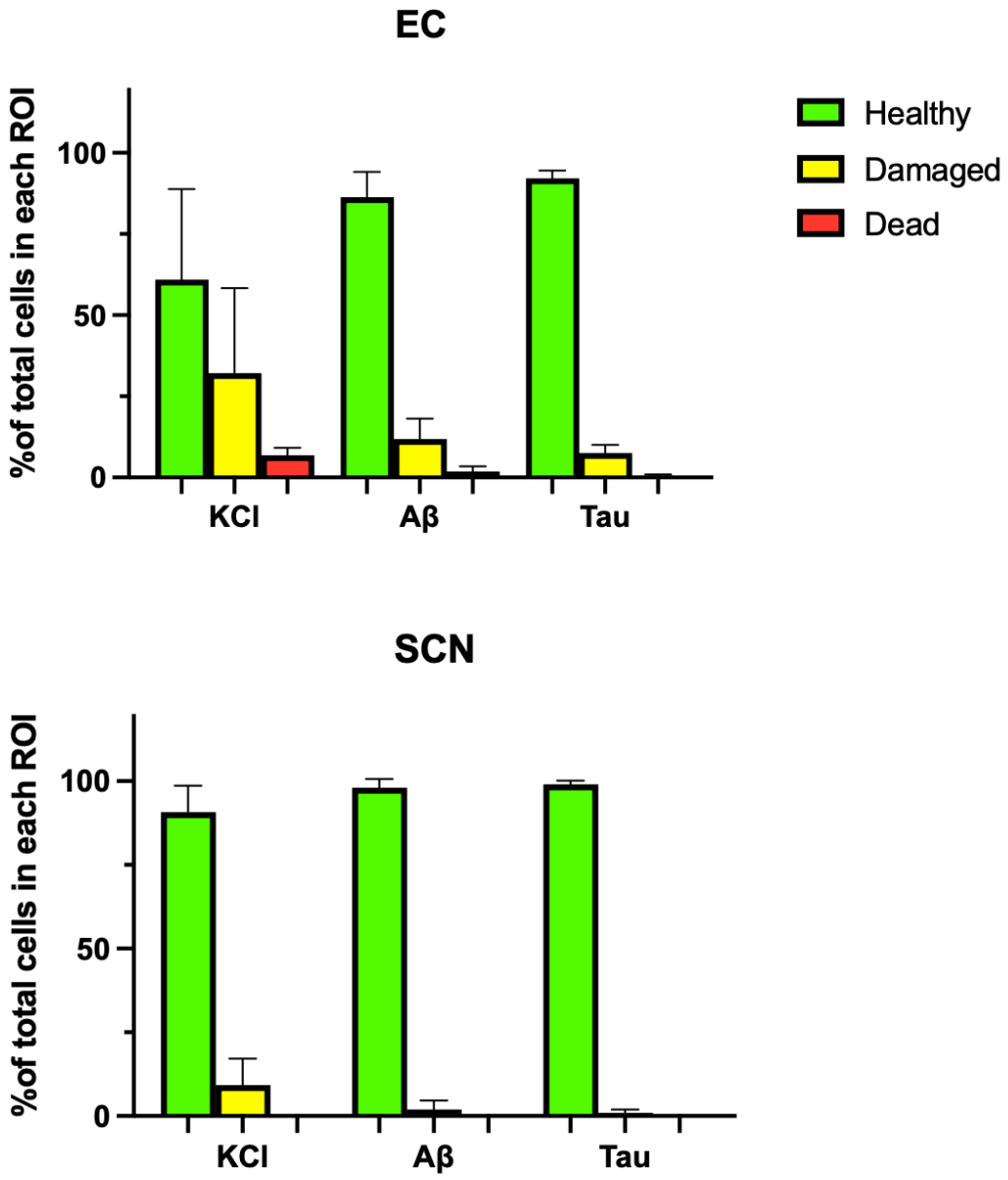


Figure 4.10 Comparison of cell death in EC and SCN in the presence of dantrolene. Percentage of healthy, damaged, and dead cells in the EC and SCN after 12 hours, periodically stimulated with 40μM Aβ, tau, or 60 mM KCl in EBSS supplemented with 20μM dantrolene. N=3

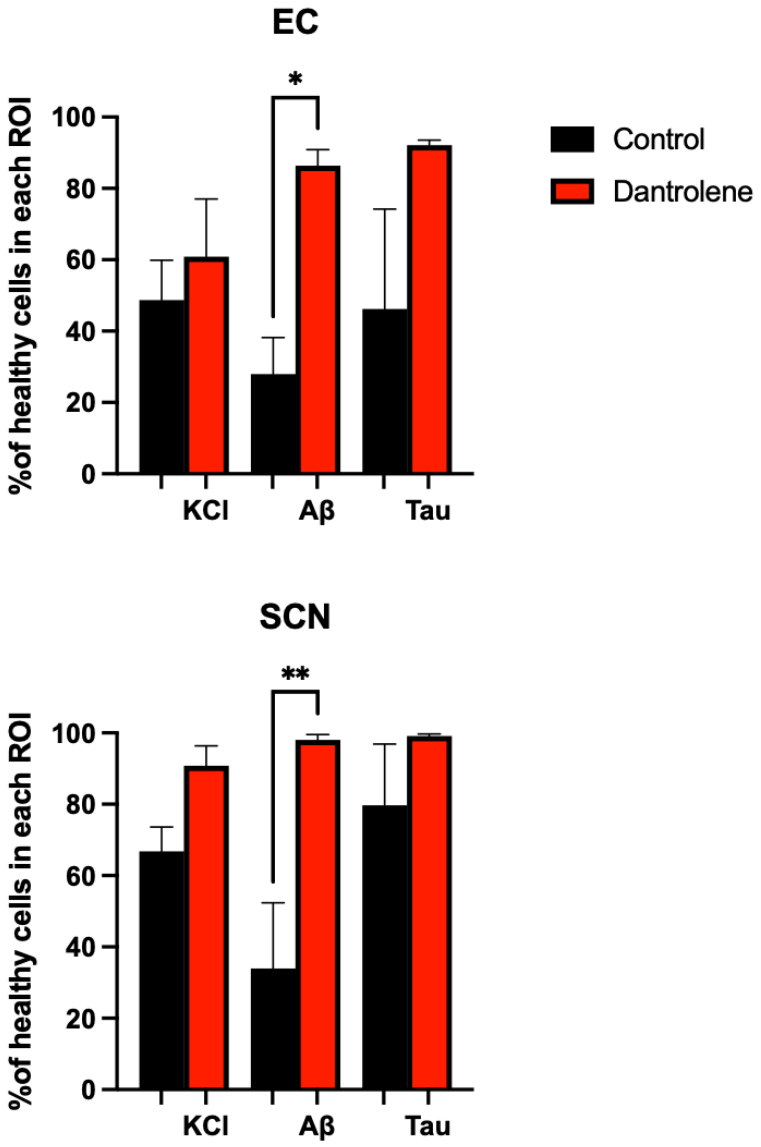


Figure 4.11 Comparison of heathy cells in EC and SCN. Percentage of healthy cells in the EC and SCN after 12 hours, periodically stimulated with 40μM Aβ, tau, or 60 mM KCl in EBSS and EBSS supplemented with 20μM dantrolene. *$p<0.05$, **$p<0.01$, ns = $p>0.05$. N=3

PI imaging analysis of neurons and microglia in the presence of dantrolene

Neurons co-stained with NeuN and PI were quantified. One-way ANOVAs indicated that there were no statistically significant differences in the number of healthy (p=0.9137), damaged (p=0.9259), or dead (p=0.3423) neurons in EC slices stimulated with Aβ when compared to slices stimulated with KCl. There were also no statistically significant differences in the number of healthy (p=0.9237), damaged (p=0.9440), or dead (p=0.3913) neurons in EC slices stimulated with tau when compared to slices stimulated with KCl (**Figure 4.12**). In the SCN, one-way ANOVAs indicated that there were no statistically significant differences in the number of healthy (p=0.9997), damaged (p=0.5168), or dead (p=0.3214) neurons in slices stimulated with Aβ when compared to slices stimulated with KCl. There were also no statistically significant differences in the number of healthy (p=0.9998), damaged (p=0.5756), or dead (p=0.3778) neurons in slices stimulated with tau when compared to slices stimulated with KCl (**Figure 4.12**). The percentage of total cells that were NeuN positive for each stimulus condition was also determined (Appendix A).

Microglial cells co-stained with IBA1 and PI were quantified. One-way ANOVAs indicated that there were statistically significant differences in the number of healthy (p=0.0012) and damaged (p=0.0023) microglia in EC slices stimulated with tau when compared to slices stimulated with KCl as well as the number of damaged (p=0.0311) microglia in EC slices stimulated with Aβ when compared to slices stimulated with KCl (**Figure 4.13**). There were no statistically significant differences in the number of healthy (p=0.1054) or dead (p=0.9935) microglia in EC slices stimulated with Aβ or dead (p=0.9999) microglia in slices stimulated with tau when compared to slices stimulated with KCl. In the SCN, one-way ANOVAs indicated that there were no statistically significant differences in the number of healthy (p>0.9999), damaged (p>0.9999),

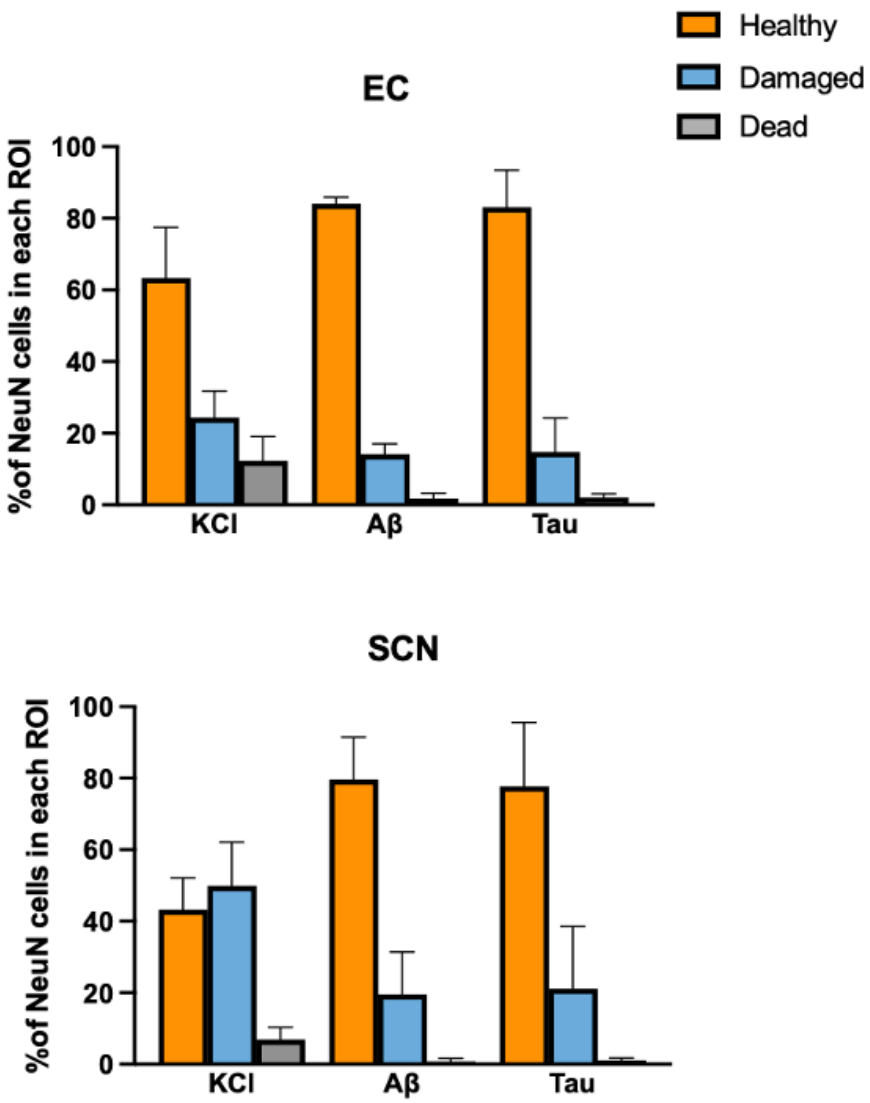


Figure 4.12 Comparison of neuron specific cell death in EC and SCN with dantrolene
Percentage of healthy, damaged, and dead neurons in the EC and SCN after 12 hours, periodically stimulated with 40μM Aβ, tau, or 60 mM KCl in EBSS supplemented with 20μM dantrolene. N=3

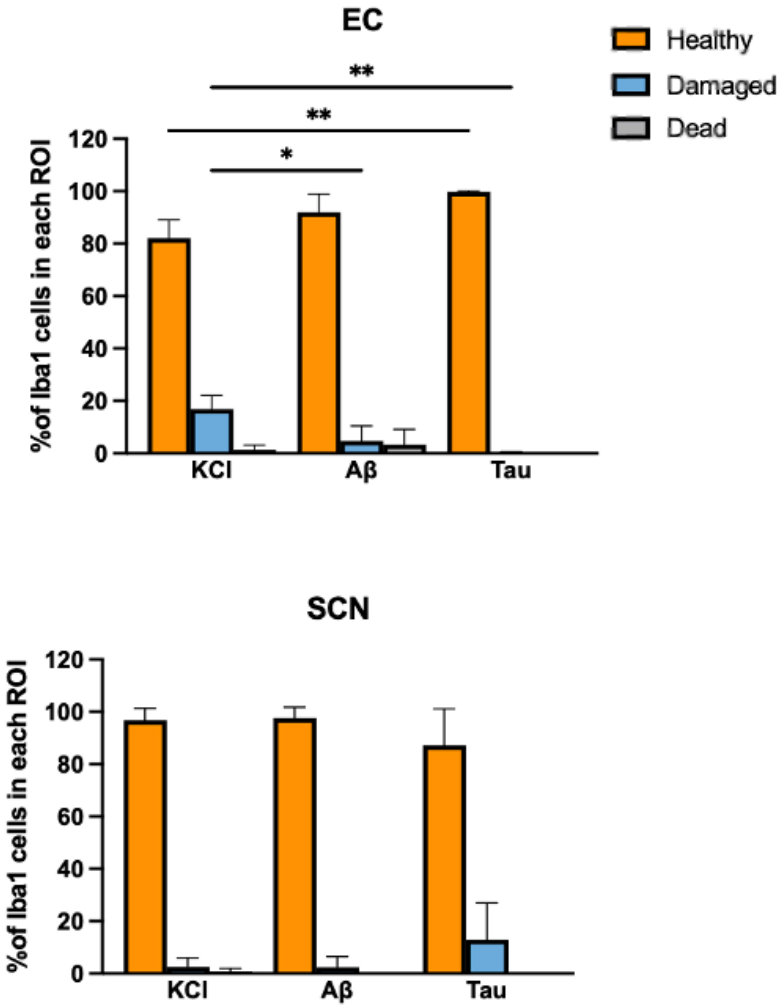


Figure 4.13 Comparison of microglia specific cell death in EC and SCN with dantrolene
Percentage of healthy, damaged, and dead microglia in the EC and SCN after 12 hours, periodically stimulated with 40μM Aβ, tau, or 60 mM KCl in EBSS supplemented with 20μM dantrolene. *p<0.05, **p<0.01, ns = p>0.05. N=3

or dead (p>0.9999) cells in slices stimulated with Aβ when compared to slices stimulated with KCl. There were also no statistically significant differences in the number of healthy (p=0.7110), damaged (p=0.6368), or dead (p>0.9999) cells in slices stimulated with tau when compared to slices stimulated with KCl (**Figure 4.13**). The percentage of total cells that were IBA1 positive for each stimulus condition was also determined (Appendix A).

When comparing the cell-type specific PI staining data for these tissues compared to those maintained in EBSS not supplemented with dantrolene, in the EC there were no statistically significant differences in the percent of healthy neurons in the KCl (p=0.9839), Aβ (p=0.4750), and tau (p=0.5688) conditions at the end of the 12 hours (**Figure 4.14**), or healthy microglia in the KCl (p=0.4631), Aβ (p=0.9861), and tau (p=0.1097) conditions (**Figure 4.15**). In the SCN, there were no statistically significant differences in the percent of healthy neurons in the KCl (p=0.1942), Aβ (p=0.9997), and tau (p=0.9047) conditions at the end of the 12 hours (**Figure 4.14**), or healthy microglia in the KCl (p=0.5697), Aβ (p=0.9971), and tau (p=0.9998) conditions (**Figure 4.15**).

LDH Analysis

One-way ANOVAs comparing fluorescence levels of the samples, combining the data across the 12-hour incubation period, determined there were statistically significant differences for both the EC and SCN. Pairwise comparisons for EC slices treated with Aβ (p=0.0336) indicated a significant increase in LDH was release but no statistically significant differences for tau (p=0.1993) compared to slices treated with KCl (**Figure 4.16**). For SCN tissue slices, pairwise comparisons indicated that significantly more LDH was released after treatment with Aβ compared to KCl (p=0.0120) but not tau (p=0.1478) (**Figure 4.16**). Thus, these data indicate that, in the presence of dantrolene, LDH release due to peptide stimulation over time is changed.

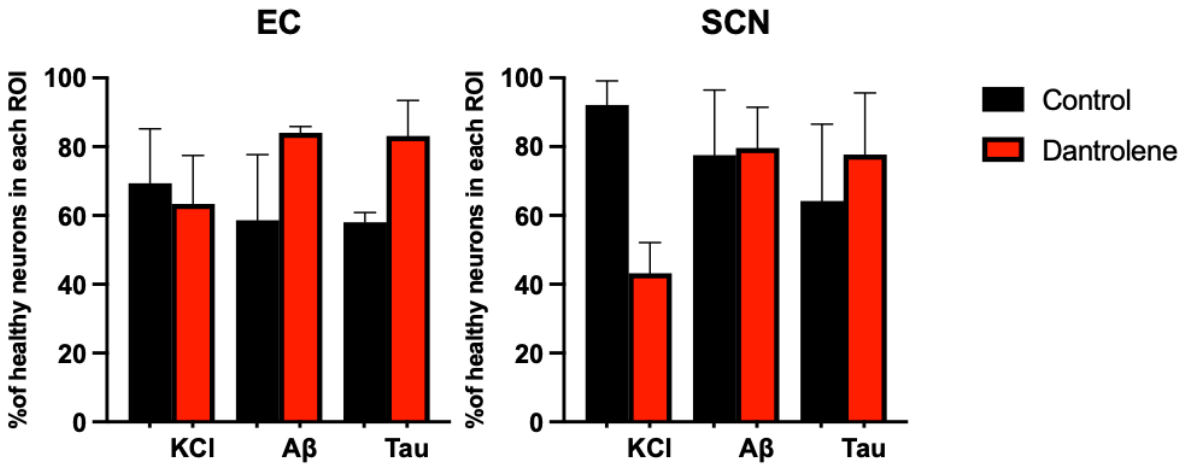


Figure 4.14 Comparison of healthy neurons in EC and SCN Total percentage of healthy neurons in the EC and SCN after 12 hours, periodically stimulated with 40μM Aβ, tau, or 60 mM KCl with just EBSS and EBSS supplemented with 20μM dantrolene. N=3

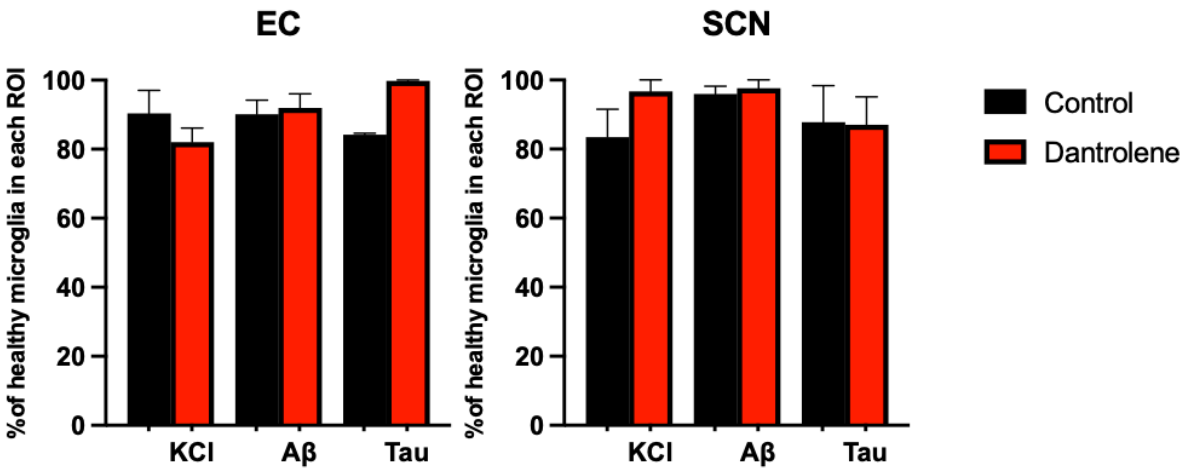


Figure 4.15 Comparison of healthy microglia in EC and SCN Total percentage of healthy microglia in the EC and SCN after 12 hours, periodically stimulated with 40μM Aβ, tau, or 60 mM KCl with just EBSS and EBSS supplemented with 20μM dantrolene. N=3

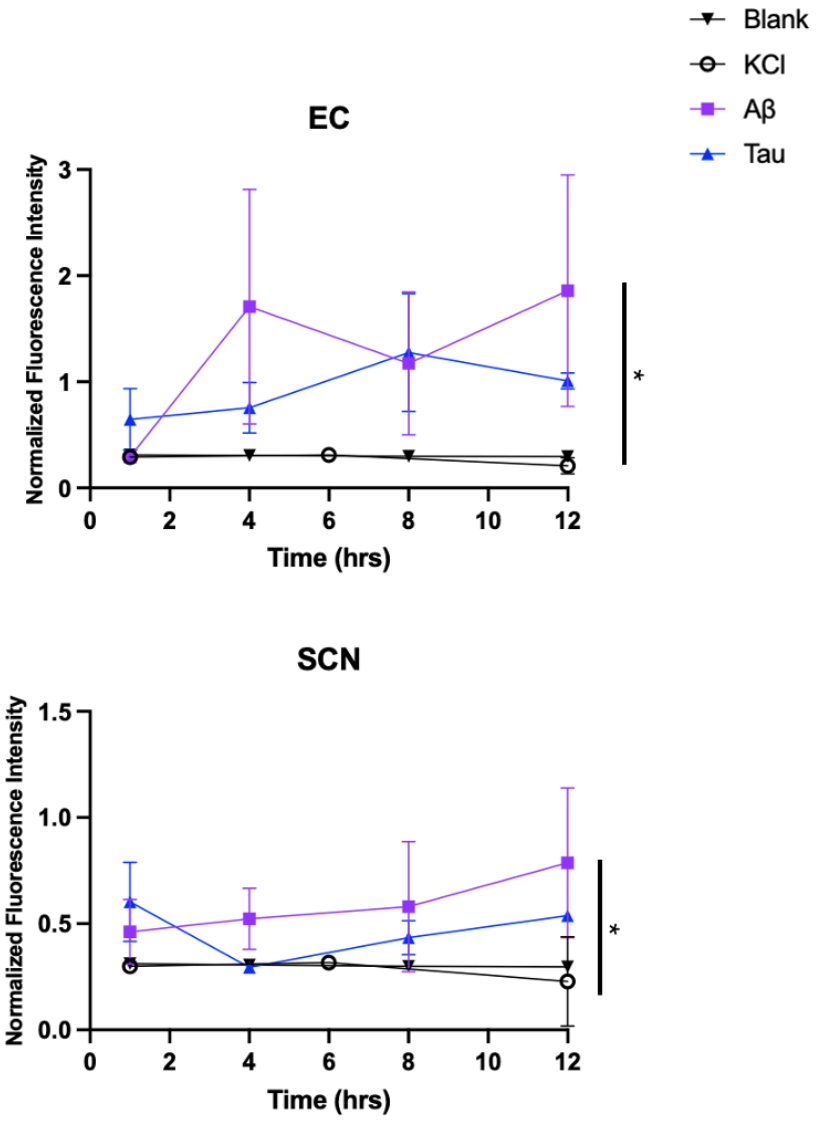


Figure 4.16 Quantified LDH release from the EC and SCN with dantrolene
Normalized fluorescence intensity of released LDH over 12 hours from EC and SCN slice periodically stimulated with 60mM KCl, 40µM Aβ, and 40µM tau in EBSS supplemented with 20µM dantrolene. *$p<0.05$, ns = $p > 0.05$. N=3

Summary and Conclusions

Through the use of the microfluidic system we have developed, these experiments have generated a number of novel insights into acute effects of Aβ and tau peptides on *ex vivo* brain tissue. Using calcium imaging we have shown, for the first time, that upon stimulation with Aβ, tau, and Aβ:tau, increases in intracellular Ca^{2+} are induced quickly (within 1 minute) in *ex vivo* brain slices containing EC and SCN regions. The increases are similar in size to those induced by KCl stimulation. While PI staining did not reveal any differences in cell death due to peptide stimulation, LDH analysis revealed increased LDH release from both the EC and SCN tissue slices in response to peptide stimulation, in line with result from previous work (Chapter 2). We also, for the first time, began to explore which cell types within these two brain regions are affected by Aβ and tau stimulation. In particular, we reveal increased microglia death in the EC with Aβ:tau stimulation. When using dantrolene to inhibit release from intracellular calcium stores, increases in intracellular Ca^{2+} are still observed, but the overall health of both SCN and EC brain slices is improved, especially in respect to Aβ and tau stimulation, as indicated by both PI and LDH assays. The implications of these findings and directions for future research are discussed in the next chapter.

Chapter 5: Summary and Conclusions

Alzheimer's disease (AD) is a progressive and irreversible neurodegenerative disease that damages parts of the brain responsible for memory and learning.[1,22] Accumulation of the peptides amyloid beta (Aβ) and tau are hypothesized to be either a trigger or result of AD and can contribute to the pathological damage seen with AD.[2–4] Although the clinical symptoms, such as memory loss and confusion, seem new at their time of onset, the changes that occur within the brain to cause them are thought to begin decades before the symptoms even show up.[1] As a result, much research around AD is done at a point when it would be too late to even treat the disease should meaningful therapeutic targets be identified. Thus, it is important to study the brain at the initial onset of AD, before these detrimental changes to the brain have taken place. This work aimed to bridge the gap and investigate changes in the brain upon initial exposure and accumulation of Aβ and tau. Specifically, we focused on the entorhinal cortex (EC), one of the first regions effected by peptide accumulation, and the suprachiasmatic nucleus (SCN), due to increasing evidence of circadian rhythm changes in AD patients.

In a collaborative study with Dr. Thanh Do and colleagues (summarized in Chapter 2), we began by isolating acute coronal brain tissue slices containing the SCN or EC from C75Bl/6 mice and maintaining them in Hatton-style brain interface dishes. Slices were exposed to 40μM Aβ, tau or Aβ:tau throughout a 12-hour incubation period. During the 12 hours, media was collected every 2 hours to assess lactate dehydrogenase (LDH) release in response to the peptide treatment and at the end of the 12 hours slices were stained with the cell death marker propidium iodide (PI). Based on this analysis, we observed that within the first 12 hours of exogenous peptide exposure in the SCN, Aβ increased LDH release indicating cell death, but histological analysis of PI staining did not yield any statistically significant difference in cell death between tissues exposed to peptides compared to those that were not. We also observed that in the EC,

Aβ:tau caused significant differences in cell death compared to all other experimental conditions via histological analysis of PI staining, though this is not reflected in the amount of LDH released. Difference in results of the two assays suggests that LDH release is a more sensitive marker of cell damage/death compared to PI staining, having the advantage of providing information on changes in cell damage over time, while PI staining only provides information on the extent of cell damage at the time of tissue fixation. This work demonstrated, for the first time, the initial toxicity of Aβ in acute *ex vivo* slices containing the SCN and surrounding anterior hypothalamus. Moving forward, we wanted to expand on this work and look closer at the immediate physiological changes taking place in tissues slice as a response to peptide exposure.

Next, we worked to develop microfluidic technology that could help us expand on the previous study and address some of its limitations. The Hatton-style brain interface dishes are a gold standard for maintaining *ex vivo* brain tissue slices, but they do not allow for simultaneous analysis of real-time physiological responses such as changes in intracellular calcium or released substances. Through a collaboration with Dr. Chris Baker and colleagues (summarized in Chapter 3) we developed a novel microfluidic device that allows for real-time calcium imaging upon tissue stimulation. Preliminary experiments demonstrated the ability to pause media droplets in the tissue chamber for up to 8 minutes at a time, allowing for released analytes to be captured within droplets without harming long-term tissue viability. Analysis showed we were able to visualize instant (within seconds) changes in intracellular calcium in the EC and SCN when stimulated with potassium chloride (KCl).

Confident in the new microfluidic system, we moved on to looking more closely at the effects of Aβ and tau stimulation in the EC and SCN through both real-time calcium imaging and off-line analysis of released substances. Research through the years has failed to pinpoint

whether Aβ and tau accumulation is causative or correlative to AD. This work aimed to investigate changes within the EC and SCN immediately after initial exposure to Aβ and tau. In a collaboration with Drs. Paul Allen and Thanh Do, calcium (Ca^{2+}) imaging of tissues containing the EC or SCN upon stimulation with Aβ and tau revealed real-time changes in intracellular Ca^{2+} concentrations as a direct response to peptide exposure similar to changes seen due to KCl depolarization. Additionally, we observed increased LDH release in both regions following peptide stimulation. These data are consistent with the idea that Ca^{2+} dysregulation due to the presence of Aβ and tau may contribute to AD progression. Histological analysis of cell death after 12 hours of initial peptide exposure reveals no significant differences in the amount of cell death with Aβ or tau stimulation in the SCN, consistent with previous findings. However, when comparing cell health between regions, we observed that the SCN is significantly healthier than the EC in the Aβ:tau condition. A deeper dive into cell type specific cell health shows no significant differences in neuronal cell death but does show increased microglial cell death in the EC with Aβ:tau stimulation. Finally, we investigated a potential source of the increased intracellular Ca^{2+}, specifically release from intracellular stores through ryanodine channels. Treatment with dantrolene, a selective blocker of ryanodine receptors, did not suppress the intracellular Ca^{2+} changes seen due to peptide stimulation, but it did lead to an increase in overall healthy cells in tissues stimulated with Aβ. Specifically, we observed a significant difference in the number of healthy cells in tissues stimulated with Aβ in the presence of dantrolene compared to without dantrolene. Also, dantrolene prevented the increase in LDH release in response to tau treatment and reduced the significance of Aβ induced release compared to KCl. Together these data are consistent with Aβ and tau contributing to changes in the brain that can, over decades, lead to characteristics of AD pathology beyond normal aging, and that dantrolene may be an

effective treatment to decrease or slow their pathological effects. Due to time constraints, the effect of dantrolene on Aβ:tau stimulation was not done. The combination of both peptides yielded increased cell death in the EC, so investigating how dantrolene influences this response is worth future exploration.

While the presented results are novel, interesting, and elucidate some changes within the brain at the initial exposure of peptides related to AD, further research could continue to fill in the gaps in knowledge about early stages of AD. The design of the developed microfluidic device allows for offline analysis of time-stamped samples of analytes of interest, in this case LDH. This could be expanded into a proteomics study to identify more broadly any substances released by brain tissues upon initial exposure to Aβ and tau. Obvious targets of interest would be pro-inflammatory cytokines, like TNF-α or IL-6, whose dysregulation, specifically overproduction, has already been implicated in AD progression.[159–161] A more thorough understanding of the early effects of Aβ and tau could provide important clues to changes occurring early in the onset of AD that could possibly be used as a diagnostic tool before cognitive symptoms are even present. This is appealing due to AD's irreversible nature, as catching pathological changes as early as possible may lead to a better chance of preventing damage before it can occur.

Additionally, taking a closer look at the role of other possible players in plaque and fibril clearance, such as astrocytes and exosomes, may elucidate why some forms, misfolded or otherwise, of Aβ and tau are more prone to toxicity and disease pathology than others. We did not analyze changes in astrocytes in these experiments. Given current data implicating astrocytes in both positive and negative contributions to AD progression[162,163] investigating how Aβ and tau affect their health will be important in the future.

Finally, additional improvements to microfluidic device will be important. For example, expanding it to include more input channels and having multiple slice chambers would allow for high throughput analysis of tissue slices in future experiments. Incorporating multielectrode arrays into the slice chambers would allow simultaneous electrical recordings of the tissues. Also, developing ways to analyze released substances in real time as they exit the device would speed data generation.

List of References

(1) 2024 Alzheimer's Disease Facts and Figures. *Alzheimer's Dement.* **2024**, *20* (5), 3708–3821. https://doi.org/10.1002/alz.13809.

(2) Lane, C. A.; Hardy, J.; Schott, J. M. Alzheimer's Disease. *Eur. J. Neurol.* **2018**, *25* (1), 59–70. https://doi.org/10.1111/ene.13439.

(3) Hippius, H.; Neundörfer, G. The Discovery of Alzheimer's Disease. *Dialogues Clin. Neurosci.* **2003**, *5* (1), 101–108. https://doi.org/10.31887/DCNS.2003.5.1/hhippius.

(4) Kametani, F.; Hasegawa, M. Reconsideration of Amyloid Hypothesis and Tau Hypothesis in Alzheimer's Disease. *Front. Neurosci.* **2018**, *12*. https://doi.org/10.3389/fnins.2018.00025.

(5) Tabaton, M.; Zhu, X.; Perry, G.; Smith, M. A.; Giliberto, L. Signaling Effect of Amyloid-B42 on the Processing of AβPP. *Exp. Neurol.* **2010**, *221* (1), 18–25. https://doi.org/10.1016/j.expneurol.2009.09.002.

(6) Zou, K.; Gong, J.-S.; Yanagisawa, K.; Michikawa, M. A Novel Function of Monomeric Amyloid β-Protein Serving as an Antioxidant Molecule against Metal-Induced Oxidative Damage. *J. Neurosci.* **2002**, *22* (12), 4833–4841. https://doi.org/10.1523/JNEUROSCI.22-12-04833.2002.

(7) Baruch-Suchodolsky, R.; Fischer, B. Aβ 40 , Either Soluble or Aggregated, Is a Remarkably Potent Antioxidant in Cell-Free Oxidative Systems. *Biochemistry* **2009**, *48* (20), 4354–4370. https://doi.org/10.1021/bi802361k.

(8) Yao, Z.; Papadopoulos, V. Function of B-amyloid in Cholesterol Transport: A Lead to Neurotoxicity. *FASEB J.* **2002**, *16* (12), 1677–1679. https://doi.org/10.1096/fj.02-0285fje.

(9) Igbavboa, U.; Sun, G. Y.; Weisman, G. A.; He, Y.; Wood, W. G. Amyloid β-Protein

Stimulates Trafficking of Cholesterol and Caveolin-1 from the Plasma Membrane to the Golgi Complex in Mouse Primary Astrocytes. *Neuroscience* **2009**, *162* (2), 328–338. https://doi.org/10.1016/j.neuroscience.2009.04.049.

(10) Luo, Y. BACE1 (β-Secretase) Knockout Mice Do Not Acquire Compensatory Gene Expression Changes or Develop Neural Lesions over Time. *Neurobiol. Dis.* **2003**, *14* (1), 81–88. https://doi.org/10.1016/S0969-9961(03)00104-9.

(11) Luo, Y.; Bolon, B.; Kahn, S.; Bennett, B. D.; Babu-Khan, S.; Denis, P.; Fan, W.; Kha, H.; Zhang, J.; Gong, Y.; et al. Mice Deficient in BACE1, the Alzheimer's β-Secretase, Have Normal Phenotype and Abolished β-Amyloid Generation. *Nat. Neurosci.* **2001**, *4* (3), 231–232. https://doi.org/10.1038/85059.

(12) Roberds, S. L. BACE Knockout Mice Are Healthy despite Lacking the Primary Beta-Secretase Activity in Brain: Implications for Alzheimer's Disease Therapeutics. *Hum. Mol. Genet.* **2001**, *10* (12), 1317–1324. https://doi.org/10.1093/hmg/10.12.1317.

(13) Wood, J. G.; Zinsmeister, P. Immunohistochemical Evidence for Reorganization of Tau in the Plaques and Tangles in Alzheimer's Dissease. *Histochem. J.* **1989**, *21* (11), 659–662. https://doi.org/10.1007/BF01002486.

(14) Gastard, M. C.; Troncoso, J. C.; Koliatsos, V. E. Caspase Activation in the Limbic Cortex of Subjects with Early Alzheimer's Disease. *Ann. Neurol.* **2003**, *54* (3), 393–398. https://doi.org/10.1002/ana.10680.

(15) d'Errico, P.; Meyer-Luehmann, M. Mechanisms of Pathogenic Tau and Aβ Protein Spreading in Alzheimer's Disease. *Front. Aging Neurosci.* **2020**, *12*. https://doi.org/10.3389/fnagi.2020.00265.

(16) Basu, J.; Siegelbaum, S. A. The Corticohippocampal Circuit, Synaptic Plasticity, and

Memory. *Cold Spring Harb. Perspect. Biol.* **2015**, *7* (11), a021733. https://doi.org/10.1101/cshperspect.a021733.

(17) Ye, J.; Witter, M. P.; Moser, M.-B.; Moser, E. I. Entorhinal Fast-Spiking Speed Cells Project to the Hippocampus. *Proc. Natl. Acad. Sci.* **2018**, *115* (7). https://doi.org/10.1073/pnas.1720855115.

(18) Igarashi, K. M.; Lu, L.; Colgin, L. L.; Moser, M.-B.; Moser, E. I. Coordination of Entorhinal–Hippocampal Ensemble Activity during Associative Learning. *Nature* **2014**, *510* (7503), 143–147. https://doi.org/10.1038/nature13162.

(19) Grothe, M. J.; Barthel, H.; Sepulcre, J.; Dyrba, M.; Sabri, O.; Teipel, S. J.; Weiner, M.; Aisen, P.; Weiner, M.; Aisen, P.; et al. In Vivo Staging of Regional Amyloid Deposition. *Neurology* **2017**, *89* (20), 2031–2038. https://doi.org/10.1212/WNL.0000000000004643.

(20) Serrano-Pozo, A.; Frosch, M. P.; Masliah, E.; Hyman, B. T. Neuropathological Alterations in Alzheimer Disease. *Cold Spring Harb. Perspect. Med.* **2011**, *1* (1), a006189–a006189. https://doi.org/10.1101/cshperspect.a006189.

(21) Braak, H.; Braak, E. Neuropathological Stageing of Alzheimer-Related Changes. *Acta Neuropathol.* **1991**, *82* (4), 239–259. https://doi.org/10.1007/BF00308809.

(22) Igarashi, K. M. Entorhinal Cortex Dysfunction in Alzheimer's Disease. *Trends Neurosci.* **2023**, *46* (2), 124–136. https://doi.org/10.1016/j.tins.2022.11.006.

(23) Rigat, L.; Ouk, K.; Kramer, A.; Priller, J. Dysfunction of Circadian and Sleep Rhythms in the Early Stages of Alzheimer's Disease. *Acta Physiol.* **2023**, *238* (2). https://doi.org/10.1111/apha.13970.

(24) Musiek, E. S.; Bhimasani, M.; Zangrilli, M. A.; Morris, J. C.; Holtzman, D. M.; Ju, Y.-E. S. Circadian Rest-Activity Pattern Changes in Aging and Preclinical Alzheimer Disease.

JAMA Neurol. **2018**, *75* (5), 582. https://doi.org/10.1001/jamaneurol.2017.4719.

(25) Leng, Y.; Musiek, E. S.; Hu, K.; Cappuccio, F. P.; Yaffe, K. Association between Circadian Rhythms and Neurodegenerative Diseases. *Lancet Neurol.* **2019**, *18* (3), 307–318. https://doi.org/10.1016/S1474-4422(18)30461-7.

(26) van Someren, E. J. W.; Hagebeuk, E. E. O.; Lijzenga, C.; Scheltens, P.; de Rooij, S. E. J. A.; Jonker, C.; Pot, A.-M.; Mirmiran, M.; Swaab, D. F. Circadian Rest—Activity Rhythm Disturbances in Alzheimer's Disease. *Biol. Psychiatry* **1996**, *40* (4), 259–270. https://doi.org/10.1016/0006-3223(95)00370-3.

(27) Farajnia, S.; Michel, S.; Deboer, T.; VanderLeest, H. T.; Houben, T.; Rohling, J. H. T.; Ramkisoensing, A.; Yasenkov, R.; Meijer, J. H. Evidence for Neuronal Desynchrony in the Aged Suprachiasmatic Nucleus Clock. *J. Neurosci.* **2012**, *32* (17), 5891–5899. https://doi.org/10.1523/JNEUROSCI.0469-12.2012.

(28) Zhou, J. VIP Neurons in the Human SCN in Relation to Sex, Age, and Alzheimer's Disease. *Neurobiol. Aging* **1995**, *16* (4), 571–576. https://doi.org/10.1016/0197-4580(95)00043-E.

(29) Harper, D. G.; Stopa, E. G.; Kuo-Leblanc, V.; McKee, A. C.; Asayama, K.; Volicer, L.; Kowall, N.; Satlin, A. Dorsomedial SCN Neuronal Subpopulations Subserve Different Functions in Human Dementia. *Brain* **2008**, *131* (6), 1609–1617. https://doi.org/10.1093/brain/awn049.

(30) Singer, R.; Alia, A. Evaluation of Suprachiasmatic Nucleus in Alzheimer's Disease with Non-Invasive Magnetic Resonance Methods. *Neural Regen. Res.* **2022**, *17* (8), 1753–1754. https://doi.org/10.4103/1673-5374.332136.

(31) Roy, U.; Stute, L.; Höfling, C.; Hartlage-Rübsamen, M.; Matysik, J.; Roβner, S.; Alia, A.

Sex- and Age-Specific Modulation of Brain GABA Levels in a Mouse Model of Alzheimer's Disease. *Neurobiol. Aging* **2018**, *62*, 168–179. https://doi.org/10.1016/j.neurobiolaging.2017.10.015.

(32) Astashkina, A.; Mann, B.; Grainger, D. W. A Critical Evaluation of in Vitro Cell Culture Models for High-Throughput Drug Screening and Toxicity. *Pharmacol. Ther.* **2012**, *134* (1), 82–106. https://doi.org/10.1016/j.pharmthera.2012.01.001.

(33) Sainz, A.; Perez-Cerda, F.; Perez-Samartin, A.; Panicker, M.; Ruiz, A.; Matute, C. Pros and Cons of Human Brain Organoids to Study Alzheimer's Disease. *aging Dis.* **2024**. https://doi.org/10.14336/AD.2024.1409.

(34) Lossi, L.; Alasia, S.; Salio, C.; Merighi, A. Cell Death and Proliferation in Acute Slices and Organotypic Cultures of Mammalian CNS. *Prog. Neurobiol.* **2009**, *88* (4), 221–245. https://doi.org/10.1016/j.pneurobio.2009.01.002.

(35) Gähwiler, B. H.; Capogna, M.; Debanne, D.; McKinney, R. A.; Thompson, S. M. Organotypic Slice Cultures: A Technique Has Come of Age. *Trends Neurosci.* **1997**, *20* (10), 471–477. https://doi.org/10.1016/S0166-2236(97)01122-3.

(36) Li, C.-L.; McIlwain, H. Maintenance of Resting Membrane Potentials in Slices of Mammalian Cerebral Cortex and Other Tissues in Vitro. *J. Physiol.* **1957**, *139* (2), 178–190. https://doi.org/10.1113/jphysiol.1957.sp005885.

(37) Yamamoto, C.; McIlwain, H. ELECTRICAL ACTIVITIES IN THIN SECTIONS FROM THE MAMMALIAN BRAIN MAINTAINED IN CHEMICALLY-DEFINED MEDIA IN VITRO. *J. Neurochem.* **1966**, *13* (12), 1333–1343. https://doi.org/10.1111/j.1471-4159.1966.tb04296.x.

(38) Dingledine, R.; Dodd, J.; Kelly, J. S. The in Vitro Brain Slice as a Useful

Neurophysiological Preparation for Intracellular Recording. *J. Neurosci. Methods* **1980**, *2* (4), 323–362. https://doi.org/10.1016/0165-0270(80)90002-3.

(39) Reid, K. H.; Edmonds, H. L.; Schurr, A.; Tseng, M. T.; West, C. A. Pitfalls in the Use of Brain Slices. *Prog. Neurobiol.* **1988**, *31* (1), 1–18. https://doi.org/10.1016/0301-0082(88)90020-2.

(40) Kékesi, O.; Buskila, Y. Method for Prolonged Incubation of Brain Slices. *Bio-protocol* **2020**, *10* (14), e3683. https://doi.org/10.21769/BioProtoc.3683.

(41) Haas, H. L.; Schaerer, B.; Vosmansky, M. A Simple Perfusion Chamber for the Study of Nervous Tissue Slices in Vitro. *J. Neurosci. Methods* **1979**, *1* (4), 323–325. https://doi.org/10.1016/0165-0270(79)90021-9.

(42) Hájos, N.; Ellender, T. J.; Zemankovics, R.; Mann, E. O.; Exley, R.; Cragg, S. J.; Freund, T. F.; Paulsen, O. Maintaining Network Activity in Submerged Hippocampal Slices: Importance of Oxygen Supply. *Eur. J. Neurosci.* **2009**, *29* (2), 319–327. https://doi.org/10.1111/j.1460-9568.2008.06577.x.

(43) Hájos, N.; Mody, I. Establishing a Physiological Environment for Visualized in Vitro Brain Slice Recordings by Increasing Oxygen Supply and Modifying ACSF Content. *J. Neurosci. Methods* **2009**, *183* (2), 107–113. https://doi.org/10.1016/j.jneumeth.2009.06.005.

(44) Whitesides, G. M. The Origins and the Future of Microfluidics. *Nature* **2006**, *442* (7101), 368–373. https://doi.org/10.1038/nature05058.

(45) Huang, Y.; Williams, J. C.; Johnson, S. M. Brain Slice on a Chip: Opportunities and Challenges of Applying Microfluidic Technology to Intact Tissues. *Lab Chip* **2012**, *12* (12), 2103. https://doi.org/10.1039/c2lc21142d.

(46) Passeraub, P. A.; Almeida, A. C.; Thakor, N. V. Design, Microfabrication and Analysis of a Microfluidic Chamber for the Perfusion of Brain Tissue Slices. *Biomed. Microdevices* **2003**, *5* (2), 147–155. https://doi.org/10.1023/A:1024547413721.

(47) Blake, A. J.; Pearce, T. M.; Rao, N. S.; Johnson, S. M.; Williams, J. C. Multilayer PDMS Microfluidic Chamber for Controlling Brain Slice Microenvironment. *Lab Chip* **2007**, *7* (7), 842. https://doi.org/10.1039/b704754a.

(48) Tang, Y. T.; Kim, J.; López-Valdés, H. E.; Brennan, K. C.; Ju, Y. S. Development and Characterization of a Microfluidic Chamber Incorporating Fluid Ports with Active Suction for Localized Chemical Stimulation of Brain Slices. *Lab Chip* **2011**, *11* (13), 2247. https://doi.org/10.1039/c1lc20197b.

(49) Mauleon, G.; Fall, C. P.; Eddington, D. T. Precise Spatial and Temporal Control of Oxygen within In Vitro Brain Slices via Microfluidic Gas Channels. *PLoS One* **2012**, *7* (8), e43309. https://doi.org/10.1371/journal.pone.0043309.

(50) Saleheen, A.; Acharyya, D.; Prosser, R. A.; Baker, C. A. A Microfluidic Bubble Perfusion Device for Brain Slice Culture. *Anal. Methods* **2021**, *13* (11), 1364–1373. https://doi.org/10.1039/D0AY02291H.

(51) Goedert, M. Alpha-Synuclein and Neurodegenerative Diseases. *Nat. Rev. Neurosci.* **2001**, *2* (7), 492–501. https://doi.org/10.1038/35081564.

(52) Rochet, J.-C.; Lansbury, P. T. Amyloid Fibrillogenesis: Themes and Variations. *Curr. Opin. Struct. Biol.* **2000**, *10* (1), 60–68. https://doi.org/10.1016/S0959-440X(99)00049-4.

(53) Selkoe, D. J. Alzheimer's Disease: Genes, Proteins, and Therapy. *Physiol. Rev.* **2001**, *81* (2), 741–766. https://doi.org/10.1152/physrev.2001.81.2.741.

(54) Zoghbi, H. Y.; Orr, H. T. Glutamine Repeats and Neurodegeneration. *Annu. Rev.*

Neurosci. **2000**, *23* (1), 217–247. https://doi.org/10.1146/annurev.neuro.23.1.217.

(55) Benilova, I.; Karran, E.; De Strooper, B. The Toxic Aβ Oligomer and Alzheimer's Disease: An Emperor in Need of Clothes. *Nat. Neurosci.* **2012**, *15* (3), 349–357. https://doi.org/10.1038/nn.3028.

(56) Kayed, R.; Lasagna-Reeves, C. A. Molecular Mechanisms of Amyloid Oligomers Toxicity. *J. Alzheimer's Dis.* **2012**, *33* (s1), S67–S78. https://doi.org/10.3233/JAD-2012-129001.

(57) Haass, C.; Selkoe, D. J. Soluble Protein Oligomers in Neurodegeneration: Lessons from the Alzheimer's Amyloid β-Peptide. *Nat. Rev. Mol. Cell Biol.* **2007**, *8* (2), 101–112. https://doi.org/10.1038/nrm2101.

(58) Baglioni, S.; Casamenti, F.; Bucciantini, M.; Luheshi, L. M.; Taddei, N.; Chiti, F.; Dobson, C. M.; Stefani, M. Prefibrillar Amyloid Aggregates Could Be Generic Toxins in Higher Organisms. *J. Neurosci.* **2006**, *26* (31), 8160–8167. https://doi.org/10.1523/JNEUROSCI.4809-05.2006.

(59) Hamley, I. W. The Amyloid Beta Peptide: A Chemist's Perspective. Role in Alzheimer's and Fibrillization. *Chem. Rev.* **2012**, *112* (10), 5147–5192. https://doi.org/10.1021/cr3000994.

(60) Binder, L. I.; Guillozet-Bongaarts, A. L.; Garcia-Sierra, F.; Berry, R. W. Tau, Tangles, and Alzheimer's Disease. *Biochim. Biophys. Acta - Mol. Basis Dis.* **2005**, *1739* (2–3), 216–223. https://doi.org/10.1016/j.bbadis.2004.08.014.

(61) Walsh, D. M.; Teplow, D. B. Alzheimer's Disease and the Amyloid β-Protein; 2012; pp 101–124. https://doi.org/10.1016/B978-0-12-385883-2.00012-6.

(62) Hardy, J. A.; Higgins, G. A. Alzheimer's Disease: The Amyloid Cascade Hypothesis.

Science (80-.). **1992**, *256* (5054), 184–185. https://doi.org/10.1126/science.1566067.

(63) Hardy, J.; Duff, K.; Hardy, K. G.; Perez-Tur, J.; Hutton, M. Genetic Dissection of Alzheimer's Disease and Related Dementias: Amyloid and Its Relationship to Tau. *Nat. Neurosci.* **1998**, *1* (5), 355–358. https://doi.org/10.1038/1565.

(64) Spires-Jones, T. L.; Stoothoff, W. H.; de Calignon, A.; Jones, P. B.; Hyman, B. T. Tau Pathophysiology in Neurodegeneration: A Tangled Issue. *Trends Neurosci.* **2009**, *32* (3), 150–159. https://doi.org/10.1016/j.tins.2008.11.007.

(65) HUTTON, M. Molecular Genetics of Chromosome 17 Tauopathies. *Ann. N. Y. Acad. Sci.* **2000**, *920* (1), 63–73. https://doi.org/10.1111/j.1749-6632.2000.tb06906.x.

(66) Götz, J.; Chen, F.; van Dorpe, J.; Nitsch, R. M. Formation of Neurofibrillary Tangles in P301L Tau Transgenic Mice Induced by Aβ42 Fibrils. *Science (80-.).* **2001**, *293* (5534), 1491–1495. https://doi.org/10.1126/science.1062097.

(67) Jacobs, H. I. L.; Hedden, T.; Schultz, A. P.; Sepulcre, J.; Perea, R. D.; Amariglio, R. E.; Papp, K. V.; Rentz, D. M.; Sperling, R. A.; Johnson, K. A. Structural Tract Alterations Predict Downstream Tau Accumulation in Amyloid-Positive Older Individuals. *Nat. Neurosci.* **2018**, *21* (3), 424–431. https://doi.org/10.1038/s41593-018-0070-z.

(68) Kwak, S. S.; Washicosky, K. J.; Brand, E.; von Maydell, D.; Aronson, J.; Kim, S.; Capen, D. E.; Cetinbas, M.; Sadreyev, R.; Ning, S.; et al. Amyloid-B42/40 Ratio Drives Tau Pathology in 3D Human Neural Cell Culture Models of Alzheimer's Disease. *Nat. Commun.* **2020**, *11* (1), 1377. https://doi.org/10.1038/s41467-020-15120-3.

(69) Bloom, G. S. Amyloid-β and Tau. *JAMA Neurol.* **2014**, *71* (4), 505. https://doi.org/10.1001/jamaneurol.2013.5847.

(70) Braak, H.; Del Tredici, K. Neuroanatomy and Pathology of Sporadic Alzheimer's

Disease; 2015; pp 1–162. https://doi.org/10.1007/978-3-319-12679-1_1.

(71) Braak, H.; Del Tredici, K. Are Cases with Tau Pathology Occurring in the Absence of Aβ Deposits Part of the AD-Related Pathological Process? *Acta Neuropathol.* **2014**, *128* (6), 767–772. https://doi.org/10.1007/s00401-014-1356-1.

(72) Johnson, K. A.; Schultz, A.; Betensky, R. A.; Becker, J. A.; Sepulcre, J.; Rentz, D.; Mormino, E.; Chhatwal, J.; Amariglio, R.; Papp, K.; et al. Tau Positron Emission Tomographic Imaging in Aging and Early <scp>A</Scp> Lzheimer Disease. *Ann. Neurol.* **2016**, *79* (1), 110–119. https://doi.org/10.1002/ana.24546.

(73) Guo, J.-P.; Arai, T.; Miklossy, J.; McGeer, P. L. Aβ and Tau Form Soluble Complexes That May Promote Self Aggregation of Both into the Insoluble Forms Observed in Alzheimer's Disease. *Proc. Natl. Acad. Sci.* **2006**, *103* (6), 1953–1958. https://doi.org/10.1073/pnas.0509386103.

(74) Lee, J.-H.; Yang, D.-S.; Goulbourne, C. N.; Im, E.; Stavrides, P.; Pensalfini, A.; Chan, H.; Bouchet-Marquis, C.; Bleiwas, C.; Berg, M. J.; et al. Faulty Autolysosome Acidification in Alzheimer's Disease Mouse Models Induces Autophagic Build-up of Aβ in Neurons, Yielding Senile Plaques. *Nat. Neurosci.* **2022**, *25* (6), 688–701. https://doi.org/10.1038/s41593-022-01084-8.

(75) D'Andrea, M. R.; Nagele, R. G.; Wang, H.; Peterson, P. A.; Lee, D. H. S. Evidence That Neurones Accumulating Amyloid Can Undergo Lysis to Form Amyloid Plaques in Alzheimer's Disease. *Histopathology* **2001**, *38* (2), 120–134. https://doi.org/10.1046/j.1365-2559.2001.01082.x.

(76) Karch, C. M.; Jeng, A. T.; Goate, A. M. Extracellular Tau Levels Are Influenced by Variability in Tau That Is Associated with Tauopathies. *J. Biol. Chem.* **2012**, *287* (51),

42751–42762. https://doi.org/10.1074/jbc.M112.380642.

(77) Chai, X.; Dage, J. L.; Citron, M. Constitutive Secretion of Tau Protein by an Unconventional Mechanism. *Neurobiol. Dis.* **2012**, *48* (3), 356–366. https://doi.org/10.1016/j.nbd.2012.05.021.

(78) Magnoni, S.; Esparza, T. J.; Conte, V.; Carbonara, M.; Carrabba, G.; Holtzman, D. M.; Zipfel, G. J.; Stocchetti, N.; Brody, D. L. Tau Elevations in the Brain Extracellular Space Correlate with Reduced Amyloid-β Levels and Predict Adverse Clinical Outcomes after Severe Traumatic Brain Injury. *Brain* **2012**, *135* (4), 1268–1280. https://doi.org/10.1093/brain/awr286.

(79) Do, T. D.; Economou, N. J.; Chamas, A.; Buratto, S. K.; Shea, J.-E.; Bowers, M. T. Interactions between Amyloid-β and Tau Fragments Promote Aberrant Aggregates: Implications for Amyloid Toxicity. *J. Phys. Chem. B* **2014**, *118* (38), 11220–11230. https://doi.org/10.1021/jp506258g.

(80) Kazmi, S.; Mujeeb, A. A.; Owais, M. Cyclic Undecapeptide Cyclosporin A Mediated Inhibition of Amyloid Synthesis: Implications in Alleviation of Amyloid Induced Neurotoxicity. *Sci. Rep.* **2018**, *8* (1), 17283. https://doi.org/10.1038/s41598-018-35645-4.

(81) von Bergen, M.; Friedhoff, P.; Biernat, J.; Heberle, J.; Mandelkow, E.-M.; Mandelkow, E. Assembly of τ Protein into Alzheimer Paired Helical Filaments Depends on a Local Sequence Motif (306 VQIVYK 311) Forming β Structure. *Proc. Natl. Acad. Sci.* **2000**, *97* (10), 5129–5134. https://doi.org/10.1073/pnas.97.10.5129.

(82) Ganguly, P.; Do, T. D.; Larini, L.; LaPointe, N. E.; Sercel, A. J.; Shade, M. F.; Feinstein, S. C.; Bowers, M. T.; Shea, J.-E. Tau Assembly: The Dominant Role of PHF6 (VQIVYK) in Microtubule Binding Region Repeat R3. *J. Phys. Chem. B* **2015**, *119* (13), 4582–4593.

https://doi.org/10.1021/acs.jpcb.5b00175.

(83) Gray, A. L. H.; Sawaya, M. R.; Acharyya, D.; Lou, J.; Edington, E. M.; Best, M. D.; Prosser, R. A.; Eisenberg, D. S.; Do, T. D. Atomic View of an Amyloid Dodecamer Exhibiting Selective Cellular Toxic Vulnerability in Acute Brain Slices. *Protein Sci.* **2022**, *31* (3), 716–727. https://doi.org/10.1002/pro.4268.

(84) Laake, J. H.; Haug, F.-M.; Wieloch, T.; Ottersen, O. P. A Simple in Vitro Model of Ischemia Based on Hippocampal Slice Cultures and Propidium Iodide Fluorescence. *Brain Res. Protoc.* **1999**, *4* (2), 173–184. https://doi.org/10.1016/S1385-299X(99)00021-5.

(85) Happ, D. F.; Tasker, R. A. A Method for Objectively Quantifying Propidium Iodide Exclusion in Organotypic Hippocampal Slice Cultures. *J. Neurosci. Methods* **2016**, *269*, 1–5. https://doi.org/10.1016/j.jneumeth.2016.05.006.

(86) Sun, H.-S.; French, R. J.; Feng, Z.-P. A Method for Identifying Viable and Damaged Neurons in Adult Mouse Brain Slices. *Acta Histochem.* **2009**, *111* (6), 531–537. https://doi.org/10.1016/j.acthis.2008.06.005.

(87) Macklis, J. D.; Madison, R. D. Progressive Incorporation of Propidium Iodide in Cultured Mouse Neurons Correlates with Declining Electrophysiological Status: A Fluorescence Scale of Membrane Integrity. *J. Neurosci. Methods* **1990**, *31* (1), 43–46. https://doi.org/10.1016/0165-0270(90)90007-3.

(88) Korzeniewski, C.; Callewaert, D. M. An Enzyme-Release Assay for Natural Cytotoxicity. *J. Immunol. Methods* **1983**, *64* (3), 313–320. https://doi.org/10.1016/0022-1759(83)90438-6.

(89) Decker, T.; Lohmann-Matthes, M.-L. A Quick and Simple Method for the Quantitation of

Lactate Dehydrogenase Release in Measurements of Cellular Cytotoxicity and Tumor Necrosis Factor (TNF) Activity. *J. Immunol. Methods* **1988**, *115* (1), 61–69. https://doi.org/10.1016/0022-1759(88)90310-9.

(90) Shin, W. S.; Di, J.; Cao, Q.; Li, B.; Seidler, P. M.; Murray, K. A.; Bitan, G.; Jiang, L. Amyloid β-Protein Oligomers Promote the Uptake of Tau Fibril Seeds Potentiating Intracellular Tau Aggregation. *Alzheimers. Res. Ther.* **2019**, *11* (1), 86. https://doi.org/10.1186/s13195-019-0541-9.

(91) Wallin, C.; Hiruma, Y.; Wärmländer, S. K. T. S.; Huvent, I.; Jarvet, J.; Abrahams, J. P.; Gräslund, A.; Lippens, G.; Luo, J. The Neuronal Tau Protein Blocks in Vitro Fibrillation of the Amyloid-β (Aβ) Peptide at the Oligomeric Stage. *J. Am. Chem. Soc.* **2018**, *140* (26), 8138–8146. https://doi.org/10.1021/jacs.7b13623.

(92) Wiltzius, J. J. W.; Sievers, S. A.; Sawaya, M. R.; Cascio, D.; Popov, D.; Riekel, C.; Eisenberg, D. Atomic Structure of the Cross-β Spine of Islet Amyloid Polypeptide (Amylin). *Protein Sci.* **2008**, *17* (9), 1467–1474. https://doi.org/10.1110/ps.036509.108.

(93) Lin, C.-Y.; Gurlo, T.; Kayed, R.; Butler, A. E.; Haataja, L.; Glabe, C. G.; Butler, P. C. Toxic Human Islet Amyloid Polypeptide (h-IAPP) Oligomers Are Intracellular, and Vaccination to Induce Anti-Toxic Oligomer Antibodies Does Not Prevent h-IAPP–Induced β-Cell Apoptosis in h-IAPP Transgenic Mice. *Diabetes* **2007**, *56* (5), 1324–1332. https://doi.org/10.2337/db06-1579.

(94) Westermark, P.; Andersson, A.; Westermark, G. T. Is Aggregated IAPP a Cause of Beta-Cell Failure in Transplanted Human Pancreatic Islets? *Curr. Diab. Rep.* **2005**, *5* (3), 184–188. https://doi.org/10.1007/s11892-005-0007-2.

(95) Westermark, P.; Engström, U.; Westermark, G. T.; Johnson, K. H.; Permerth, J.;

Betsholtz, C. Islet Amyloid Polypeptide (IAPP) and pro-IAPP Immunoreactivity in Human Islets of Langerhans. *Diabetes Res. Clin. Pract.* **1989**, *7* (3), 219–226. https://doi.org/10.1016/0168-8227(89)90008-9.

(96) Fineman, M.; Weyer, C.; Maggs, D. G.; Strobel, S.; Kolterman, O. G. The Human Amylin Analog, Pramlintide, Reduces Postprandial Hyperglucagonemia in Patients with Type 2 Diabetes Mellitus. *Horm. Metab. Res.* **2002**, *34* (9), 504–508. https://doi.org/10.1055/s-2002-34790.

(97) Fineman, M. S.; Koda, J. E.; Shen, L. Z.; Strobel, S. A.; Maggs, D. G.; Weyer, C.; Kolterman, O. G. The Human Amylin Analog, Pramlintide, Corrects Postprandial Hyperglucagonemia in Patients with Type 1 Diabetes. *Metabolism* **2002**, *51* (5), 636–641. https://doi.org/10.1053/meta.2002.32022.

(98) Im, D.; Heo, C. E.; Son, M. K.; Park, C. R.; Kim, H. I.; Choi, J.-M. Kinetic Modulation of Amyloid-β (1–42) Aggregation and Toxicity by Structure-Based Rational Design. *J. Am. Chem. Soc.* **2022**, *144* (4), 1603–1611. https://doi.org/10.1021/jacs.1c10173.

(99) Dugger, B. N.; Dickson, D. W. Pathology of Neurodegenerative Diseases. *Cold Spring Harb. Perspect. Biol.* **2017**, *9* (7), a028035. https://doi.org/10.1101/cshperspect.a028035.

(100) 2009 Alzheimer's Disease Facts and Figures. *Alzheimer's Dement.* **2009**, *5* (3), 234–270. https://doi.org/10.1016/j.jalz.2009.03.001.

(101) Cermakian, N.; Boivin, D. B. The Regulation of Central and Peripheral Circadian Clocks in Humans. *Obes. Rev.* **2009**, *10* (s2), 25–36. https://doi.org/10.1111/j.1467-789X.2009.00660.x.

(102) Dunlap, J. C. Molecular Bases for Circadian Clocks. *Cell* **1999**, *96* (2), 271–290. https://doi.org/10.1016/S0092-8674(00)80566-8.

(103) Yesavage, J. A.; Noda, A.; Hernandez, B.; Friedman, L.; Cheng, J. J.; Tinklenberg, J. R.; Hallmayer, J.; O'Hara, R.; David, R.; Robert, P.; et al. Circadian Clock Gene Polymorphisms and Sleep–Wake Disturbance in Alzheimer Disease. *Am. J. Geriatr. Psychiatry* **2011**, *19* (7), 635–643. https://doi.org/10.1097/JGP.0b013e31820d92b2.

(104) Van Someren, E. J. W. Circadian and Sleep Disturbances in the Elderly. *Exp. Gerontol.* **2000**, *35* (9–10), 1229–1237. https://doi.org/10.1016/S0531-5565(00)00191-1.

(105) Bombois, S.; Derambure, P.; Pasquier, F.; Monaca, C. Sleep Disorders in Aging and Dementia. *J. Nutr. Heal. aging* **2010**, *14* (3), 212–217. https://doi.org/10.1007/s12603-010-0052-7.

(106) Schmitt, K.; Grimm, A.; Eckert, A. Amyloid-β–Induced Changes in Molecular Clock Properties and Cellular Bioenergetics. *Front. Neurosci.* **2017**, *11*. https://doi.org/10.3389/fnins.2017.00124.

(107) Furtado, A.; Esgalhado, A. J.; Duarte, A. C.; Costa, A. R.; Costa-Brito, A. R.; Carro, E.; Ishikawa, H.; Schroten, H.; Schwerk, C.; Gonçalves, I.; et al. Circadian Rhythmicity of Amyloid-beta-related Molecules Is Disrupted in the Choroid Plexus of a Female Alzheimer's Disease Mouse Model. *J. Neurosci. Res.* **2023**, *101* (4), 524–540. https://doi.org/10.1002/jnr.25164.

(108) Song, H.; Moon, M.; Choe, H. K.; Han, D.-H.; Jang, C.; Kim, A.; Cho, S.; Kim, K.; Mook-Jung, I. Aβ-Induced Degradation of BMAL1 and CBP Leads to Circadian Rhythm Disruption in Alzheimer's Disease. *Mol. Neurodegener.* **2015**, *10* (1), 13. https://doi.org/10.1186/s13024-015-0007-x.

(109) Homolak, J.; Mudrovčić, M.; Vukić, B.; Toljan, K. Circadian Rhythm and Alzheimer's Disease. *Med. Sci.* **2018**, *6* (3), 52. https://doi.org/10.3390/medsci6030052.

(110) Sharma, A.; Sethi, G.; Tambuwala, M. M.; Aljabali, A. A. A.; Chellappan, D. K.; Dua, K.; Goyal, R. Circadian Rhythm Disruption and Alzheimer's Disease: The Dynamics of a Vicious Cycle. *Curr. Neuropharmacol.* **2020**, *19* (2), 248–264. https://doi.org/10.2174/1570159X18666200429013041.

(111) Wise, L. E.; Thorpe, A. J.; Lichtman, A. H. Hippocampal CB1 Receptors Mediate the Memory Impairing Effects of Δ9-Tetrahydrocannabinol. *Neuropsychopharmacology* **2009**, *34* (9), 2072–2080. https://doi.org/10.1038/npp.2009.31.

(112) de Oliveira Alvares, L.; Pasqualini Genro, B.; Diehl, F.; Molina, V. A.; Quillfeldt, J. A. Opposite Action of Hippocampal CB1 Receptors in Memory Reconsolidation and Extinction. *Neuroscience* **2008**, *154* (4), 1648–1655. https://doi.org/10.1016/j.neuroscience.2008.05.005.

(113) Davis, M. P. Cannabinoids in Pain Management: CB1, CB2 and Non-Classic Receptor Ligands. *Expert Opin. Investig. Drugs* **2014**, *23* (8), 1123–1140. https://doi.org/10.1517/13543784.2014.918603.

(114) Cardinal, P.; Bellocchio, L.; Clark, S.; Cannich, A.; Klugmann, M.; Lutz, B.; Marsicano, G.; Cota, D. Hypothalamic CB1 Cannabinoid Receptors Regulate Energy Balance in Mice. *Endocrinology* **2012**, *153* (9), 4136–4143. https://doi.org/10.1210/en.2012-1405.

(115) Wittmann, G.; Deli, L.; Kalló, I.; Hrabovszky, E.; Watanabe, M.; Liposits, Z.; Fekete, C. Distribution of Type 1 Cannabinoid Receptor (CB1)-immunoreactive Axons in the Mouse Hypothalamus. *J. Comp. Neurol.* **2007**, *503* (2), 270–279. https://doi.org/10.1002/cne.21383.

(116) Acuna-Goycolea, C.; Obrietan, K.; van den Pol, A. N. Cannabinoids Excite Circadian Clock Neurons. *J. Neurosci.* **2010**, *30* (30), 10061–10066.

https://doi.org/10.1523/JNEUROSCI.5838-09.2010.

(117) Esposito, G.; Scuderi, C.; Savani, C.; Steardo, L.; De Filippis, D.; Cottone, P.; Iuvone, T.; Cuomo, V.; Steardo, L. Cannabidiol in Vivo Blunts B-amyloid Induced Neuroinflammation by Suppressing IL-1β and INOS Expression. *Br. J. Pharmacol.* **2007**, *151* (8), 1272–1279. https://doi.org/10.1038/sj.bjp.0707337.

(118) Hamelink, C.; Hampson, A.; Wink, D. A.; Eiden, L. E.; Eskay, R. L. Comparison of Cannabidiol, Antioxidants, and Diuretics in Reversing Binge Ethanol-Induced Neurotoxicity. *J. Pharmacol. Exp. Ther.* **2005**, *314* (2), 780–788. https://doi.org/10.1124/jpet.105.085779.

(119) Janefjord, E.; Mååg, J. L. V.; Harvey, B. S.; Smid, S. D. Cannabinoid Effects on β Amyloid Fibril and Aggregate Formation, Neuronal and Microglial-Activated Neurotoxicity In Vitro. *Cell. Mol. Neurobiol.* **2014**, *34* (1), 31–42. https://doi.org/10.1007/s10571-013-9984-x.

(120) Scuderi, C.; Steardo, L.; Esposito, G. Cannabidiol Promotes Amyloid Precursor Protein Ubiquitination and Reduction of Beta Amyloid Expression in SHSY5Y APP+ Cells Through PPARγ Involvement. *Phyther. Res.* **2014**, *28* (7), 1007–1013. https://doi.org/10.1002/ptr.5095.

(121) Ingber, D. E. Reverse Engineering Human Pathophysiology with Organs-on-Chips. *Cell* **2016**, *164* (6), 1105–1109. https://doi.org/10.1016/j.cell.2016.02.049.

(122) Zhang, B.; Radisic, M. Organ-on-a-Chip Devices Advance to Market. *Lab Chip* **2017**, *17* (14), 2395–2420. https://doi.org/10.1039/C6LC01554A.

(123) Oleaga, C.; Bernabini, C.; Smith, A. S. T.; Srinivasan, B.; Jackson, M.; McLamb, W.; Platt, V.; Bridges, R.; Cai, Y.; Santhanam, N.; et al. Multi-Organ Toxicity Demonstration

in a Functional Human in Vitro System Composed of Four Organs. *Sci. Rep.* **2016**, *6* (1), 20030. https://doi.org/10.1038/srep20030.

(124) Thornham, J.; Bertram, R.; Roper, M. G. Unveiling Islet Heterogeneity Using an Automated Microfluidic Imaging System. *Sci. Rep.* **2024**, *14* (1), 24707. https://doi.org/10.1038/s41598-024-75340-1.

(125) Zhang, H.; Rong, G.; Bian, S.; Sawan, M. Lab-on-Chip Microsystems for Ex Vivo Network of Neurons Studies: A Review. *Front. Bioeng. Biotechnol.* **2022**, *10*. https://doi.org/10.3389/fbioe.2022.841389.

(126) Bandak, B.; Yi, L.; Roper, M. G. Microfluidic-Enabled Quantitative Measurements of Insulin Release Dynamics from Single Islets of Langerhans in Response to 5-Palmitic Acid Hydroxy Stearic Acid. *Lab Chip* **2018**, *18* (18), 2873–2882. https://doi.org/10.1039/C8LC00624E.

(127) Eaton, W. J.; Roper, M. G. A Microfluidic System for Monitoring Glucagon Secretion from Human Pancreatic Islets of Langerhans. *Anal. Methods* **2021**, *13* (32), 3614–3619. https://doi.org/10.1039/D1AY00703C.

(128) Cavaliere, F.; Matute, C. Utility of Organotypic Slices in Parkinson's Disease Research. In *Towards New Therapies for Parkinson's Disease*; InTech, 2011. https://doi.org/10.5772/16902.

(129) Saleheen, A.; Acharyya, D.; Prosser, R. A.; Baker, C. A. A Microfluidic Bubble Perfusion Device for Brain Slice Culture. *Anal. Methods* **2021**, *13* (11), 1364–1373. https://doi.org/10.1039/D0AY02291H.

(130) Balakrishnan, B.; Soman, D.; Payanam, U.; Laurent, A.; Labarre, D.; Jayakrishnan, A. A Novel Injectable Tissue Adhesive Based on Oxidized Dextran and Chitosan. *Acta*

Biomater. **2017**, *53*, 343–354. https://doi.org/10.1016/j.actbio.2017.01.065.

(131) Schneider, C. A.; Rasband, W. S.; Eliceiri, K. W. NIH Image to ImageJ: 25 Years of Image Analysis. *Nat. Methods* **2012**, *9* (7), 671–675. https://doi.org/10.1038/nmeth.2089.

(132) Acharyya, D.; Cooper, J.; Prosser, R. Ex Vivo Comparative Investigation of Suprachiasmatic Nucleus Excitotoxic Resiliency. *F1000Research* **2022**, *11*, 1242. https://doi.org/10.12688/f1000research.125332.1.

(133) Thomas, A.; Baillie, G. L.; Phillips, A. M.; Razdan, R. K.; Ross, R. A.; Pertwee, R. G. Cannabidiol Displays Unexpectedly High Potency as an Antagonist of CB 1 and CB 2 Receptor Agonists in Vitro. *Br. J. Pharmacol.* **2007**, *150* (5), 613–623. https://doi.org/10.1038/sj.bjp.0707133.

(134) Mezey, É.; Tóth, Z. E.; Cortright, D. N.; Arzubi, M. K.; Krause, J. E.; Elde, R.; Guo, A.; Blumberg, P. M.; Szallasi, A. Distribution of MRNA for Vanilloid Receptor Subtype 1 (VR1), and VR1-like Immunoreactivity, in the Central Nervous System of the Rat and Human. *Proc. Natl. Acad. Sci.* **2000**, *97* (7), 3655–3660. https://doi.org/10.1073/pnas.97.7.3655.

(135) Ligresti, A.; Moriello, A. S.; Starowicz, K.; Matias, I.; Pisanti, S.; De Petrocellis, L.; Laezza, C.; Portella, G.; Bifulco, M.; Di Marzo, V. Antitumor Activity of Plant Cannabinoids with Emphasis on the Effect of Cannabidiol on Human Breast Carcinoma. *J. Pharmacol. Exp. Ther.* **2006**, *318* (3), 1375–1387. https://doi.org/10.1124/jpet.106.105247.

(136) Bisogno, T.; Hanuš, L.; De Petrocellis, L.; Tchilibon, S.; Ponde, D. E.; Brandi, I.; Moriello, A. S.; Davis, J. B.; Mechoulam, R.; Di Marzo, V. Molecular Targets for Cannabidiol and Its Synthetic Analogues: Effect on Vanilloid VR1 Receptors and on the

Cellular Uptake and Enzymatic Hydrolysis of Anandamide. *Br. J. Pharmacol.* **2001**, *134* (4), 845–852. https://doi.org/10.1038/sj.bjp.0704327.

(137) Joe, E.; Ringman, J. M. Cognitive Symptoms of Alzheimer's Disease: Clinical Management and Prevention. *BMJ* **2019**, l6217. https://doi.org/10.1136/bmj.l6217.

(138) Rijal Upadhaya, A.; Kosterin, I.; Kumar, S.; von Arnim, C. A. F.; Yamaguchi, H.; Fändrich, M.; Walter, J.; Thal, D. R. Biochemical Stages of Amyloid-β Peptide Aggregation and Accumulation in the Human Brain and Their Association with Symptomatic and Pathologically Preclinical Alzheimer's Disease. *Brain* **2014**, *137* (3), 887–903. https://doi.org/10.1093/brain/awt362.

(139) Villemagne, V. L.; Rowe, C. C. Amyloid Imaging. *Int. Psychogeriatrics* **2011**, *23*, S41–S49. https://doi.org/10.1017/S1041610211000895.

(140) Struble, R. G.; Ala, T.; Patrylo, P. R.; Brewer, G. J.; Yan, X.-X. Is Brain Amyloid Production a Cause or a Result of Dementia of the Alzheimer's Type? *J. Alzheimers. Dis.* **2010**, *22* (2), 393–399. https://doi.org/10.3233/JAD-2010-100846.

(141) Wang, Y.; Shi, Y.; Wei, H. Calcium Dysregulation in Alzheimer's Disease: A Target for New Drug Development. *J. Alzheimer's Dis. Park.* **2017**, *7* (5). https://doi.org/10.4172/2161-0460.1000374.

(142) LaFerla, F. M. Calcium Dyshomeostasis and Intracellular Signalling in Alzheimer's Disease. *Nat. Rev. Neurosci.* **2002**, *3* (11), 862–872. https://doi.org/10.1038/nrn960.

(143) Bezprozvanny, I.; Mattson, M. P. Neuronal Calcium Mishandling and the Pathogenesis of Alzheimer's Disease. *Trends Neurosci.* **2008**, *31* (9), 454–463. https://doi.org/10.1016/j.tins.2008.06.005.

(144) Ferreiro, E.; Oliveira, C. R.; Pereira, C. Involvement of Endoplasmic Reticulum Ca2+

Release through Ryanodine and Inositol 1,4,5-Triphosphate Receptors in the Neurotoxic Effects Induced by the Amyloid-Beta Peptide. *J. Neurosci. Res.* **2004**, *76* (6), 872–880. https://doi.org/10.1002/jnr.20135.

(145) Del Prete, D.; Checler, F.; Chami, M. Ryanodine Receptors: Physiological Function and Deregulation in Alzheimer Disease. *Mol. Neurodegener.* **2014**, *9*, 21. https://doi.org/10.1186/1750-1326-9-21.

(146) Chen, S. R.; Leong, P.; Imredy, J. P.; Bartlett, C.; Zhang, L.; MacLennan, D. H. Single-Channel Properties of the Recombinant Skeletal Muscle Ca2+ Release Channel (Ryanodine Receptor). *Biophys. J.* **1997**, *73* (4), 1904–1912. https://doi.org/10.1016/S0006-3495(97)78221-3.

(147) Demuro, A.; Parker, I. Cytotoxicity of Intracellular Aβ42 Amyloid Oligomers Involves Ca2+ Release from the Endoplasmic Reticulum by Stimulated Production of Inositol Trisphosphate. *J. Neurosci.* **2013**, *33* (9), 3824–3833. https://doi.org/10.1523/JNEUROSCI.4367-12.2013.

(148) Krause, T.; Gerbershagen, M. U.; Fiege, M.; Weißhorn, R.; Wappler, F. Dantrolene – A Review of Its Pharmacology, Therapeutic Use and New Developments. *Anaesthesia* **2004**, *59* (4), 364–373. https://doi.org/10.1111/j.1365-2044.2004.03658.x.

(149) Uryash, A.; Flores, V.; Adams, J. A.; Allen, P. D.; Lopez, J. R. Memory and Learning Deficits Are Associated With Ca2+ Dyshomeostasis in Normal Aging. *Front. Aging Neurosci.* **2020**, *12*. https://doi.org/10.3389/fnagi.2020.00224.

(150) Uryash, A.; Mijares, A.; Lopez, C. E.; Adams, J. A.; Allen, P. D.; Lopez, J. R. Post-Anesthesia Cognitive Dysfunction in Mice Is Associated with an Age-Related Increase in Neuronal Intracellular [Ca2+]—Neuroprotective Effect of Reducing Intracellular [Ca2+]:

In Vivo and In Vitro Studies. *Cells* **2024**, *13* (3), 264. https://doi.org/10.3390/cells13030264.

(151) Chakroborty, S.; Goussakov, I.; Miller, M. B.; Stutzmann, G. E. Deviant Ryanodine Receptor-Mediated Calcium Release Resets Synaptic Homeostasis in Presymptomatic 3xTg-AD Mice. *J. Neurosci.* **2009**, *29* (30), 9458–9470. https://doi.org/10.1523/JNEUROSCI.2047-09.2009.

(152) Popugaeva, E.; Bezprozvanny, I. Role of Endoplasmic Reticulum Ca2+ Signaling in the Pathogenesis of Alzheimer Disease. *Front. Mol. Neurosci.* **2013**, *6*, 29. https://doi.org/10.3389/fnmol.2013.00029.

(153) Sui, D.; Liu, M.; Kuo, M.-H. In Vitro Aggregation Assays Using Hyperphosphorylated Tau Protein. *J. Vis. Exp.* **2015**, No. 95. https://doi.org/10.3791/51537.

(154) Xue, C.; Lin, T. Y.; Chang, D.; Guo, Z. Thioflavin T as an Amyloid Dye: Fibril Quantification, Optimal Concentration and Effect on Aggregation. *R. Soc. Open Sci.* **2017**, *4* (1), 160696. https://doi.org/10.1098/rsos.160696.

(155) Acharyya, D.; Cooper, J.; Prosser, R. Ex Vivo Comparative Investigation of Suprachiasmatic Nucleus Excitotoxic Resiliency. *F1000Research* **2023**, *11*, 1242. https://doi.org/10.12688/f1000research.125332.3.

(156) Gray, A. L. H.; Norman, V.; Oluwatoba, D. S.; Prosser, R. A.; Do, T. D. Potential Protective Function of Aβ42 Monomer on Tauopathies. *J. Am. Soc. Mass Spectrom.* **2023**, *34* (3), 472–483. https://doi.org/10.1021/jasms.2c00343.

(157) Gutierrez, G.; Ortiz, R.; Norman, V.; Prosser, R. A.; Baker, C. A. Bubble Perfusion Brain Slice Culture with Single-Droplet Stimulus Delivery in a 3D Printed Microfluidic Device. *ACS Meas. Sci. Au* **2025**.

(158) Kumar, P.; Nagarajan, A.; Uchil, P. D. Analysis of Cell Viability by the Lactate Dehydrogenase Assay. *Cold Spring Harb. Protoc.* **2018**, *2018* (6), pdb.prot095497. https://doi.org/10.1101/pdb.prot095497.

(159) Park, J.-C.; Han, S.-H.; Mook-Jung, I. Peripheral Inflammatory Biomarkers in Alzheimer's Disease: A Brief Review. *BMB Rep.* **2020**, *53* (1), 10–19. https://doi.org/10.5483/BMBRep.2020.53.1.309.

(160) Domingues, C.; da Cruz e Silva, O. A. B.; Henriques, A. G. Impact of Cytokines and Chemokines on Alzheimer's Disease Neuropathological Hallmarks. *Curr. Alzheimer Res.* **2017**, *14* (8). https://doi.org/10.2174/1567205014666170317113606.

(161) Rani, V.; Verma, R.; Kumar, K.; Chawla, R. Role of Pro-Inflammatory Cytokines in Alzheimer's Disease and Neuroprotective Effects of Pegylated Self-Assembled Nanoscaffolds. *Curr. Res. Pharmacol. drug Discov.* **2023**, *4*, 100149. https://doi.org/10.1016/j.crphar.2022.100149.

(162) Chun, H.; Lee, C. J. Reactive Astrocytes in Alzheimer's Disease: A Double-Edged Sword. *Neurosci. Res.* **2018**, *126*, 44–52. https://doi.org/10.1016/j.neures.2017.11.012.

(163) González-Reyes, R. E.; Nava-Mesa, M. O.; Vargas-Sánchez, K.; Ariza-Salamanca, D.; Mora-Muñoz, L. Involvement of Astrocytes in Alzheimer's Disease from a Neuroinflammatory and Oxidative Stress Perspective. *Front. Mol. Neurosci.* **2017**, *10*. https://doi.org/10.3389/fnmol.2017.00427.

Appendices

A. Additional Materials for Chapter 4

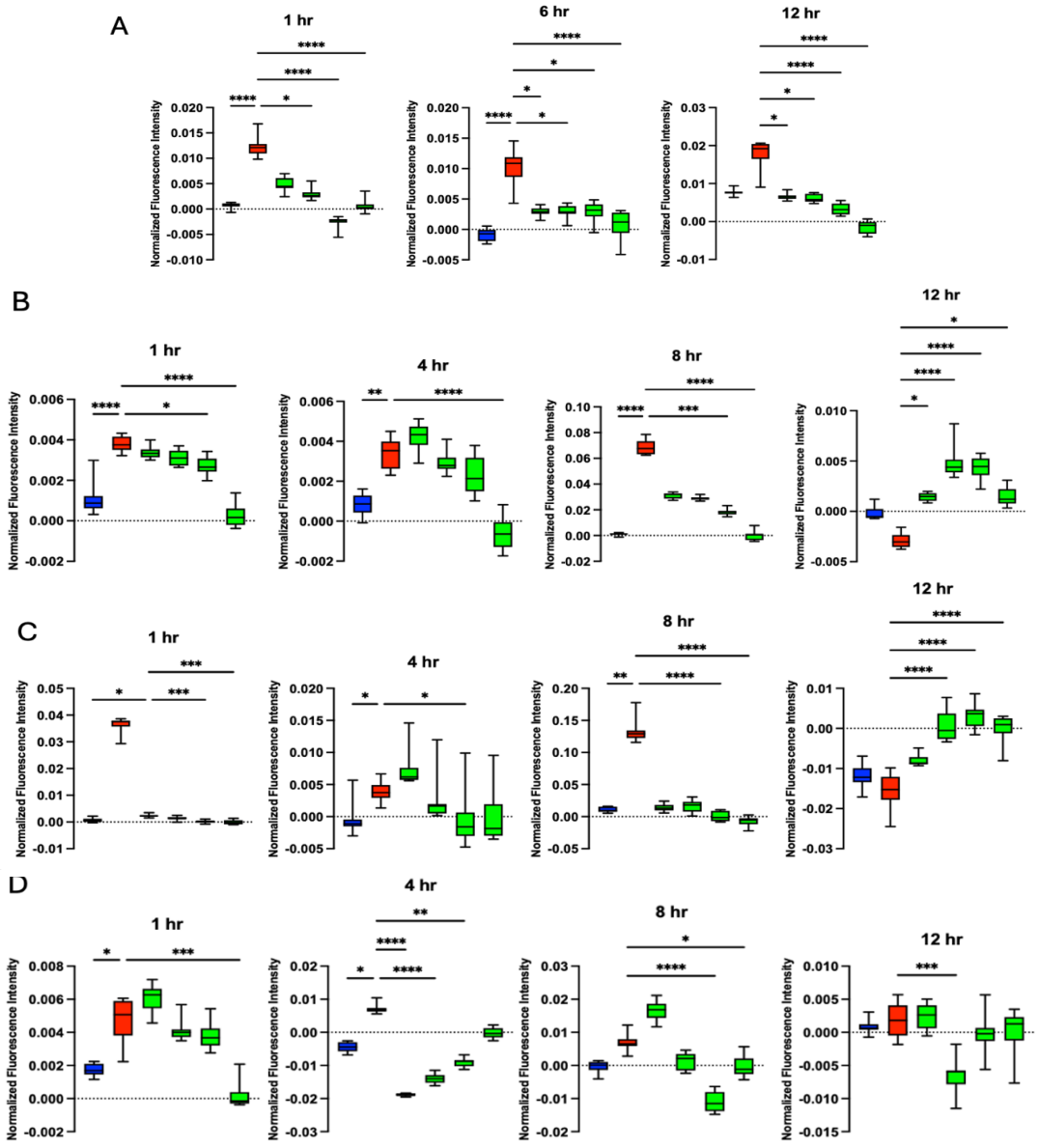


Figure A.1 Comparison of Ca^{2+} response in EC slices Summary of Ca^{2+} response in EC tissue induced by delivery of 60 mM KCl after 1 hour, 6 hours, and 12 hours of perfusion. Each dataset pools observations from three tissue slices. **B.** The analysis is identical to A, but Ca^{2+} response in EC tissue induced by delivery of 40μM Aβ after 1 hour, 4 hours, 8 hours, and 12 hours of perfusion. **C.** The analysis is identical to B, but Ca^{2+} response in EC tissue induced by delivery of 40μM tau. **D.** The analysis is identical to B, but Ca^{2+} response in EC tissue induced by delivery of 40μM Aβ:tau. *p<0.05, **p<0.01, ***p < 0.001, ****p < 0.0001, ns = p > 0.05. N=3

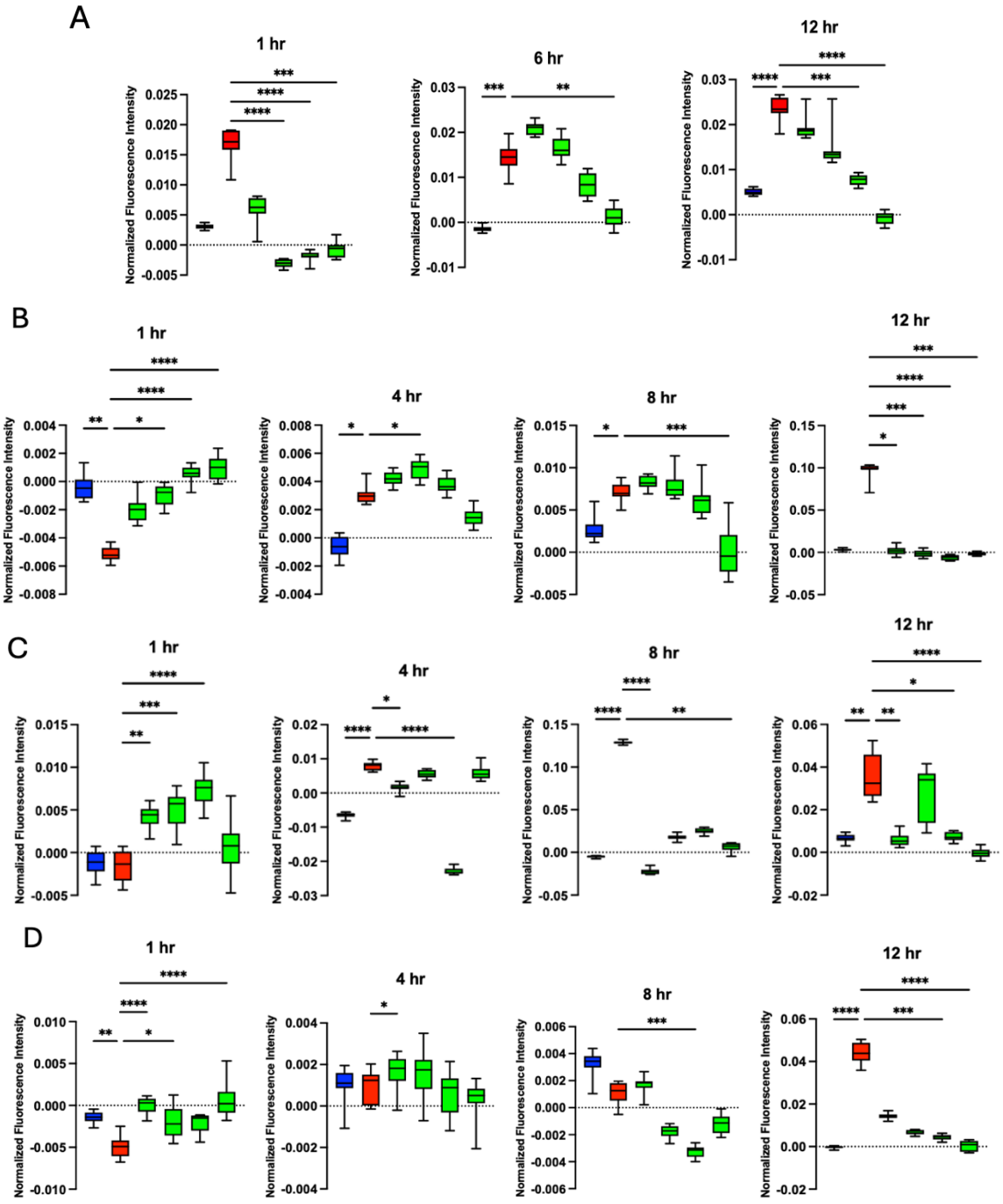


Figure A.2 Comparison of Ca^{2+} response in SCN slices Summary of Ca^{2+} response in SCN tissue induced by delivery of 60 mM KCl after 1 hour, 6 hours, and 12 hours of perfusion. Each dataset pools observations from three tissue slices. **B.** The analysis is identical to A, but Ca^{2+} response in SCN tissue induced by delivery of 40μM Aβ after 1 hour, 4 hours, 8 hours, and 12 hours of perfusion. **C.** The analysis is identical to B, but Ca^{2+} response in SCN tissue induced by delivery of 40μM tau. **D.** The analysis is identical to B, but Ca^{2+} response in SCN tissue induced by delivery of 40μM Aβ:tau. *p<0.05, **p<0.01, ***p < 0.001, ****p < 0.0001, ns = p > 0.05. N=3

While quantifying the number of microglia and neurons was not the focus of these experiments, we did identify an interesting trend of increased microglial cells in the EC compared to the SCN in tissues stimulated with tau. We also see an increase in the number of neurons in the EC compared to the SCN (**Figure A.3**). Even more interesting, when looking at tissue that has been stimulated with peptides in the presence of dantrolene, no difference between microglia and neurons in either brain region is observed (**Figure A.4**).

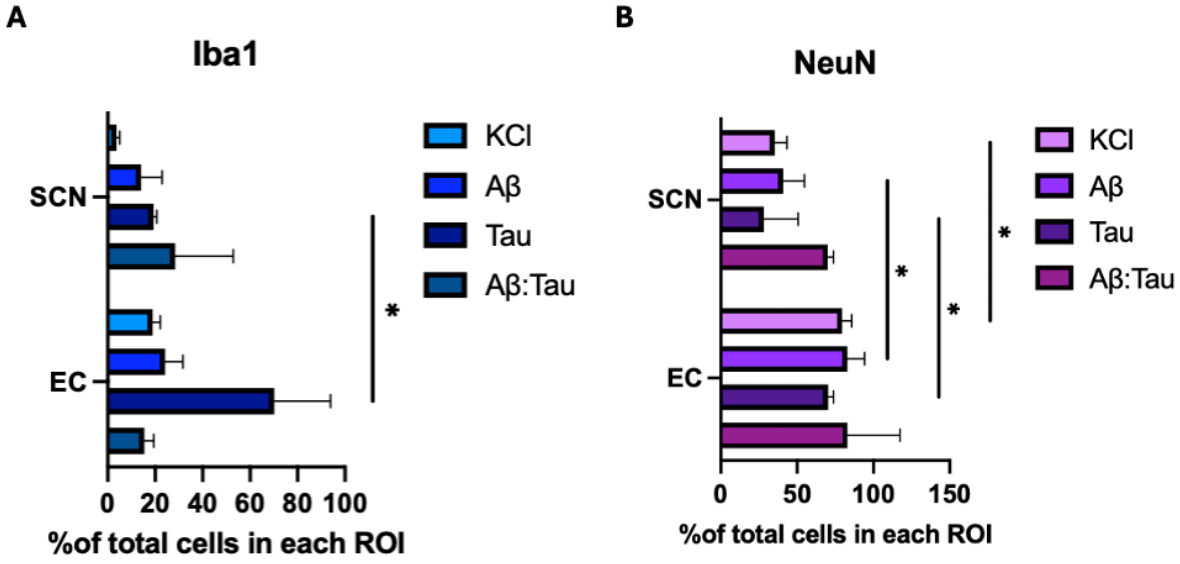


Figure A.3 Comparison of number of microglia and neurons in EC and SCN Total percentage of **A.)** microglia and **B.)** neurons in the EC and SCN after 12 hours, periodically stimulated with 40μM Aβ, tau, or 60 mM KCl. *p<0.01. N=3

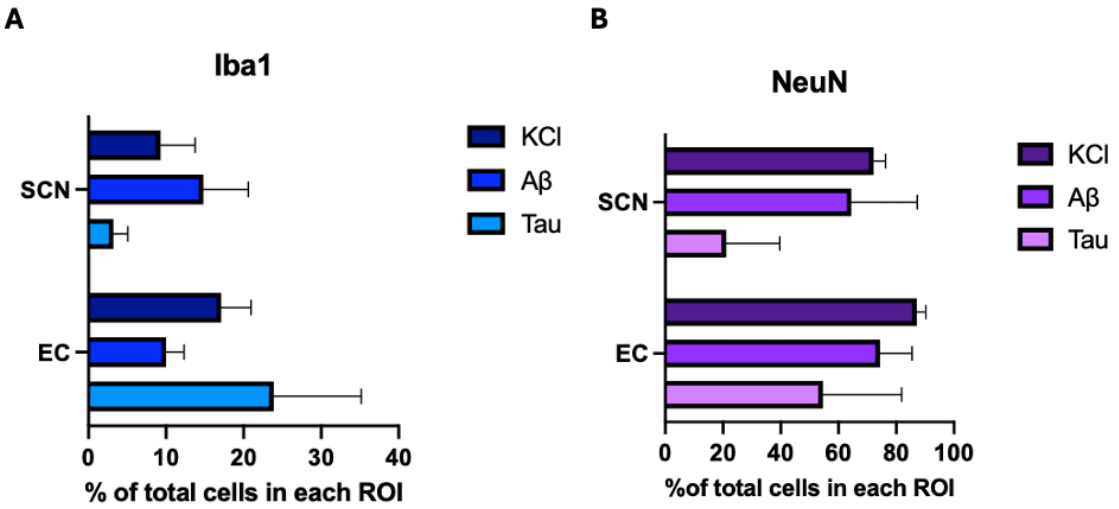


Figure A.4 Comparison of number of microglia and neurons in EC and SCN with dantrolene Total percentage of **A.)** microglia and **B.)** neurons in the EC and SCN after 12 hours, periodically stimulated with 40μM Aβ, tau, or 60 mM KCl in EBSS supplemented with 20μM dantrolene. N=3

B. Imaging Protocols

Image Analysis for Determining Cell Damage and Death

Open the .tiff image, duplicate image and minimize one copy. *Do not add the ROI yet*

Adjust image brightness/contrast (auto)

Separate colors (Image > Color > split channels). For each channel: Process > Subtract background (2 pixels, sliding paraboloid; disable smoothing)

DAPI:

Image > Adjust > Threshold (255 and variable) *Have duplicate channel image open for comparison*. Zooming in can help. Adjust the upper slide scale so that all cells are shown in red but no artifacts are red. [Entire cells don't need to be filled in red.] You are trying to keep all cells while eliminating the very small, faint dots. In some brain regions (e.g., hippocampus) it is hard to get a threshold that works for the entire tissue section. If that is the case, you may need to set a distinct threshold for each ROI. For other brain regions (e.g., hypothalamus, cortex) a single threshold should work for the entire image. [Don't try to match the threshold scale number across different images.] Save the threshold you use to an excel file.

If there are an excessive number of cell clumps, you can try setting the threshold using an image that has not had the brightness/contrast adjusted, or one where the brightness/contrast has been adjusted after colors were separated (be sure background is subtracted).

Process > Binary (watershed)

Overlay ROI by choosing (clicking on) the ROI in the ROI manager

Analyze > Analyze Particles (using default settings, bare outlines, summary).

Save to excel file the cell number of cells for each ROI as indicated in the "summary" window.

Dealing with clumps: Compare the outlined areas with the image you used to compare with and add points when multiple cells are clumped together (see image below).

Note: for each "clump" you add N-1 dots. That is, if the clump represents 2 cells, add 1 point. If it represents 3 cells, add 2 points.

When finished, add these points to ROI manager, then select "measure". Add that number of cells to the previous total calculated by the "analyze particles" process and save the new total. [Alternatively, when you are finished, add one more point where you can see the number; the number to add to the previous total will be one less than that.]

PI:

Image > Adjust > Threshold (255 and variable) *Have duplicate split channel image open for comparison*. Zooming in can help. Adjust the upper slide scale so that all cells you wish to identify are shown in red. [Entire cells don't need to be filled in red.]

There are *two separate thresholds* you need to identify: one that separates Grade 3 (high intensity, sharp edges) from Grade 2 (medium intensity, sharp edges) cells. In this case, set the threshold so only the brightest (dead) cells are red. Write down the threshold you use in the excel file. The second threshold separates Grade 0/1 (minimal PI staining) from Grades 2 + 3 (more PI staining). For this one, set the threshold so all but the dim (healthy) cells are red. Save the threshold you use in the excel file. After each thresholding:

Process > Binary (watershed) - - hopefully all cells will get separated and not remain in clumps. If not, use 'dealing with clumps' procedure outlined above.

Overlay ROI; choose (click on) ROI in ROI manager

Analyze > Analyze Particles (using defaults; summary).

Save to excel file the cell number of cells identified with each threshold for each ROI as indicated in the "summary" window.

Important Note: the number of cells calculated with the lower threshold (eliminating Grade 0/1 cells only) includes Grade 2 + Grade 3 cells. You need to subtract the number of Grade 3 cells (determined with the higher threshold) to get the number of Grade 2 cells.

Image Analysis for Colocalization of PI in Specific Cell Types

Open the .tiff image, duplicate image and minimize one copy. Do not add the ROI yet

Adjust image brightness/contrast (auto)

Separate colors (Image > Color > split channels). For each channel: Process > Subtract background (2 pixels, sliding paraboloid; disable smoothing, preview: check to see the setting has not eliminated true cells, but is clears up background noise/haze. Duplicate all channels.

<u>DAPI (total number of cells):</u>

Image > Adjust > Threshold (255 and variable)

Save the threshold you use to an excel file.

Note: Having a duplicate image open for comparison and zooming in can help. Adjust the upper slide scale so that all cells are shown in red but no artifacts are red. [Entire cells don't need to be filled in red.] You are trying to keep all cells while eliminating the very small, faint dots. In some brain regions (e.g., hippocampus) it is hard to get a threshold that works for the entire tissue section. If that is the case, you may need to set a distinct threshold for each ROI. For other brain regions (e.g., hypothalamus, cortex) a single threshold should work for the entire image. [Don't try to match the threshold scale number across different images.]

If there are an excessive number of cell clumps, you can try setting the threshold using an image that has not had the brightness/contrast adjusted, or one where the brightness/contrast has been adjusted after colors were separated (be sure background is subtracted).

Process > Binary (watershed)

Overlay ROI by choosing (clicking on) the ROI in the ROI manager

Analyze > Analyze Particles (using default settings, bare outlines, summary).

Save to excel file the cell number of cells for each ROI as indicated in the "summary" window.

Dealing with clumps: Compare the outlined areas with the image you used to compare with and add points when multiple cells are clumped together (see image below).

Note: for each "clump" you add N-1 dots. That is, if the clump represents 2 cells, add 1 point. If it represents 3 cells, add 2 points.

<u>Alexa 488 (Total number of specific cell type):</u>

Image > Adjust > Threshold (255 and variable) Have duplicate channel image open for comparison. Zooming in can help. Adjust the upper slide scale so that all cells are shown in red but no artifacts are red. [Entire cells don't need to be filled in red.] You are trying to keep all cells while eliminating the very small, faint dots. [Don't try to match the threshold scale number across different images.] Save the threshold you use to an excel file.

If there are an excessive number of cell clumps, you can try setting the threshold using an image that has not had the brightness/contrast adjusted, or one where the brightness/contrast has been adjusted after colors were separated (be sure background is subtracted).

Process > Binary (watershed) - - hopefully most clumps will get separated into individual cells.

Overlay ROI by choosing (clicking on) the ROI in the ROI manager

Analyze > Analyze Particles (using default settings, bare outlines, summary). Save to excel file the number of cells for each ROI as indicated in the “summary” window.

Merged PI and Alexa 488:

In the green channel make sure the ROI is on the image and make sure the ROI Manager is open

Edit>Clear Outside

Image > Adjust > Threshold (255 and variable)

Adjust the upper slide scale so that all cells you wish to identify are shown in red. (Entire cells don’t need to be filled in red) Click apply

Process > Binary (watershed) - - hopefully most clumps will get separated into individual cells.

Edit>Selection>Create Selection

In the ROI manager hit “add” then “rename” and name the new ROI ‘Green’

Analyze > Analyze Particles (using default settings, bare outlines, summary).

In the red channel duplicate the images.

Add the ROI and make sure it is on the image and make sure the ROI Manager is open

Edit>Clear Outside

Image > Adjust > Threshold (255 and variable), Threshold for Grade 3

Adjust the upper slide scale so that all cells you wish to identify are shown in red. (Entire cells don’t need to be filled in red) Do NOT click apply

Edit>Selection>Create Selection

In the ROI manager hit “add” then “rename” and name the new ROI ‘Red Grade 3’

In the duplicated red channel add the ROI and make sure it is on the image and make sure the ROI Manager is open

Edit>Clear Outside

Image > Adjust > Threshold (255 and variable), Threshold for Grade 2

Adjust the upper slide scale so that all cells you wish to identify are shown in red. (Entire cells don't need to be filled in red) Do NOT click apply

Edit>Selection>Create Selection

In the ROI manager hit "add" then "rename" and name the new ROI 'Red Grade 2'

Click on the green channel image, then click 'Red Grade 3' in the ROI manager. At this point you should see the cells you've identified as grade 3 overlayed in the green image

Analyze>Analyze Particles (using default settings, bare outlines, summary). Save to excel file the number of grade 3 cells that overlap with green cells within the ROI as indicated in the "summary" window.

Click on the green channel image, then click 'Red Grade 2' in the ROI manager. At this point you should see the cells you've identified as grade 2 overlayed in the green image.

Analyze>Analyze Particles (using default settings, bare outlines, summary). Save to excel file the number of grade 2 cells that overlap with green cells within the ROI as indicated in the "summary" window.

Important Note: the number of cells calculated with the lower threshold (eliminating Grade 0/1 cells only) includes Grade 2 + Grade 3 cells. You need to subtract the number of Grade 3 cells (determined with the higher threshold) to get the number of Grade 2 cells.

Image Analysis for Calcium Imaging Time Lapsed Videos

Open ImageJ

Open the image by dragging the .avi file to the ImageJ tool bar.

The AVI Reader window should pop up, make sure only "Use Virtual Stack" is checked, then press OK.

Before adding the ROI, check to make sure that the number of images is displayed in the top left corner and matches the number of frames captured during the experiment.

Click and drag the slider at the bottom to flip through the images and check that there are changes in intensity to indicate switches between bubbles and droplets.

Add the appropriate ROI (should be the same as the file name, ending in ".roi") by clicking and dragging it into the ImageJ tool bar.

To overlay the ROI to all images in the file, click Image>Overlay>Add Selection…

Next, add the ROI to the ROI Manger by clicking Image>Overlay>To ROI Manager

In the ROI Manager, select the ROI by clicking on it. Once it is highlighted click More>>Multi Measure

A table containing the mean intensity value for each image in the file should pop up. (This step may take a minute, be patient).

Right click to select all values, then copy and paste these on to the provided excel sheet.

Once you have all the data in excel you can close ImageJ (it is not necessary to save the values in ImageJ).

Open Plot 2x (Download at https://apps.micw.org/apps/plot2/downloads.php)

Two windows should open, the untitled plot window and the inspector window.

In the inspector window, click the "XY" button in the upper right corner.

Copy and paste all the values from the excel sheet into the inspector window.

The intensity traces should appear in the plot window. Peaks represent gas bubbles, and the flat lines represent media droplets. The data should have an overall negative slope.

In the inspector window, you should be able to select a single point, and a dot should appear on the plot window corresponding with that point.

Using the selector, scroll through the values to find the ones corresponding to only the bubbles. Make a note of the bubble values and highlight them in the excel sheet. In the example above, values 30 – 37 would be highlighted in the excel sheet.

Repeat for all the bubble values in the plot window.

VITA

Victoria Nickole Norman graduated from Suitland High school in Forestville, Maryland in 2014. She earned her Bachelor of Science in Chemistry from North Carolina A&T State University in Greensboro, North Carolina. During her undergraduate career, she completed a summer Research Experience for Undergraduates at the University of Tennessee, Knoxville (UTK) with Dr. Chris Baker, which inspired her to pursue a career in research and attend graduate school. She continued to work with Dr. Baker and went on to earn a Master of Science in Analytical Chemistry. In 2020, despite a global pandemic, Victoria decided to continue her graduate studies and moved to the Biochemistry & Cellular and Molecular Biology (BCMB) department at UTK where she began to work with Dr. Rebecca A. Prosser. Her research focused on studying regional differences in response to initial amyloid beta and tau exposure in the suprachiasmatic nucleus and entorhinal cortex using microfluidic technology. During her time in graduate school, she was involved in numerous organization both at the department and university level. She has served in leadership positions in the Association of Chemistry Graduate Students, the graduate school's Peer Connection Groups, and the BCMB Graduate Student Organization. Additionally, Victoria was a Neuroscience Program scholar in the 2024-2026 cohort of the Society of Neuroscience and had the opportunity to participate in the MBL Summer Program in Neuroscience, Excellence and Success course in 2024. During her free time, she enjoys reading fiction, trying new recipes and spending time with her dog, George.